A multi-isotopic geochemical investigation of the Lower Zone, Bushveld Complex, South Africa: implications for a crustal component for parental magmas

Hunter R. Edwards

Dissertation presented for the degree of Master of Science in the Department of Geological Sciences
University of Cape Town

May 2020

Supervisor: Dr. Geoffrey H. Howarth

Plagiarism declaration

I know the meaning of plagiarism and declare that all of the work in this dissertation, except for that which is properly acknowledged, is my own

Hunter Edwards

May 2020

Abstract

The current study focuses on the Lower Zone of the Bushveld Complex, South Africa using multiple geochemical and isotopic systems to determine the origin of crustal signatures, i.e. crustal assimilation or recycled crust in the mantle source, present throughout the Rustenburg Layered Suite (RLS) such as elevated $\delta^{18}O$ values. These geochemical and isotopic systems include major elements, trace elements, highly siderophile elements, oxygen isotopes, $^{87}Sr/^{86}Sr$, $^{143}Nd/^{144}Nd$, and Os-Os isotopes. Samples come from the Nooitgedacht Borehole 2 (NG2) at Union Section of the western limb of the Bushveld Complex, which sampled the Lower Zone. The $^{87}Sr/^{86}Sr_i$ (0.7043 – 0.7086) and εNd_i values (-7.40 - -4.97) calculated in this study are in agreement with published data for the Bushveld. The majority of NG2 samples contain $\delta^{18}O$ greater than mantle peridotite (5.50‰) and MORB (5.70‰), in which NG2 $\delta^{18}O$ ranges from 5.60 up to 8.00‰ for olivine, orthopyroxene, and clinopyroxene separates. These high $\delta^{18}O$ values suggests the Bushveld magmas sourced a crustal reservoir, either through crust assimilation or recycled crustal materials in the mantle source. This is the first study utilizing the Re-Os isotope system for the Lower Zone. The γOs_i values for the NG2 suite range from -4.37 to +35.9, which overlap with published data for the Critical Zone and the Platreef, the only previous Re-Os studies on the Bushveld. However, there are no previously reported negative γOs_i values for the Bushveld. The range in γOs_i values for the NG2 samples suggest mixing of at least two geochemical reservoirs. In addition to Lower Zone NG2 samples, sample NG2-773.65 is a chilled margin sample at the base of the NG2 borehole that contains high $\delta^{18}O$ ($\delta^{18}O$ = 9.42 – 9.78‰) and radiogenic γOs_i (γOs_i = +62.5), in which the crust and/or recycled crust in the mantle source caused these high values. Sample NG2-734.64 contains the second lowest $\delta^{18}O$ ($\delta^{18}O$ = 5.67‰) and most unradiogenic γOs_i (γOs_i = -4.37) values for the NG2 suite, evidence for a harzburgitic SCLM (H-SCLM) mantle source component. A lack of correlations for γOs_i values with $\delta^{18}O$ and $^{87}Sr/^{86}Sr_i$ values are indices for crustal assimilation processes. This lack in correlation may suggest a crustal component in the mantle is more likely than assimilation of the crust during ascent of the magmas toward the surface. The geochemical data presented in this study suggest the Lower Zone parent magma had a H-SCLM mantle source component in addition to the assimilation of the crust and/or the eclogitic SCLM (E-SCLM).

Acknowledgements

I would like to thank those who helped and supported me through this journey. Particularly, I would like to thank my exceptionally supportive parents, Dennis and Megan, who made sacrifices for me to pursue my dreams and aspirations. Additionally, they were understanding for me to make the trip from the United States to Cape Town to finish my degree at the University of Cape Town (UCT). I thank my family, friends, and my sister, Savannah, for their support. Jennie Cerone was exceptionally supportive from the time I left the US, throughout my time in Cape Town, to the time I came back home, and I thank her for this. I thank Geoff Howarth for taking me on as a student at the University of Georgia (UGA), making it possible for me to finish my degree in Cape Town, and for reviewing numerous thesis manuscripts. I thank Dr. James Day, Dr. Marine Paguet, and Ruan Hattingh for assistance in analyses at Scripps Institution of Oceanography (Scripps), as well as the hospitality from my friends Carrie Macintosh and Sarah Perry during my stay at Scripps. Julie Cox and Chris Harris were extremely helpful in teaching me how to conduct oxygen isotope analyses at UGA and UCT, respectively. A thank you to Jonathan Van Rooyen and Dr. Philip Janney for their assistance preparing samples and analysing them for major element concentrations. I thank my lab mate at UGA, Sierra Ramsey, for discussing both science and nonsense in the lab. Dr. Doug Crowe was someone I could always turn to at UGA when I had questions about economic deposits, general science, or just someone to talk to (or bother). In addition, I thank Drs. Robert Bodnar, Sterling Nesbitt, and Mark Caddick at Virginia Tech for giving me helpful advice for impactful decisions in my life and for teaching me the groundwork on how to become a successful scientist and geoscientist. Dr. Matthew Sublett believed in me even when I doubted my abilities, so I thank him deeply for that. I appreciate the hospitality shown to me by my friends Chad Peel, Guy Salomon, and Fiona Clark throughout my stay in Cape Town.

I dedicate this thesis to my Nana, Barbara J. Edwards (8/21/1946 – 11/22/2005).

This research was supported, in-part, by an NRF Incentive award to Dr. Howarth, NRF grant #115370

Table of Contents

1. Introduction

The Bushveld Complex (also referred to as the Bushveld Igneous Complex) is the largest layered mafic intrusion (LMI) in the world and contains the majority of the Earth's PGE reserves and significant amounts of chromium and vanadium ore (Vermaak, 1995; Cawthorn, 1999a; Barnes et al., 2010; Barnes and Ripley, 2016). The ~2.06 Ga (Buick et al., 2001) Bushveld Complex is located in northeastern South Africa (Figure 1), has a surface area of ~65,000 km^2, and a thickness between 7–9 km (Eales and Cawthorn, 1996; Buick et al., 2001; Cawthorn, 2015).

Although the Bushveld is the largest LMI on Earth, there are continued debates on how the PGE ores formed, what caused the layering, the timing of emplacement, mantle source(s), and the degree and source of crustal contamination (e.g. Maier et al., 2000; Harris et al., 2005; Richardson and Shirey, 2008; Eales and Costin, 2012; Rajesh et al., 2013; Cawthorn, 2015; Zeh et al., 2015; Latypov et al., 2018; Zeh et al., 2019; Zirakparvar et al., 2019). The issues of mantle source(s) and crustal contamination are addressed in this study. More specifically, this study will address whether a recycled crustal component (e.g. an eclogitic upper mantle reservoir) or the upper crust is the source for the geochemical characteristics reflected in the Lower Zone of the Bushveld Complex.

A key feature of the RLS is elevated $\delta^{18}O$, relative to mantle peridotites (~ 5.50‰, Mattey et al., 1994; Eiler, 2001), with $\delta^{18}O$ values that range from 5.70‰ to 7.80‰, with most falling between 6.00‰ and 7.00‰ (Harris et al. 2005). In addition to the Bushveld *sensu stricto*, elevated $\delta^{18}O$ compositions have been reported for Bushveld platiniferous dunite pipes ($\delta^{18}O$ = 5.70 - 7.10‰) (Günther et al., 2018). Previous investigations have modelled the amount of crustal contamination necessary to account for the trace element concentrations and the isotopic values for Bushveld rocks (e.g. Maier et al., 2000; Harris et al., 2005; Eales and Costin, 2012). The amount of crustal assimilation given by these models typically ranges from a minimum of 20% up to 41% (e.g. Barnes, 1989; Harmer et al., 1995; Maier et al., 2000; Barnes and Maier, 2002; Buchanan et al., 2002; Buchanan et al., 2004; Harris et al., 2005; Eales and Costin, 2012; Maier et al., 2016), which may be unrealistic degrees of crustal contamination due to effects such as dilution (e.g. Barnes et al., 2010), the inability to satisfy radiogenic $^{87}Sr/^{86}Sr_i$ and γOs_i values and the lateral

homogeneity observed in the Bushveld, such as the Merensky Reef (e.g. Kruger and Marsh, 1982; Lee and Butcher, 1990; Schoenberg et al., 1999; Richardson and Shirey, 2008).

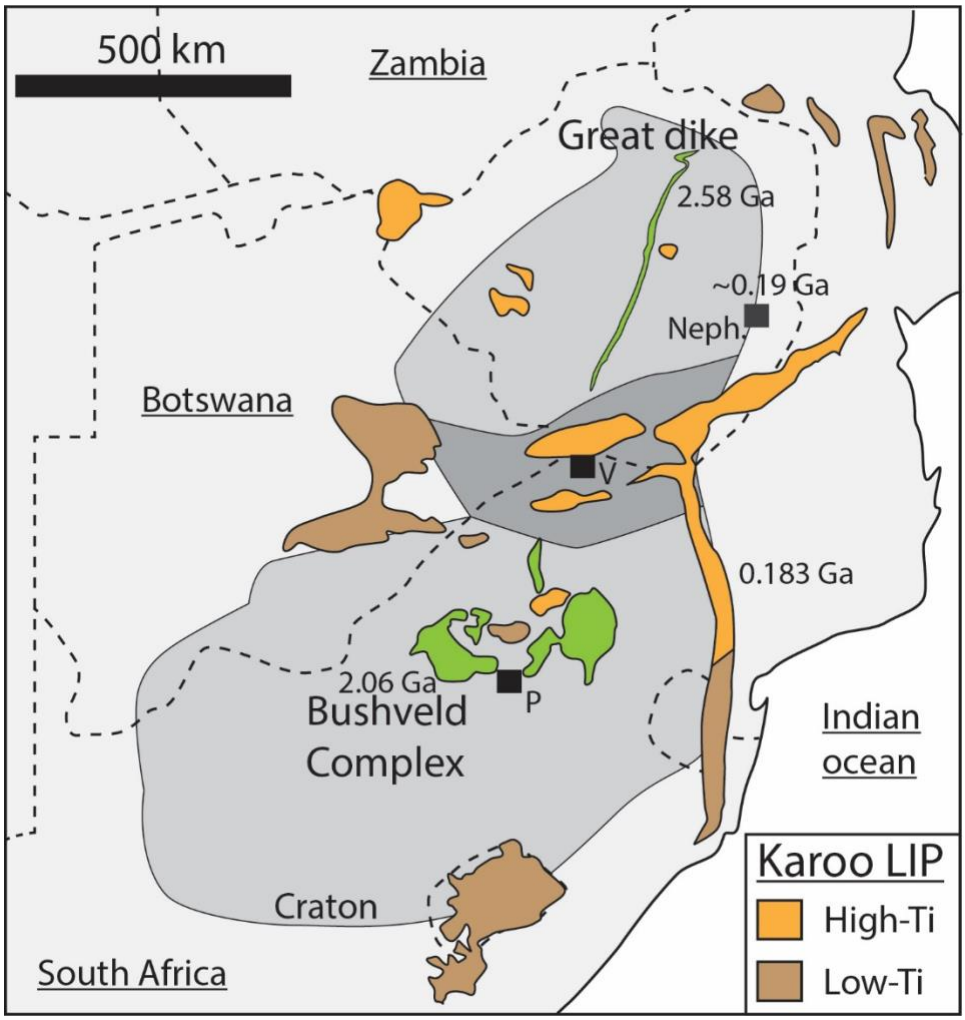

Figure 1. Map illustrating the proximity of the Bushveld Complex and the Karoo LIP of southern Africa, with the locations of Premier (P) and Venetia (V) kimberlites of South Africa, and Nephelinites of the Buhera District, Zimbabwe.

Assimilation-fractional crystallization (AFC) processes can cause $\delta^{18}O$ compositions to increase with increasing degrees of crustal contamination, however, $\delta^{18}O$ values for the RLS are variable and do not show correlations with depth (Harris et al., 2005; Günther et al., 2018). Maier et al. (2000) argue that AFC should not be strongly applied to magma chambers because they likely represent open systems. Further, (Yao et al., 2020) support simple assimilation-batch crystallisation (ABC) over AFC processes for the Lower Zone and the Critical Zone. Alternatively,

the upper Critical Zone and Main Zone likely formed by a two-stage ABC process, and the upper Main Zone and Upper Zone through traditional AFC (Yao et al., 2020). In addition to oxygen isotopes, Nd and Sr isotopes can also be used to track crustal assimilation/contamination. Although there are no previous publications reporting both oxygen and Nd isotopes for the Bushveld Lower Zone, oxygen would have increasing $\delta^{18}O$ values with decreasing εNd_i values, if progressive upper crustal contamination occurred (Depaolo, 1981; Günther et al., 2018). Additionally, there is only one publication that reports both oxygen and Sr_i isotopic data for the Bushveld (i.e. Reid et al., 1993). With respect to crustal contamination, Sr isotope values will increase with increasing crustal contribution (Maier et al., 2000). The elevated $\delta^{18}O$ values for the Bushveld may be related to recycled crust in the mantle rather than crustal assimilation, and there may be different reservoirs and processes that caused the Bushveld to contain elevated $\delta^{18}O$ values (Harris et al., 2015; Günther et al., 2018). On the contrary, 20-40% crustal contamination is feasible if the intruding magma was komatiitic (Eales and Costin, 2012). It has been determined experimentally that 1g of komatiite melt is able to melt 0.64g of 0°C granite and 1.64g of granite that has an initial temperature of 850°C (Sparks, 1986). Isotopic investigations on the Bushveld commonly report only one or two isotopic systems (e.g. Kruger, 1994; Schoenberg et al., 1999; Maier et al., 2000; Harris et al., 2005; Prevec et al., 2005; Reisberg et al., 2011; Günther et al., 2018; Zirakparvar et al., 2019). The primary objective of the current study is to utilise multiple isotopic systems to determine the degree and source(s) of crustal input for the Bushveld due to their differences and abilities to track contamination. It is also useful to compare Bushveld isotopic data to the Karoo Large Igneous Province (LIP) due to its close proximity (Figure 1) and the geochemical similarities that it shares with the Bushveld (e.g., Harris et al., 2015).

Oxygen isotopes for the nearby high-Ti picrites of the Tuli and Mwenezi basins of the Karoo LIP (Figure 1) show similar elevated $\delta^{18}O$ values (6.00 – 6.70‰ for olivine and orthopyroxene separates) to the Bushveld, despite their large age discrepancies (Karoo: ~180 Ma; Bushveld ~2.06 Ga) (Harris et al., 2015). The similar $\delta^{18}O$ values for the Bushveld and Karoo have been suggested to be related to a long-lived enriched mantle source with a recycled crust component rather than obtaining elevated $\delta^{18}O$ from crustal assimilation *en route* to the surface

(Harris et al., 2015). The subcontinental lithospheric mantle (SCLM), more specifically an eclogitic-type SCLM (E-SCLM) reservoir, has been suggested to be the source for these elevated $\delta^{18}O$ compositions (Harris et al., 2015). One way the E-SCLM forms from the subduction of oceanic crust (basalt/gabbro), which is metamorphosed into eclogite during its residence in the mantle (Hacker, 1996; Shirey et al., 2001). Alternatively, the E-SCLM could form from the ponding of melts derived from the asthenosphere near the base of the depleted lithosphere (underplated magmas), cumulates, and melt-peridotite reaction zones (Griffin and O'Reilly, 2007). Oxygen isotope values range from 5.30 – 8.00‰ for eclogite mantle xenoliths from the Roberts Victor kimberlite, which are in agreement with published Bushveld and Karoo data (MacGregor and Manton, 1986; Schulze et al., 2000; Harris et al., 2005; Harris et al., 2015; Riches et al., 2016; Günther et al., 2018). The elevated $\delta^{18}O$ values given by the Bushveld are of crustal origin, however, the issue, and goal of this work, is to determine whether the crustal material is recycled (e.g., E-SCLM) or sourced from the upper crust.

A particularly useful isotope system for tracking recycled crust in the mantle is Re-Os, which is commonly used in plume-related ocean island basalt (OIB) settings (e.g., Lassiter and Hauri, 1998). Osmium isotopes are used to differentiate between materials from the core-mantle boundary, upper mantle, lithospheric mantle, and crustal reservoirs due to their distinct compositions from these reservoirs (e.g. Day, 2013). Osmium isotopes are commonly employed for ocean island basalts (OIB) and are frequently used contemporaneously with more traditional isotope systems such as Sr and Nd isotopes (e.g. Schiano et al., 2001; Eisele et al., 2002; Sen et al., 2011). The Re-Os isotopic system is unique compared to other traditional radiogenic isotopic systems (e.g. Sr and Nd) in that the parent element, Re, is moderately incompatible, compared to the daughter, Os, which is highly compatible, in metal and sulphide phases, instead of both the parent and daughter behaving incompatibly in silicate phases (i.e. Sm-Nd and Rb-Sr) (e.g. Day, 2013). In addition, more traditional isotope systems (e.g. Sr, Nd, Hf, Pb) give smaller isotopic fractionation ranges for ocean island basalts (OIB) that have input from recycled crustal sources, or from the crust itself, than the Re-Os system, which is more sensitive to input from these crustal sources (e.g. Zindler and Hart, 1986; Pegram and Allègre, 1992; Hauri and Hart, 1993; Reisberg et al., 1993; Marcantonio et al., 1995; Roy-Barman and Allègre, 1995; Widom and Shirey, 1996;

Lassiter and Hauri, 1998; Brandon et al., 1999; Widom et al., 1999; Schiano et al., 2001; Eisele et al., 2002; Schaefer et al., 2002; Hofmann, 2003; Lassiter et al., 2003; Workman et al., 2004; Escrig et al., 2005; Brandon et al., 2007; Class et al., 2009; Day et al., 2009; Debaille et al., 2009; Ireland et al., 2009; Day et al., 2010a; White, 2010; Jackson and Shirey, 2011; Day, 2013). Thus, Re-Os isotopic values display a greater disparity between crust and mantle materials than more traditional isotopic systems (e.g. Sr and Nd) (Day, 2013). Further, the long-lived character (half-life: ~42 Ga) of the Re-Os isotope system make this system useful in determining long-term reservoir sources (Day, 2013). This is particularly useful when combined with HSE compositions, which reflect the most recent processes to act on magmas (Day, 2013). The utilisation of Os isotopes and highly siderophile elements (HSE) may bring to light the mantle source(s) and the degree and source of crustal contamination for the Bushveld.

The goal of this study is to utilize multiple radiogenic and stable isotope systems ($^{87}Sr/^{86}Sr$, $^{143}Nd/^{144}Nd$, $\delta^{18}O$, and Os-Os), as well as HSE (Os, Ir, Ru, Pt, Pd, and Re), major elements, and trace elements to constrain the sources for the parental magmas for the Lower Zone of the RLS. More specifically, these geochemical systems will be used to determine whether the high $\delta^{18}O$ values reported for the RLS comes from a recycled crustal component present in the mantle (e.g., E-SCLM) or is caused by upper crust assimilation. This study will use all geochemical systems mentioned above, but a primary focus will be on oxygen and Os isotopes for the NG2 suite, as the contemporaneous use of both of these isotopic systems provides the best opportunity to determine the sources of Lower Zone magmas.

2. Bushveld Complex Background

The Bushveld Complex was discovered in the 1860's by Carl Mauch (Harger, 1934; Cawthorn, 2015). It is located in north-eastern South Africa and contains the largest LMI in the world, the RLS, which has a total surface area of ~65,000 km^2 and an original thickness of 7-9 km (e.g. Eales and Cawthorn, 1996). It is an exceptionally important source for ore deposits as it hosts the majority of the Earth's PGE as well as abundant Cr and V ores in massive oxide layers (Vermaak, 1995; Cawthorn, 1999b; Barnes et al., 2010). The Bushveld Complex also contains the Rooiberg volcanics and the Lebowa Granite Suite (LGS) (Schweitzer et al., 1997; Buchanan et al., 2002; Kinnaird, 2005; Lenhardt and Eriksson, 2012; Cawthorn, 2015). The Rooiberg volcanics are the earliest phase of the Bushveld Complex and, in some areas of the RLS, comprise the floor and roof rocks (e.g. Buchanan et al., 2002). The Rooiberg volcanics are a ~6 km thick succession of silicic volcanic rocks aged at 2061 $\pm$ 2 Ma, which originally covered an area greater than 200,000 km^2, however only 50,000 – 67,000 km^2 remains presently due to erosion (e.g. Walraven, 1997; Buchanan et al., 2002; Lenhardt and Eriksson, 2012). Further, the Rooiberg volcanics are made up of alternating rhyolites, basalts, andesites, and felsites, as well as some interbedded sediments, and units of shale and greywacke (e.g. Twist and French, 1983; Twist, 1985; Harmer and Farrow, 1995; Hatton and Schweitzer, 1995; Schweitzer et al., 1995; Buchanan et al., 2002; Lenhardt and Eriksson, 2012). The LGS, on the other hand, followed the emplacement of the RLS (LGS: 2054 $\pm$ 2 Ma), and is comprised of the Nebo, Makhutso, Bobbejaankop, Lease, and Klipkloof granites (Walraven and Hattingh, 1993; Hill et al., 1996). Additionally, the LGS is ~1.5 – 3 km thick and has an area of 30,000 km^2 (e.g. Molyneux and Klinkert, 1978; MacCaskie, 1983; de Beer et al., 1987; Kleemann and Twist, 1989; Walraven and Hattingh, 1993; Hill et al., 1996; Kinnaird, 2005).

Several geochronology studies, utilizing the U-Pb geochronometer, have focused on the Bushveld Complex in order to determine its age and the timing of emplacement (Buick et al., 2001; Scoates and Friedman, 2008; Olsson et al., 2010). Buick et al. (2001) determined an age of 2058.9 $\pm$ 0.8 Ma by dating titanite within a completely retrogressed xenolith. Scoates and Friedman (2008) utilized the U-Pb system on zircon crystals within Merensky Reef pyroxenites, giving an age of 2054.4 $\pm$ 1.3 Ma. Further, Olsson et al. (2010) determined the age of a Marginal

Zone norite from ~30 km west of Lydenburg, dating at 2057.7 ± 1.6 Ma. The duration of emplacement of the Bushveld is not well constrained, however, with estimates ranging from 75 Ka up to 5 Ma (Cawthorn and Walraven, 1998; Cawthorn and Webb, 2013; Zeh et al., 2015). Zeh et al. (2015) suggests emplacement and cooling for the Bushveld to be less than 1 Ma based on zircon ages of rocks from all RLS Zones. Additionally, this model age was determined by utilizing the a single monolithic magma chamber (Zeh et al., 2015; Robb and Mungall, 2020). Further, Robb and Mungall (2020) determined that it would take 1.2 Myr to crystallize zircon in a single monolithic magma chamber. However, the ages of zircon in the middle of the Critical Zone of the RLS are older than the rest of the LMI. This has led to the introduction of a model where the RLS formed "out-of-sequence," meaning that the RLS formed through the stacking, or the injection into pre-existing sills, of sheet-like intrusions that solidified as separate bodies (Mungall et al., 2016; Robb and Mungall, 2020). The duration for emplacement and cooling of the RLS by way of the "out-of-sequence" model is estimated to be at least 0.6 Myr (Mungall et al., 2016).

The Bushveld has four major limbs that crop out on the surface: the Far Western, Western, Eastern, and Northern, as well as one major limb that has been detected but is not at the surface, the Southeastern or Bethal limb (Figure 2) (Eales and Cawthorn, 1996). The Western limb and the Eastern limb are both ~200 km long, in which the Western limb stretches from near Thabazimbi to just north of Pretoria, and the Eastern limb extends from Stoffberg to Chuniespoort (Figure 2) (Eales and Cawthorn, 1996).

There are five main zones that comprise the RLS, the Marginal, Lower, Critical, Main, and Upper Zones (e.g. Eales and Cawthorn, 1996; Cawthorn, 2015). For the purposes of this study, the Rustenburg layered suite will be referred to as the Bushveld Complex, or simply Bushveld. Marginal Zone rocks are poorly layered fine- to medium-grained norites depleted in incompatible elements (Cawthorn, 2015). The Lower Zone sits atop the Marginal Zone and is composed of alternating successions of layered pyroxenites, dunites, and harzburgites (Eales and Cawthorn, 1996; Cawthorn, 2015). Next is the Critical Zone, which is subdivided into lower and upper Critical Zones. The lower Critical Zone is composed of cumulate pyroxenites in addition to layers of olivine-rich cumulates and chromitites, whereas the upper Critical Zone is defined by the first occurrence of cumulus plagioclase and made up of cyclic units comprising chromitite,

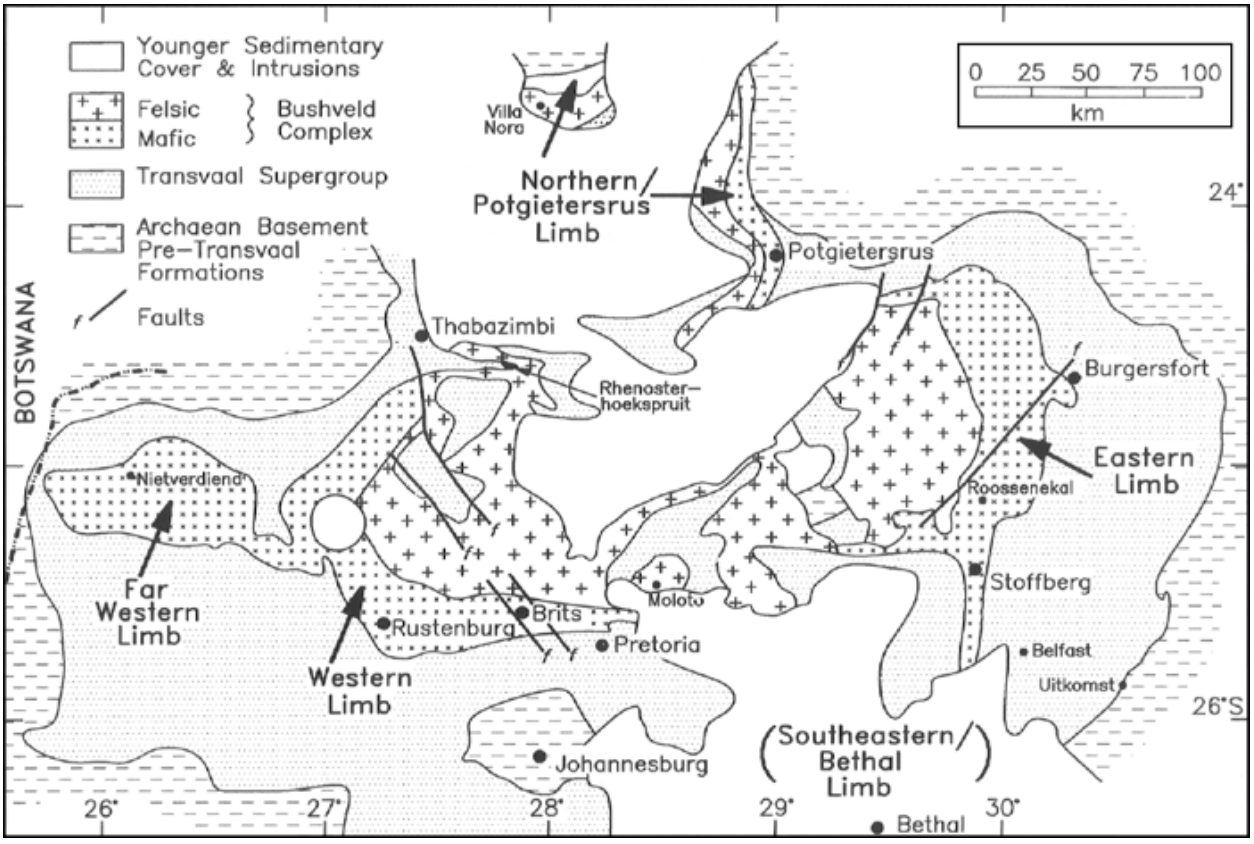

Figure 2. Map of the Bushveld Complex showing the locations of the major limbs, the Far Western, Western, Eastern, Northern, and the Southeastern (Bethal). The figure also shows the locations for the pre-Bushveld Archaean basement, Transvaal Supergroup, and the sedimentary cover that post-dates the Bushveld Complex. Major faults of the Bushveld are also shown. Figure modified slightly from Eales and Cawthorn (1996).

harzburgite, pyroxenite, norite, and anorthosite (Eales and Cawthorn, 1996). The Main Zone sits atop the Critical Zone, and is primarily comprised of norite and gabbronorite with some layers of pyroxenites and anorthosites (Eales and Cawthorn, 1996). The Upper Zone is the uppermost zone of the Bushveld and is comprised of magnetitite, anorthosite, ferrogabbro, troctolite, olivine diorite, and magnetite-rich diorite (Eales and Cawthorn, 1996; Cawthorn, 2015).

2.1 Parental magmas

Chilled margin rocks associated with layered intrusions are often interpreted to represent the original parent magma, as they are the first rocks to crystallize from a magma, following contact with country rock. However, several formation processes of chilled margin rocks force the compositions of these rocks to deviate from the composition(s) of parental magma(s). These processes include, but are not limited to, the first magmas to crystallize were likely affected by

fractional crystallisation, the increased degree of equilibrium further from the country rocks, and increased abundance of cumulus rocks farther from the country rocks (Wilson, 2012). Additionally, the Bushveld Marginal Zone has been interpreted as representative of the Bushveld parental magma, however, varying compositions, grain sizes, and thicknesses contest that this zone of the Bushveld does not represent the parental magma (Cawthorn, 2015).

The most well-supported composition for parental magmas to the Bushveld come from four different rock types associated with various marginal rocks, sills, and dikes, and are termed Bushveld 1 (B1), B1-Ultramafic (B1-UM), B2, and B3 magmas/rocks (Sharpe, 1981; Harmer and Sharpe, 1985; Sharpe and Hulbert, 1985). These rocks were originally found beneath the Bushveld, east of Rustenburg, and are similar to the sills described by Willemse (1969) (Davies, 1980; Cawthorn, 2015). The B1, B2, and B3 rocks are thought to be parental to the Lower Zone and lower Critical Zone, the upper Critical Zone, and the Main Zone, respectively (Davies and Tredoux, 1985; Harmer and Sharpe, 1985; Sharpe and Hulbert, 1985; Maier and Barnes, 1998; Barnes et al., 2010; Godel et al., 2011). Further, the B1-UM rocks are interpreted as parental to the B1 rocks (Barnes et al., 2010). The B1 rocks, also referred as U-magma (Irvine and Sharpe, 1982), are rocks characterized by an enrichment in LREE and contain high Mg contents (Sharpe, 1981; Maier and Barnes, 1998). The Lower Zone parental magma, B1 magma, is hypothesized to have formed from partial melting of the lithospheric mantle with varying (lower, middle, upper) continental crust components (Hickey and Frey, 1982; Lambert et al., 1994; Maier and Barnes, 1998). Further, the upper Critical Zone and Main Zone parental magmas, B2 and B3 magmas, also termed A-type magmas (Irvine and Sharpe, 1982), are Al-tholeiitic basalts that share similar major and trace element compositions (Maier and Barnes, 1998). However, B2 magmas are relatively enriched in REE in comparison to B3 (Maier and Barnes, 1998). The B2 and B3 magmas are thought to have formed from either (1) a mantle-derived magma that assimilated crustal material (Lambert et al., 1994; Maier and Barnes, 1998) or (2) from partial melting of the lower crust comprised of mafic materials (Simmons and Hanson, 1978; Irvine and Sharpe, 1982; Taylor et al., 1984; Hatton, 1995b; Maier and Barnes, 1998). Further, it has been argued that a komatiitic magma represents the initial parental magma for the Bushveld (e.g. Eales and Costin, 2012; Wilson, 2012; Cawthorn, 2015). Wilson (2012) suggests that a komatiite with 19 wt% MgO is the

parental magma, however, a magma with this composition would crystallize olivine before orthopyroxene, forming a dunite layer before a pyroxenitic (Cawthorn, 2015). What is observed for the Lower Zone, however, is an initial pyroxenite layer, not dunite (Cawthorn, 2015). Furthermore, it is suggested that more than one parental magma was emplaced into a staging magma chamber, all of which are enriched in Cr, MgO, and SiO_2 (e.g. Cawthorn, 2015).

Subsequent parental magmas with repeated injections are thought to fill the hypothesized staging magma chamber at depths corresponding to 4.5 – 10 kbars (Wager and Brown, 1968; Eales and Costin, 2012; Cawthorn, 2015). A parental magma with 13 wt.% MgO is thought to be parental to the Lower Zone and lower Critical Zone (Cawthorn, 2015). Additionally, the upper Critical Zone may have had a different parental magma(s) than the Lower Zone and lower Critical Zone (Harmer and Sharpe, 1985; Cawthorn, 2015). This is supported by the presence of cumulus plagioclase and an increase in the initial Sr isotope ratio (Cawthorn, 2015). The Lower Zone is the focus of this study, in which the compositions and other characteristics of this zone will provide insight into the reservoir sources for Lower Zone magmas, including the mantle source(s).

2.2 Mantle Source

As previously noted, the B1, B2, and B3 rocks that come from marginal rocks, sills, and dikes are currently the best representative rocks for the parental magmas (Sharpe, 1981; Harmer and Sharpe, 1985; Sharpe and Hulbert, 1985; Cawthorn, 2015). Further, it is thought that the B1 rocks were sourced from lithospheric mantle partial melts with a crustal component, and the B2 and B3 rocks have two potential formation histories: (1) mantle-derived magma with a crustal component, and (2) lower crust partial melts (Simmons and Hanson, 1978; Hickey and Frey, 1982; Irvine and Sharpe, 1982; Taylor et al., 1984; Lambert et al., 1994; Hatton, 1995b; Maier and Barnes, 1998). Despite the well-held agreement that these rocks are currently the best approximation for Bushveld parental magmas, the mantle sources for these magmas continue to be scrutinized. The hypothesized mantle sources for Bushveld magmas include: (1) a deep-mantle plume (e.g. Hatton, 1995a; Hatton and Schweitzer, 1995; Zirakparvar et al., 2019), (2) the asthenosphere (e.g. Olsson et al., 2011; Rajesh et al., 2013; Maier et al., 2016), and (3) the SCLM

(e.g. Carlson et al., 1999; Maier and Barnes, 2004; Richardson and Shirey, 2008; Olsson et al., 2011; Wilson, 2012; Rajesh et al., 2013; Zirakparvar et al., 2014; Harris et al., 2015; Zeh et al., 2019). In addition to these mantle sources, there is debate on the role and extent of crustal assimilation/contamination in Bushveld magmas (e.g. Maier et al., 2000; Harris et al., 2005; Eales and Costin, 2012). First, I will discuss the mantle sources and then crustal contamination of the Bushveld.

The first mantle source to be discussed is a deep-mantle plume, which several studies have supported for the Bushveld parent magmas (e.g. Hatton, 1995a; Hatton, 1995b; Hatton and Schweitzer, 1995; Olsson et al., 2011; Zeh et al., 2015; Zirakparvar et al., 2019). Evidence for a deep-mantle plume primarily comes from Lu-Hf isotope measurements of zircons (Zirakparvar et al., 2014; Zirakparvar et al., 2019), in addition to the short emplacement time, bulk composition of the proposed parental magmas of the Bushveld (Zirakparvar et al., 2019), and the geometrical relationship of the Bushveld to that of an impinging plume head (Hatton, 1995a; Hatton and Schweitzer, 1995). The $\varepsilon Hf_{(2.06\ Ga)}$ values for Bushveld-related intrusions range from $\varepsilon Hf = -20.7$ to -2.7 (Zirakparvar et al., 2019). Additionally, the most radiogenic εHf values for the Bushveld are near to primordial, $\varepsilon Hf = 0$, suggesting that source of heat for the Bushveld came from the deep mantle (Zirakparvar et al., 2019). The deep-mantle plume hypothesis is also supported by Hatton (1995), in which they suggest that the combination of (1) an elliptical distribution of inferred feeder zones (Sharpe et al., 1981), (2) the intracratonic granites could have originated from a hotspot (Sawkins, 1984), and that (3) a pluton may have been halted by the upper 10 – 20km of the crust (Glazner, 1994).

Asthenospheric derivation of Bushveld magmas is supported by several authors (e.g. Olsson et al., 2011; Rajesh et al., 2013; Maier et al., 2016). Radiating dykes that converge to a focal point in the Eastern limb are evidence for the emplacement of an asthenospheric plume for the Bushveld (Olsson et al., 2011). Additionally, Rajesh et al. (2013) provide a model in which three separate magma pulses from the asthenosphere intruded through the SCLM and crust, were emplaced in a staging magma chamber, later to form the Bushveld. The second of these magmatic injections formed the main Bushveld Complex *sensu stricto* (Rajesh et al., 2013). This model focuses on the major and trace elements, and titanite U-Pb isotopes of low- and high-Ti

rocks from Bushveld-related bodies, where support for an asthenospheric magma source is given from high Nb/La ratios (Rajesh et al., 2013). Further, the chilled margin of the Bushveld is suggested to have a parental magma derived from the asthenosphere, with andesitic or komatiitic composition (Maier et al., 2016). This is supported by the low abundances of high field strength elements (HFSE) for the chilled margin samples (Maier et al., 2016). In addition to parental magmas derived from either the deep mantle or the asthenosphere, it has been suggested that these parental melts interacted with the SCLM.

Bushveld magmas, that were either sourced from the deep mantle or the asthenosphere, have been suggested to have an SCLM component that was incorporated as the magmas rose from the convecting mantle (e.g. Carlson et al., 1999; Maier and Barnes, 2004; Richardson and Shirey, 2008; Olsson et al., 2011; Wilson, 2012; Rajesh et al., 2013; Zirakparvar et al., 2014; Harris et al., 2015). There are two distinct SCLM types, the eclogitic SCLM (E-SCLM) and the harzburgitic, or peridotitic, SCLM (H-SCLM) (e.g. Richardson and Shirey, 2008; Richardson et al., 2009). These two SCLM-types are brought to the surface of Earth as mantle xenoliths through kimberlite eruptions (e.g. Pearson et al., 1995a; Shirey et al., 2001; Jacob et al., 2003; Arndt et al., 2009; Shu et al., 2019). Rhenium-osmium analyses on Premier kimberlite xenoliths suggest a SCLM component that may have been added or was modified from the Bushveld event, which suggests that the Bushveld may have interacted with SCLM material (Carlson et al., 1999). Additionally, the Bushveld has some of the highest Pt/Pd ratios for large magmatic events, and based on its Pt/Pd and the Pd/Ir ratios, the Bushveld may have assimilated the SCLM (Maier and Barnes, 2004). Richardson and Shirey (2008) investigated the Re-Os compositions for diamond-bearing sulphide inclusions from the Venetia and Premier kimberlites. The sulphide inclusions have not interacted with the crust nor have been altered post-emplacement, making them useful in determining the Re-Os compositions of the SCLM beneath the Kaapvaal Craton (Richardson and Shirey, 2008). Although the kimberlites are much younger than the Bushveld Complex (Venetia: 0.5 Ga; Premier: 1.2 Ga), the diamonds themselves are ~2 Ga, similar in age to the Bushveld (Richardson and Shirey, 2008). This makes the ~2 Ga sulphide inclusions within the diamonds a good representation for the Re-Os composition of the upper mantle at the time of Bushveld emplacement (Richardson and Shirey, 2008). The radiogenic γOs_i values for eclogite sulphide

inclusions indicate that the E-SCLM was present at the time the Bushveld was being emplaced (Richardson and Shirey, 2008). The sulphide inclusions that originate from an eclogitic source have characteristically high radiogenic $^{187}Os/^{188}Os$ ratios, up to $^{187}Os/^{188}Os$ = 52.3 (Richardson and Shirey, 2008). Richardson and Shirey (2008) then suggest that since the Lower Zone rocks of the Bushveld have much higher magnesium compositions, these rocks were sourced, in part, by a peridotitic upper mantle reservoir (H-SCLM) and the Main Zone rocks have an eclogitic component (E-SCLM) due to the high aluminous character of these rocks. In addition to their models for asthenospheric-derived magmas to form the Bushveld, Olsson et al. (2011) and Rajesh et al. (2013) support the idea that the Bushveld interacted with the SCLM before emplacement in the crust. Further, Hf isotopes, which suggest a deep-mantle origin for the Bushveld magmas (i.e. Zirakparvar et al., 2019), have unradiogenic $\varepsilon Hf_{(2.06\ Ga)}$ values for the Bushveld and related intrusions (-20.7 to -2.7), which supports an enriched mantle component for the Bushveld, such as the SCLM (Zirakparvar et al., 2014).

2.3 Crustal contamination and oxygen isotopes correlation with radiogenic isotopes

In addition to the mantle sources and an SCLM component for Bushveld rocks, many authors support the idea that Bushveld magmas assimilated parts of the crust, although the degree of crustal assimilation is not well constrained, in which 20 – 41% assimilation of crust has been proposed (e.g. Barnes, 1989; Harmer et al., 1995; Maier et al., 2000; Barnes and Maier, 2002; Buchanan et al., 2002; Buchanan et al., 2004; Harris et al., 2005; Eales and Costin, 2012; Maier et al., 2016; Zeh et al., 2019). Further, Zeh et al. (2019) propose that if the asthenosphere contributed to the B1 magmas, as low as 5% contribution from the crust is required if the lower crust is highly enriched in incompatible trace elements. Support for a crustal component in the Bushveld magmas comes from elevated $\delta^{18}O$ in Bushveld rocks (Harris et al., 2005). Such elevated $\delta^{18}O$ can only be formed by incorporation of crustal material into the Bushveld magmas. Bushveld rocks contain $\delta^{18}O$ values that range from 5.70 – 7.80‰, with most falling between 6.00 – 7.00‰, which is higher than the accepted primary mantle value of ~5.70‰ (Mattey et al., 1994; Eiler, 2001; Harris et al., 2005). Harris et al. (2005) investigated the $\delta^{18}O$ compositions for plagioclase, orthopyroxene, and olivine separates throughout the RLS stratigraphy. It was demonstrated that

~20% upper crustal contamination, and potentially up to 36% to 41% contamination from the lower to middle crust, is required to explain the elevated $\delta^{18}O$ values in Bushveld rocks (Harris et al., 2005). Further, it should be noted that H-isotope compositions demonstrate that these elevated $\delta^{18}O$ values for the Bushveld are of magmatic origin and is not caused by fluid-rock interactions or by alteration (Harris et al., 2005). In addition to assimilation modelling based on oxygen isotopes, crustal contamination has been modelled by trace element concentrations, and Sm-Nd and Rb-Sr isotopes (Maier et al., 2000). These models suggest that the Lower Zone assimilated 10-30% with 5% partial melting of the upper crust, whereas the Main Zone assimilated 40-50% upper crust (Maier et al., 2000). Further, if 12% partial melting of upper crust occurred for the Lower Zone, more contamination by the upper crust is required (Maier et al., 2000). Models supporting 10 – 30% assimilation of upper crust are in agreement with 20-30% crustal contamination by a komatiitic magma, modelled by major element compositions and mineral phase relations in a staging magma chamber between depths corresponding to 4.5 – 10 kbars (Eales and Costin, 2012).

2.4 Karoo LIP & Bushveld relationship

The Karoo LIP and Bushveld Complex, are proximal to one another in southeast Africa (Figure 1) and share similar isotopic characteristics (Ellam and Cox, 1989; Maier et al., 2000; Harris et al., 2005; Ellam, 2006; Jourdan et al., 2007; Zirakparvar et al., 2014; Harris et al., 2015; Zirakparvar et al., 2019). In particular, Tuli and Mwenezi high-Ti picrites share similar elevated $\delta^{18}O$ values to the Bushveld (Harris et al., 2005; Harris et al., 2015). Karoo Tuli and Mwenezi olivine and orthopyroxene separates have $\delta^{18}O$ = 6.00 - 6.70‰, which are similar to the Bushveld, $\delta^{18}O$ = 5.70 - 7.80‰, although $\delta^{18}O$ values for Karoo picrites are less variable than Bushveld samples (Harris et al., 2005; Harris et al., 2015). In addition to similar enriched $\delta^{18}O$ values, the two LIP's share overlapping εNd_i values (Karoo: ~-9.4 to 5.0; Bushveld: ~-7.6 to -5.1) and initial Sr ($^{87}Sr/^{86}Sr_i$) isotope values (Karoo: ~0.704 to 0.708; Bushveld: ~0.704 to 0.709) (Ellam and Cox, 1989; Maier et al., 2000; Jourdan et al., 2007). More specifically, εNd_i values for the Bushveld have the best overlap with Karoo high-Ti picrites from Botswana and Zimbabwe, in which εNd_i = -0.3 to -9.4 (Jourdan et al., 2007). Further, εHf_i isotope values for the Karoo high-Ti picrites (εHf_i

370 = -8.1 to -4.7) overlap with Bushveld εHf values (εHf_i = -12.8 to -6.1), as well as εHf values for a
371 variety of intrusions related to the Bushveld (εHf_i = -20.7 to -2.7) (Jourdan et al., 2007; Zirakparvar
372 et al., 2014; Zirakparvar et al., 2019). The shared elevated $\delta^{18}O$ values, and similar εNd_i, $^{87}Sr/^{86}Sr_i$,
373 and εHf_i values suggests that the Karoo and the Bushveld may have shared an enriched mantle
374 source or a source that formed through a similar process, despite the large difference in ages
375 between them (Karoo: ~183 Ma; Bushveld: ~2.05 Ga) (Harris et al., 2015).
376 Although the Karoo and Bushveld share similar $\delta^{18}O$, εNd_i, $^{87}Sr/^{86}Sr_i$, and εHf_i isotopic
377 values, their Os isotope compositions vary. Karoo picrites have γOs_i isotope values that range
378 from -2.0 to +12.1, whereas Bushveld γOs_i values are typically much higher (+12.7 to +71.4),
379 although reported γOs_i values for the Merensky Reef are as low as γOs_i = +1.8, but have a large
380 range: γOs_i = +1.8 to +56.7 (Ellam et al., 1992; McCandless et al., 1999; Schoenberg et al., 1999;
381 Reisberg et al., 2011). Further, non-Merensky Critical Zone data (for both Eastern and Western
382 limbs) and Platreef γOs_i values range from γOs_i = +10.4 to +39.1 and γOs_i = +46.0 to +71.4,
383 respectively (McCandless et al., 1999; Reisberg et al., 2011). Despite this isotopic difference
384 between the two LIP's, the unradiogenic Os isotope compositions for the Karoo clearly suggest a
385 SCLM component to the parent magmas (Ellam et al., 1992), however, no such unradiogenic Os-
386 isotopes have been previously reported for the Bushveld Complex.
387 Sourcing melts from the E-SCLM would result in higher-than-mantle $\delta^{18}O$ and radiogenic
388 γOs_i values (e.g. MacGregor and Manton, 1986; Shirey et al., 2001; Richardson and Shirey, 2008;
389 Harris et al., 2015). Alternatively, an H-SCLM source would result in peridotite mantle ($\delta^{18}O$ =
390 5.50‰) or MORB-like ($\delta^{18}O$ = 5.70‰) $\delta^{18}O$ and unradiogenic γOs_i values (e.g. Pearson et al.,
391 1995a; Pearson et al., 1995b; Eiler, 2001). The similarities in high $\delta^{18}O$ values for both Karoo and
392 Bushveld rocks has been suggested to represent a long-lived elevated $\delta^{18}O$ mantle source
393 beneath these provinces, likely a heterogeneous H-SCLM/E-SCLM source (Harris et al., 2015). This
394 is further supported by $\delta^{18}O$ values measured for eclogitic xenoliths from the Kaapvaal craton,
395 which span a large range of $\delta^{18}O$ values (1.40 – 8.00‰), but which also overlap with $\delta^{18}O$ values
396 reported for the Bushveld and Karoo (MacGregor and Manton, 1986; Schulze et al., 2000; Harris
397 et al., 2005; Harris et al., 2015; Riches et al., 2016; Radu et al., 2019). These high $\delta^{18}O$ values for

398 the Bushveld correlate with relatively-radiogenic γOs_i compositions from the Critical Zone and
399 the Platreef (McCandless et al., 1999; Schoenberg et al., 1999; Reisberg et al., 2011).
400 These provinces could have assimilated portions of the crust as they were emplaced (e.g.
401 Ellam and Cox, 1989; Maier et al., 2000; Harris et al., 2005). However, the high-Ti Karoo rocks,
402 which have more similar compositions to the Bushveld than the low-Ti rocks, likely did not
403 assimilate the crust (e.g., Jourdan et al., 2007). Yet, the low-Ti Karoo samples require only a minor
404 degree of crustal assimilation, as these rocks are also interpreted to have a significant SCLM
405 component (Jourdan et al., 2007). The Karoo high-Ti basalts contain more Sr than the crust and
406 have well-constrained, and restricted, MgO values, which suggests that crustal assimilation did
407 not play a primary role in the petrogenesis of these rocks (Ellam and Cox, 1989).

3. Highly siderophile elements (HSE) and Re-Os Background

The HSE and Re-Os isotopic system have been utilized to investigate a wide variety of rocks, including, but not limited to: crustal rocks (e.g. Saal et al., 1998; Peucker-Ehrenbrink and Jahn, 2001), divergent margin volcanic rocks (e.g. Gannoun et al., 2007; Yang et al., 2013), convergent margin volcanic rocks (e.g. Alves et al., 2002; Bezard et al., 2015), intraplate volcanic rocks (e.g. Schoenberg et al., 2003; Day et al., 2010a; Reisberg et al., 2011), mantle xenoliths (e.g. Meisel et al., 2001; Janney et al., 2010), mineral inclusions in diamonds (e.g. Richardson and Shirey, 2008; Wiggers de Vries et al., 2013), Apollo Lunar samples (e.g. Day et al., 2010b; Gleißner and Becker, 2017), and a variety of meteorite types (e.g. Smoliar et al., 1996; Brandon et al., 2005). Within these sample suites, HSE and Re-Os isotopes have been utilized for whole-rock samples (e.g. Chesley and Ruiz, 1998; Day et al., 2008; Puchtel et al., 2009) as well as mineral separates and single grain mineral inclusions in diamonds (e.g. Stein et al., 1997; Pearson et al., 1999; Barra et al., 2003; Richardson and Shirey, 2008). These analytical techniques have proven useful for economic deposits because they allow for an in-depth characterization of the parental magmas, contamination and assimilation sources, fractionation trends, and processes that act on the magmas pre- and post-crystallization (Day, 2013). Significant economic deposits in which HSE and/or Re-Os techniques have been applied include the Stillwater Complex (e.g. Barnes et al., 2016; Day and O'Driscoll, 2019), Sudbury Igneous Complex (e.g. Walker et al., 1991; Morgan et al., 2002), Noril'sk Ni-Cu-PGE deposits (Walker et al., 1994; Malitch and Latypov, 2011), the Great Dyke (Schoenberg et al., 2003), the Bushveld Complex (e.g. McCandless and Ruiz, 1991; McCandless et al., 1999; Schoenberg et al., 1999; Reisberg et al., 2011), among other important economic deposits (see Barnes and Ripley, 2016). The major objective of this study is to constrain the source characteristics and possible contamination by crustal and/or upper mantle materials for the Bushveld, utilizing HSE and the Re-Os systems, as well as more traditional techniques (i.e. major and trace elements, $\delta^{18}O$, Rb-Sr, and Sm-Nd).

3.1 Highly siderophile elements (HSE)

The HSE are particularly useful to determine the most recent processes (i.e. post-emplacement alteration, magmatic degassing, fractional crystallization, and partial melting) that

have acted on magmas and rocks (Day, 2013), and consist of the PGE (Os, Ir, Ru, Rh, Pt, and Pd) as well as Au and Re. These elements have varying compatibilities in the crystallizing phase from a silicate melt, with Os, Ir, Ru, and Rh being highly compatible, Pt and Pd moderately compatible, and Re and Au relatively incompatible (Day, 2013).

Previous partitioning experiments for the HSE, other than metal and sulphide phases, have focused on spinel, and silicate phases, particularly olivine (Brenan et al., 2016). Overall, Ir, Ru, and Rh have higher compatibilities in the spinel phase than Pt, Pd, Au, and Re (Brenan et al., 2016). Ruthenium is the most compatible in Cr-spinel, with a $D^{mineral/melt}$ = ~4 (D is the partition coefficient for a mineral, spinel in this case, with respect to the melt/magma), Rh and Ir have a range of $D^{mineral/melt}$ = 0.04 – 1, and Pt and Pd are the least compatible in spinel ($D^{mineral/melt}$ < 0.2) (Brenan et al., 2012). Previous studies to Brenan et al. (2012) report higher D-values for Ru (~20 - <4000), Rh (~80 - 300) in spinel and magnetite (Capobianco and Drake, 1990; Capobianco et al., 1994), and Pd (<1), Ir (5 – 10,000), Au (0.08), and Re (0.0012 – 0.21) in Cr-spinel (Righter et al., 2004). Within olivine, Ir, Ru, and Rh are moderately compatible and Pt, Pd, Au, and Re are incompatible (Brenan et al., 2016). In addition to their compatibilities in spinel and olivine, these elements are strongly chalcophile (sulphur-loving) in the absence of Fe-rich metal phases (siderophile behaviour) (Day, 2013). The partition coefficients (D) for these elements in a sulphide liquid are much greater than the silicate liquid, with minimum $D^{SulLiq/SilLiq} > 10^5$ ($D^{SulLiq/SilLiq}$ is the partition coefficient for sulphur liquid with respect to silicate liquid) for the HSE (Brenan et al., 2016; Day and O'Driscoll, 2019). Further, Os, Ir, Ru, and Pt have $D^{SulLiq/SilLiq}$ values corresponding to ~10^5, ~10^7, ~10^8, and ~10^9, respectively (Andrews and Brenan, 2002; Fonseca et al., 2009; Fonseca et al., 2012; Mungall and Brenan, 2014; Brenan et al., 2016).

Some processes that have effects on the concentration and fractionation of HSE include post-emplacement alteration, degassing, fractional crystallization, and partial melting (e.g. Day, 2013). Contamination from the crust has less of an impact on the abundances of HSE than fractional crystallization (Chazey and Neal, 2005; Ireland et al., 2009; Day, 2013). The reason that contamination has less of an impact on HSE than fractional crystallization is that contamination, particularly from <20% contamination of the crust, dilutes the HSE abundances rather than altering the relative abundances (Chazey and Neal, 2005; Ireland et al., 2009; Day, 2013). Due to

466 the dilution effect that contamination from the crust exhibits, HSE sourced from the
467 asthenosphere or SCLM may be preserved (Ireland et al., 2009; Gannoun et al., 2016). The first
468 process to be discussed that affects HSE abundances and concentrations is post-emplacement
469 alteration, which includes alteration from metamorphism, high- and low-temperature fluids,
470 leaching, and anthropogenic effects, although this last process is easily avoidable by proper
471 collection and preparation techniques (Day, 2013). Anthropogenic effects include contamination
472 from saw blades, hammers, etc. (Day, 2013). Samples that are impacted by post-emplacement
473 alteration processes are commonly found at or near the surface, in metamorphic terrains, and
474 are relatively old (Day, 2013). Further, samples that have low HSE abundances are more easily
475 affected by these processes (Day, 2013). Magmatic degassing is an additional process that
476 impacts the concentration of HSE due to the HSE being relatively volatile, as well as effects from
477 magma composition, partial melting, abundance of sulphides, and fO_2 (Day, 2013). The HSE can
478 potentially enter the vapour phase and be removed from the magma during emplacement (Day,
479 2013). Fractional crystallization of a magma causes variations in HSE abundances due to the
480 varying compatibilities of the HSE (Day, 2013). During crystallization of a magma, compatible to
481 relatively compatible HSE (Os, Ir, Ru, and Rh) are sited within various crystallizing phases,
482 including spinel, olivine, and other trace phases (Day, 2013). The remaining HSE (Pt, Pd, Au, and
483 Re) range from relatively compatible to relatively incompatible and are more likely to remain in
484 the melt with respect to Os, Ir, Ru, and Rh (Day, 2013). Partition coefficients for these elements
485 are also important during fractional crystallization, as a metal-rich or sulphide liquid is more likely
486 to contain the HSE than silicate phases (Day, 2013; Brenan et al., 2016). Partitioning of HSE is
487 complex and can be affected by many conditions and processes, including the aforementioned
488 processes, as well as by temperature, pressure, fO_2, and fS_2 (sulphur fugacity) differences (Day,
489 2013).

490 Various reservoirs have unique HSE characteristics, where the upper continental crust is
491 characterized by relatively depleted Os (0.031 ppb), Ir (0.022 ppb), and is relatively enriched in
492 Ru (0.210 ppb), Pt (0.510 ppb), Pd (0.520 ppb), and Re (0.198 ppb) (Peucker-Ehrenbrink and Jahn,
493 2001). The primitive mantle (asthenosphere) has higher abundances of these elements; Re = 0.35
494 ppb, Os = 3.9 ppb, Ir = 3.5 ppb, Ru = 7 ppb, Pt = 7.6 ppb, and Pd = 7.1 ppb (Becker et al., 2006;

Day, 2013). Additionally, the peridotite/harzburgite sub-continental lithospheric mantle (H-SCLM) is relatively depleted in the more incompatible HSE (Re = 0.14 ppb, Pt = 0.18, and Pd = 0.04) and enriched in the more compatible HSE (Os = 3.18, Ir = 1.72, and Ru = 1.42) (Pearson et al., 2004; Day, 2013). Cratonic eclogites, which represent the eclogitic SCLM (E-SCLM) contain lower concentrations of Os (0.33 ppb) than peridotitic xenoliths, which represent the H-SCLM (Aulbach et al., 2016). McDonald and Viljoen (2006) report HSE abundances for eclogite xenoliths from the Botswanan Orapa kimberlite in which the eclogites have lower abundances for Ir and Ru, and higher abundances of Pt and Pd (Ir = 0.19, Ru = 0.39 ppb, Pt = 1.9 ppb, and Pd = 1.2 ppb, Re and Os were not reported), than H-SCLM. Further, Dale et al. (2009) report HSE abundances for basaltic (averages in ppb: Os = 0.008, Ir = 0.007, Ru = 0.026, Pt = 0.112, Pd = 0.055, and Re = 0.397) and gabbroic (averages in ppb: Os = 0.031, Ir = 0.024, Ru = 0.041, Pt = 0.243, Pd = 0.080, and Re = 0.227) eclogites from the Zermatt-Saas ophiolite in Switzerland.

3.2 Re-Os isotopes

In addition to the HSE, which record the most recent processes, the long-lived Re-Os isotopic system ($^{187}Re \rightarrow {}^{187}Os + \beta^-$) has a half-life of ~42 Ga, and is particularly useful for tracking processes that have occurred over long time periods (Day, 2013). The Re-Os system can constrain geochemical reservoirs of interest, such as the crust, primitive mantle, SCLM, and the core-mantle boundary (Day and O'Driscoll, 2019).

The crust, primitive mantle, SCLM, and core-mantle boundary materials each have unique Re-Os isotopic signatures (Day, 2013). Crustal rocks have exceptionally radiogenic $^{187}Os/^{188}Os$ values (>1), which correspond to highly positive γOs_i [~300 for ancient crust (> 2Ga); Shirey and Walker (1998)]. Crustal rocks have such radiogenic values due to the compatibilities of the HSE in magmas (Saal et al., 1998; Day, 2013). As mentioned in section 3.1, Re will preferentially enter the melt and Os will remain in the solid phase. This segregation of Re and Os will cause radiogenic ingrowth of ^{187}Os in rocks that crystallised from the segregated melt, which will force high and positive γOs_i values (e.g. Saal et al., 1998; Day, 2013). Thus, crustal rocks are enriched in Re and depleted in Os, and the decay of ^{187}Re to ^{187}Os causes the radiogenic values that are observed in these rocks (Peucker-Ehrenbrink and Jahn, 2001).

Shirey and Walker (1998) report that the sub-continental lithospheric mantle, also referred to as the continental lithospheric mantle (CLM) or lithospheric mantle, has unradiogenic values ($^{187}Os/^{188}Os$ = 0.105-0.129; γOs_i = -17.3 to +1.6), and these values are in agreement with those reported in Day (2013) ($^{187}Os/^{188}Os$ = <0.13). However, there are two distinct types of SCLM, harzburgitic (peridotitic) and eclogitic, referred to as H-SCLM and E-SCLM, respectively (e.g. Richardson and Shirey, 2008). The H-SCLM is characterized by the aforementioned unradiogenic Re-Os signatures, whereas the E-SCLM has an extremely radiogenic Re-Os composition (Richardson and Shirey, 2008; Richardson et al., 2009). The E-SCLM values given by Richardson and Shirey (2008), by analyses on Venetia and Premier kimberlite sulphide inclusions in diamonds, has initial $^{187}Os/^{188}Os$ values that range from 0.0980 to 0.3154 with an outlier of 27. Most sulphide inclusion $^{187}Os/^{188}Os$ values fall between ~0.2 to 0.3 (Richardson and Shirey, 2008). Additionally, Pearson et al. (1995b) investigated Siberian eclogite xenoliths that have radiogenic $^{187}Os/^{188}Os$ (3.045 and 9.808) that correspond to extremely radiogenic γOs_i values (2072 and 6759), and represent the E-SCLM. In addition to the study by Shirey and Walker (1998), peridotite xenoliths, investigated by Pearson et al. (1995b), have $^{187}Os/^{188}Os$ that typically range from ~0.10 to 0.16 that have unradiogenic γOs_i values (-0.4 to -13). These values correspond to a H-SCLM source for these peridotite samples. Additional analyses on Kaapvaal peridotites (i.e. Pearson et al., 1995a) report initial $^{187}Os/^{188}Os$ (0.1043 – 0.1241) with unradiogenic γOs_i (-16.8 to -0.3), which are in agreement with Pearson et al. (1995b). Further, the SCLM and crust are more likely to contaminate intraplate magmas, so to better understand the HSE characteristics of asthenosphere-derived melts, oceanic basaltic magmas (i.e. MORB and OIB) and some continental flood basalts (CFB) allow us to focus on the HSE characteristics of the asthenosphere (Snow et al., 2000; Gannoun et al., 2016). Asthenospheric magmas, or primitive upper mantle magmas, are typically characterized by $^{187}Os/^{188}Os$ = 0.1296 with a corresponding γOs_i = 0 (e.g. Shirey and Walker, 1998; Day, 2013). However, the asthenosphere is heterogeneous, causing slight variations in Re-Os data (Barnes and Ripley, 2016).

The outer core, and thus the core-mantle boundary, may have slightly more radiogenic values ($^{187}Os/^{188}Os$ = 0.1372; γOs_i = +7.9) than the primitive mantle if the inner core formed early in Earth's history (Shirey and Walker, 1998). Thus, each of these reservoirs (i.e. crust, primitive

mantle, H-SCLM, E-SCLM, and the core-mantle boundary) have different Re-Os compositions, making this isotopic system particularly useful in determining the reservoirs that parental magmas were sourced from, or were contaminated by during magmatic evolution.

In addition to the effects that contamination from various reservoirs have on the Re-Os system, post-emplacement alteration has the potential to complicate HSE concentrations, which may impact Re-Os isotope values in rocks and minerals solidifying from a magma (Day, 2013). Post-emplacement alteration can cause the addition or removal of elements, causing fractionation of the HSE, particularly Re and Os, which would affect the Re-Os isotopic signatures of the samples (Day et al., 2007; Brandon et al., 2012; Day, 2013). The loss of Re and addition of radiogenic Os causes the γOs_i values to be radiogenic (high $+\gamma Os_i$) (Brandon et al., 2012; Barnes and Ripley, 2016). Alternatively, the addition of Re and loss of Os can cause the $^{187}Os/^{188}Os_{initial}$ value to be lower than expected, showing chondritic or unradiogenic γOs_i values (i.e. low $+\gamma Os_i$ or $-\gamma Os_i$) (Barnes and Ripley, 2016).

4. Sampling and Analytical Methods

4.1 Sampling

Samples utilised in this study come from the Nooitgedacht 2 borehole (NG2), of the Western limb in the Bushveld Complex, which was one of three boreholes drilled between 1986-1987 by the Geological Survey of South Africa (Maier et al., 2016). The NG2 borehole intersects through the Lower Zone and the basal contact of the Bushveld (Maier et al., 2016). The lowermost rocks of the borehole (774.70 to 773.60m) are hornfels and the rocks above this

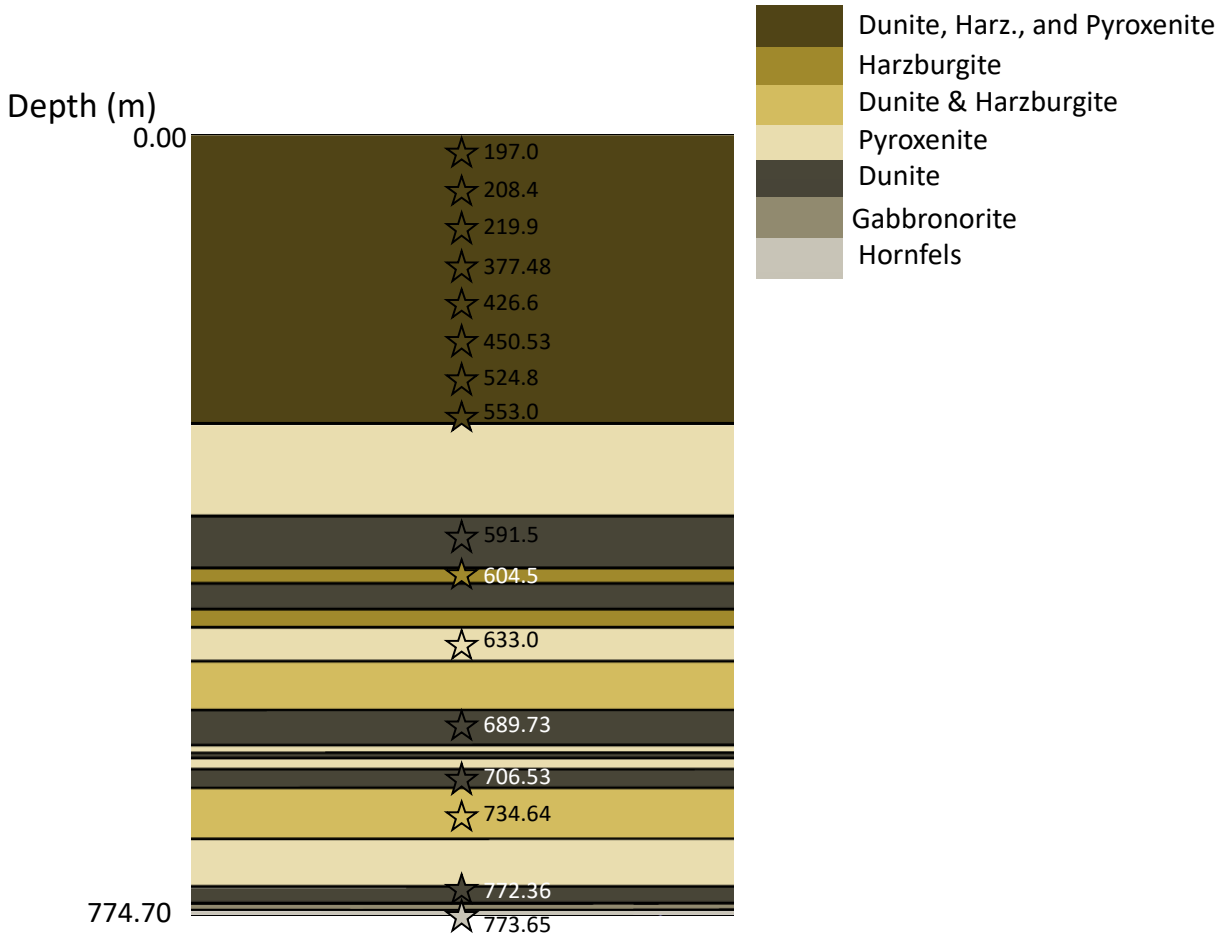

Figure 3. Schematic cross section displaying the lithologies from the NG2 borehole that were logged by B. Teigler, W. J. de Klerk, R. N. Scoon, S. A. Haikney, and W. D. Maier. The lithologies given in the key are not necessarily those for the NG2 suite samples identified by depth in the cross section, rather the lithologies represent the most common rock type in that section of the borehole.

are gabbronorite (773.20 - 773.60m) and fine-grained dunite with a quartzite xenolith (763.45 – 773.20m). Layers above these are alternating dunite, harzburgite, and pyroxenite. Samples

used in this study come from various depths within the borehole. The NG2 borehole was logged by B. Teigler, W. J. de Klerk, R. N. Scoon, S. A. Haikney, and W. D. Maier. Figure 3 is a simplified schematic cross section for the borehole, in which samples from the borehole that are utilised in this study are pointed out. The samples obtained for this study were sourced from Rhodes University rock store, the storage location for the NG2 borehole.

4.2 Petrography

Thin sections made from NG2 samples were observed by transmitted and reflected light microscopy at UCT. Textures were observed through petrographic observations and modal abundances of the samples were determined through point-count analyses, in which 300 points were taken for each thin section.

4.3 Whole-rock trace element abundance measurements

Trace-element abundances were determined at the Scripps Isotope Geochemistry Laboratory (SIGL), Scripps Institution of Oceanography using methods described previously (Day et al., 2017). One hundred milligrams of powder was precisely weighed and digested in a 1:4 mixture of Teflon-distilled HNO3:HF for >72 Hrs at 150˚C on a hotplate. Rock standards (BHVO-2, BIR-1, HARZ-01) and total procedural blanks were prepared with samples. After drying down and sequential HNO_3 dry-down steps to break-down fluorides, clear sample solutions, free of any solid material, were diluted in two sets. The first set was diluted by a factor of 5000 in 2% HNO_3 for all trace element determinations. The second set was diluted by a factor of 1000 for rare earth element determination. Both sets of solution were doped with a 1 ppb In solution to monitor instrumental drift. Solutions were measured using a Thermo Scientific iCAP Qc quadrupole inductively coupled plasma mass spectrometer at the SIGL. Reproducibility of the reference materials was generally better than 5% (RSD) for basaltic and peridotite standards, and element abundances were generally within error of recommended values.

610 **4.4 Major Elements**

611 Thirteen samples from the NG2 borehole were analysed for whole-rock major elements.
612 Major oxides were analysed using X-ray fluorescence spectrometry (XRF). The analyses were
613 carried out using a Panalytical Axios XRF spectrometer in the Department of Geological Sciences,
614 University of Cape Town. Fusion disks were used for XRF major element measurements. The
615 fusion discs were generated by weighing out 2g of sample into a crucible. The crucible was then
616 placed in an oven at 110 °C overnight and weighed afterward to determine wt.% H_2O^- (adsorbed
617 volatile content). The sample was then then roasted at 850 °C for four hours to remove all
618 structural volatiles (e.g., H_2O and CO_2) and oxidise all Fe to Fe^{3+}, and weighed again to determine
619 wt.% loss on ignition (LOI). Flux fusion disks were made using 0.7 g of ignited sample powder
620 added to 6 g of Claisse flux beads containing 57% Li tetraborate- 43% Li metaborate with a small
621 amount of LiBr as a releasing agent. The mixture was then melted and homogenized in a Pt
622 crucible over a gas flame (in a Claisse M4 automated fluxer) and poured into a Pt mold to form a
623 fusion disc.

624 XRF calibration was performed using a series of well-characterised natural rock powder
625 standard reference materials issued by organisations such as MINTEK, the United States
626 Geological Survey and the Geological Survey of Japan, prepared identically as the samples for
627 analysis. In all cases, calibration curves of known concentration versus measured analyte peak
628 intensities corrected for background were used to obtain elemental concentrations in
629 unknowns. Absorption and enhancement effects were corrected through iterative correction
630 routines employing mass attenuation coefficients. Additionally, spectral line overlaps (e.g.,
631 RbK_β on YK_α) were corrected using routines based on spiked blank analyses (e.g., by
632 determining the relationship between RbK_α intensity and RbK_β intensity at the YK_α peak
633 position using samples with variable Rb concentrations and zero Y concentration).

634

635 **4.5 Oxygen isotopes**

636 Oxygen isotope analyses were conducted in the stable isotope laboratory at UCT.
637 Inclusion-free olivine, orthopyroxene, and clinopyroxene separates were hand-picked using an
638 optical microscope with a separate light source. Mineral separates were cleaned using ethanol,

shaken in an ultrasonic bath, and dried. Laser fluorination analyses were conducted on approximately 2-3mg of mineral separates utilising a 20 W New Wave CO_2 laser, mounted on a moveable stage (Harris and Vogeli, 2010). Samples are loaded into a highly polished pure Ni sample holder, which is then placed into an oven at 110°C for an hour, and transferred to the reaction chamber (Harris and Vogeli, 2010). The sample chamber is then pumped for > 2 hours, following the expansion of 10 kPa of BrF_5 into the reaction chamber and then left overnight prior to analyses of the mineral separates (Harris and Vogeli, 2010). Analyses of samples were completed with 10 kPa BrF_5, during which the leftover Br, that formed due to dissociation, was frozen into cold fingers (Harris and Vogeli, 2010). The gases that were not frozen into the cold finger pass through a KCl trap at 200°C to remove any F_2 produced during the reaction process (Harris and Vogeli, 2010). Gasses are then expanded into a stainless steel double-U trap in liquid nitrogen, in which 5 Å molecular sieve in glass storage bottles collect the purified O_2 (Harris and Vogeli, 2010). Before the extraction of any samples, a blank was run, and the amount of gas measured (Harris and Vogeli, 2010).

The oxygen isotope ratios for NG2 samples were measured using a Finnigan Delta XP mass spectrometer in duel-inlet mode on O_2 gas (Harris and Vogeli, 2010). The isotope composition of the O_2 reference gas was determined through the conversion of an O_2 aliquot to CO_2 by utilising the carbon converter on the conventional extraction line (Harris and Vogeli, 2010). The O_2 reference gas composition was utilised to calculate the δ values [$\delta^{18}O = ((^{18}O/^{16}O)_{sample}/(^{18}O/^{16}O)_{standard} - 1) \bullet 1000‰$] for NG2 samples relative to standard mean ocean water (SMOW) (Harris and Vogeli, 2010). An internal standard, garnet from the Monastery kimberlite, is utilised. Further, the reproducibility of the Monastery kimberlite garnet is $\delta^{18}O$ = 0.117‰, which corresponds to a 2σ standard deviation equal to 0.158. These values come from 327 duplicates run from 2008 to present day.

4.6 Neodymium and Strontium isotopes

Rubidium-strontium and samarium-neodymium isotope analyses were performed at the UCT radiogenic isotope laboratory. Approximately 49-51 mg of each sample is weighed into individual Teflon beakers. Following this, 4mL of 4:1 2-bottle distilled (2B) concentrated HF:HNO_3

is added to each sample. The Teflon beakers are then sealed and left to digest on a hotplate at 140°C over the weekend (~70 hours in total). The beakers are then opened and left to dry on the hotplate (140°C), followed by an addition of 2mL of 65% 2B HNO_3 to the remaining residue in each beaker and then the samples are left to dry on the 140°C hotplate with the Teflon beaker lids open. The previous step is repeated. Once all of the samples have been dried, they are cooled down and then 1.5mL of 2M 2B HNO_3 is added and left overnight. The samples are then transferred to 1.5mL centrifuge tubes and spun at 4000 rpm for 20 minutes. Columns for Sr collection are initially conditioned with three rounds of 1mL 2M HNO_3. Samples are loaded and then rinsed with 0.5mL 2M HNO_3 followed by six washes of 0.5mL 2M HNO_3. Strontium is then collected by the addition of 0.5mL of milli-Q (MQ) water six times. The collected Sr is then dried and cooled followed up with the addition of 2mL 0.2% HNO_3 and set on a 100°C hotplate for 10 minutes. Neodymium collection begins with conditioning of columns with 1mL 0.05M HNO_3 twice. Columns are then washed with 0.5mL 0.05M HNO_3 six times. Columns are rinsed with 0.5mL 0.05M HNO_3 twice, followed by the addition of 9mL 0.25M HCl. Neodymium is then collected by the addition of 10mL of 0.25M HCl. The resins Sr.Spec and Ln.Spec are utilised for Sr and Nd isotope collection, respectively, and the columns are arranged in tandem for the separation procedure (after Pin et al., 2014). Isotope measurements utilise a Nu instruments NuPlasma HR mass spectrometer with a DSN-100 desolvating nebuliser. Strontium and Nd isotope values are referenced to values of 0.710255 for the bracketing analysis of NIST SRM987 and 0.512115 for the bracketing analysis of JNdi-1 (after Tanaka et al., 2000), respectively. The Sr isotope data were corrected for interference by Rb using the ^{85}Rb and $^{85}Rb/^{87}Rb$ values. Further, mass fractionation caused by the instrumentation is corrected for with a value of $^{86}Sr/^{88}Sr$ = 0.1194. Additionally, Nd isotope values are corrected for interference caused by Sm and Ce using the measured ^{147}Sm and ^{140}Ce values and the isotopic abundances of Sm and Ce, and mass fractionation caused by the instrument are corrected using the exponential law and $^{146}Nd/^{144}Nd$ = 0.7219.

4.7 Rhenium-osmium isotopes and HSE abundance analyses

Rhenium-Os isotope and highly siderophile element (HSE) abundance analyses were conducted at the University of California – San Diego (UCSD) Scripps Institution of Oceanography (Scripps), in the Scripps Isotope Geochemistry Laboratory (SIGL). Whole-rock samples were ground to fine powders utilizing an alumina grinding container and a shatterbox at the University of Georgia (UGA). At SIGL the powdered samples were precisely weighed, aiming for a mass of 0.7 g, and then loaded into Pyrex Carius tubes along with multiply distilled 15.7M HNO_3 and 12M HCl, and isotopically enriched spikes (^{99}Ru, ^{106}Pd, ^{185}Re, ^{190}Os, ^{191}Ir, ^{194}Pt), and 12 mL of a 1:2 mixture of multiply Teflon distilled HCl and HNO_3 purged of excess Os by repeated treatment and reaction with H_2O_2. The Carius tubes were then sealed, shaken after cooling, and then digested in a convection oven at 270°C for ~72 hours. Carius tubes were then removed from the oven and extracted solutions placed in Teflon vials. Prior to micro-distillation for purification (Birck et al., 1997), Os was triply extracted from the acid using CCl_4, followed by back extraction into HBr (Cohen and Waters, 1996). The other HSE and Re were recovered and purified from the residual solutions utilizing standard anion exchange techniques (Day et al., 2016b).

Osmium isotope compositions were measured using a *ThermoScientific* Triton thermal ionization mass spectrometer in negative-ion mode and in peak-jumping mode on the secondary electron multiplier. Utilising a Cetac Aridus *II* desolvating nebuliser coupled to a *ThermoScientific* iCAPQc ICP-MS, the measurements of Re, Ir, Pt, Pd, and Ru were made. By utilising an oxide correction, iterative fractionation correction using $^{192}Os/^{188}Os = 3.08271$, and assuming an exponential law, a ^{190}Os spike subtraction, and an Os blank subtraction, offline Os corrections were made. Repeated measurements of the UMCP Johnson-Matthey standard determined the precision for $^{187}Os/^{188}Os$, in which the standard was better than ±0.2% (2 SD; 0.1137 ± 8; n = 2). Rhenium, Ir, Pt, Pd, and Ru isotopic ratios for sample solutions were corrected for by mass fractionation using the deviation of the standard average run on the day over the natural ratio for the element. The external reproducibility for HSE analyses was better than 0.5% for 0.5 ppb solutions and all reported values are blank corrected. The procedural blank (n = 1), run with NG2 samples, gave $^{187}Os/^{188}Os = 0.1994 \pm 0.004$, with Re = 0.016 ppb, Pd = 0.017 ppb, Pt = 0.005 ppb, Ru = 0.042 ppb, Ir = 0.002 ppb, and Os = 0.001 ppb. Peridotite standard MUH-1 was run with

NG2 samples as well, in which the concentrations and isotopic compositions for this standard fit within the uncertainty of methods that include Carius tube and high-pressure asher digestion methods (Meisel and Horan, 2016).

5. Results

5.1 Petrography

Modal mineral abundances (mod.%) from point-count analyses are listed in Table 1. All rocks are characterised by cumulate textures. The cumulus textures are split into three categories, orthocumulus, mesocumulus, and adcumulus. These textures are defined by <85% (orthocumulus), 85-95% (mesocumulus), and >95% (adcumulus) cumulus minerals. Poikilitic textures are also observed and characterised by orthopyroxene oikocrysts with olivine chadacrysts. Occasionally, oikocrysts of clinopyroxene, olivine, or biotite are observed with olivine and/or orthopyroxene chadacrysts in the NG2 samples. Further, common interstitial minerals include plagioclase and biotite. Some samples have undergone serpentinization, which has altered olivines, and to a lesser extent, pyroxenes. Opaque minerals include chromite, pyrrhotite, pentlandite, and chalcopyrite. Modal abundances for opaque phases were determined for every sample other than NG2-633.0, which has trace amounts of opaques. Representative photomicrographs for all observed textures, are presented in Figure 4. Below, I describe the petrography of Lower Zone samples with available thin sections. There are several NG2 samples that were not analysed for geochemistry due to sample depletion. Some of these samples had available thin sections, however.

Sample NG2-772.36 is a strongly altered harzburgite. Most olivines have been partially or completely serpentinized, and most pyroxenes have been partially serpentinized. Orthopyroxenes primarily occur as oikocrysts with olivine chadacrysts (Figure 4a & 4b). In addition to serpentine, biotite is commonly present as an alteration phase, but is also an interstitial phase along with plagioclase (Figure 4b). The alteration phase is present near veins of serpentine, whereas the interstitial biotite is surrounded by the primary mineral phases and not located near any alteration phases. Additionally, biotite near serpentine veins, and in samples that have been extensively altered, are typically much larger than the interstitial biotite. Opaque phases (modal abundance = 0.6 mod.%) in this sample are fine-grained ($\leq$ 0.1mm) chromite grains only. No sulphides are observed.

Sample NG2-633.0 is an olivine pyroxenite. There is no observable alteration. This sample displays mesocumulus texture with interstitial plagioclase and biotite (Figure 4c). Biotite also

Table 1. Modal abundances and rock classifications for NG2 samples. The pyroxene field includes both orthopyroxene and clinopyroxene. Samples NG2-450.53 and NG2-377.48 contain 2% and 3.3% clinopyroxene, respectively. Clinopyroxene in these samples occurs as large oikocrysts. NG2-524.8 is comprised of 30.3% clinopyroxene and 3.3% orthopyroxene, making it the most clinopyroxene-rich sample from the NG2 borehole suite. See text for textures and opaque phases present for each sample. Opaque minerals are comprised mostly of chromite, but there are small amounts of pyrrhotite, pentlandite, and chalcopyrite in the NG2 samples.

	olivine	pyroxene	biotite	plagioclase	serpentine	opaques	Rock Classification
NG2-772.36	36.0%	49.6%	3.6%	2.6%	7.3%	0.6%	Harzburgite
NG2-633.0	6.6%	91.0%	0.3%	2.0%	-	-	Olivine Pyroxenite
NG2-604.5	0.6%	96.0%	0.3%	2.6%	-	0.3%	Olivine Orythopyroxenite
NG2-524.8	59.3%	33.6%	-	-	5.3%	1.6%	Olivine Websterite
NG2-450.53	7.0%	87.0%	2.3%	3.0%		0.6%	Orthopyroxenite
NG2-426.6	18.6%	78.3%	-	2.3%	-	0.6%	Harzburgite
NG2-377.48	17.3%	79.3%	-	1.0%	-	2.3%	Harzburgite
NG2-208.4	17.6%	79.6%	1.0%	-	1.3%	0.3%	Harzburgite

occurs as oikocrysts with olivine and orthopyroxene chadacrysts. Orthopyroxenes occur as groundmass material as well as oikocrysts that enclose olivine chadacrysts. Opaque phases are chromite only and are fine-grained (≤0.05 mm).

NG2-604.5 is an olivine-orthopyroxenite, which exhibits orthocumulus to mesocumulus texture. Orthopyroxene and clinopyroxene occur as oikocrysts that enclose olivine chadacrysts. Interstitial phases include biotite and plagioclase. Chromite and chalcopyrite are observed as fine-grained (≤0.05 mm) opaque phases with a modal abundance of 0.3 mod.%.

NG2-524.8 is an olivine websterite with orthocumulus texture. Clinopyroxene constitutes ~30.3 mod.% whereas ~3.3 mod.% is orthopyroxene. Clinopyroxene grains occur almost exclusively as large oikocrysts enclosing olivine and orthopyroxene chadacrysts. Some orthopyroxenes make up part of the groundmass. This sample has undergone alteration (serpentinization), although the extent of alteration is slightly less than NG2-773.36 (Figure 4d). Biotite is present as both alteration and interstitial phases. Fine-grained (≤0.1 mm) chromite and pyrrhotite are observed as opaque phases in this sample, with an abundance of 1.6 mod.%.

NG2-450.53 is an orthopyroxenite that exhibits orthocumulus texture (Figure 4e). Orthopyroxene and clinopyroxene occur as oikocrysts enclosing olivine chadacrysts. Interstitial phases include plagioclase and biotite. Opaque phases (0.6 mod.%) include fine-grained (≤0.05 mm) chromite, pyrrhotite, and pentlandite.

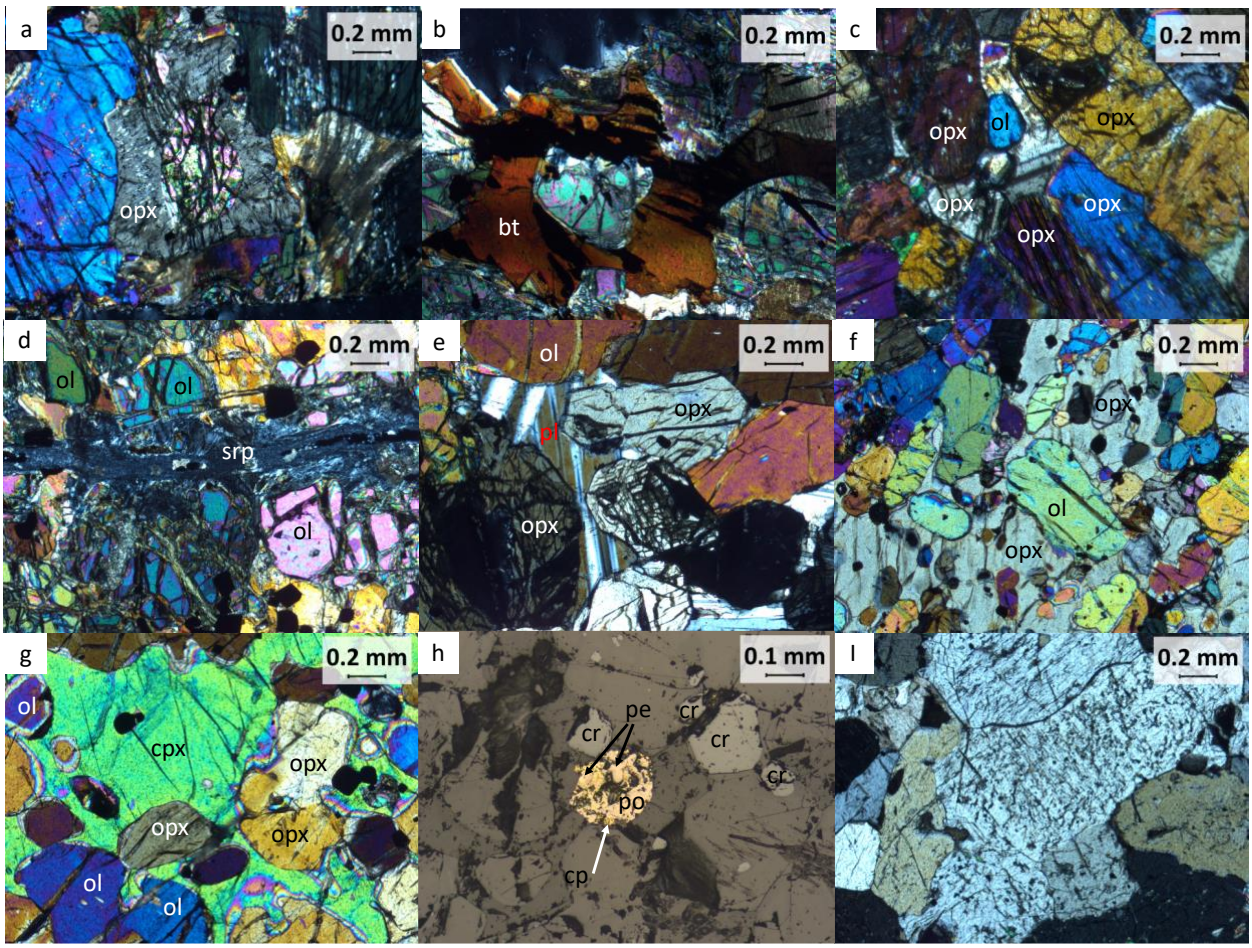

Figure 4. Photomicrographs of select samples exhibiting textures and minerals observed in the NG2 borehole suite. (a) Orthopyroxene (opx) adcumulus texture in sample NG2-208.4. (b) Orthopyroxene and olivine (ol) mesocumulus texture with intercumulus/interstitial plagioclase (pl) in sample NG2-633.0. (c) Orthopyroxene orthocumulus texture with intercumulus/interstitial plagioclase in sample NG2-450.53. (d) Poikilitic texture involving an opx oikocryst with ol and opx chadacrysts in sample NG2-377.48. (e) Poikilitic texture where clinopyroxene (cpx) is the oikocryst and opx and ol the chadacrysts in sample NG2-377.48. (f) Poikilitic texture with opx as the oikocryst enclosing a single ol chadacryst in sample NG2-772.36. (g) Poikilitic/interstitial biotite oikocryst with an olivine chadacryst in sample NG2-772.36. (h) Alteration/serpentinization of sample NG2-524.8 where a serpentine (srp) vein is cutting through and altering ol crystals. (i) Reflected light photomicrograph of sample NG2-377.48 showing the different opaque phases present in NG2 samples. In this image, chromite (cr), pyrrhotite (po), pentlandite (pe), and chalcopyrite (cp) are observed.

NG2-426.6 is a harzburgite with mesocumulus to adcumulus texture. Poikilitic texture is present with orthopyroxene and clinopyroxene oikocrysts enclosing olivine chadacrysts. Clinopyroxene is also present along with interstitial plagioclase and biotite. Furthermore, chromite, pyrrhotite, pentlandite, and chalcopyrite are the opaque phases, which have a cumulative abundance of 0.6 mod.%, and are fine-grained (≤0.2 mm).

NG2-377.48 is a harzburgite that contains mesocumulus to adcumulus texture. Further, clinopyroxene and orthopyroxene occur as oikocrysts enclosing olivine and orthopyroxene

chadacrysts (Figure 4f & 4g). Interstitial phases include plagioclase and biotite. Pyrrhotite, pentlandite, chalcopyrite, and chromite make up the fine-grained (≤0.25 mm) opaque phases, which have the greatest abundances for all NG2 samples (2.3 mod.%) (Figure 4h).

NG2-208.4 is a harzburgite with mesocumulus to adcumulus texture (Figure 4i). Orthopyroxene occurs both as oikocrysts and chadacrysts, as well as groundmass material. Olivine mostly occurs as chadacrysts. Interstitial material is comprised of biotite. Minor alteration has occurred in this sample, with serpentine and biotite making up the alteration phases. Fine-grained (≤0.25 mm) chromite and pyrrhotite make up the opaque phases (0.3 mod.%).

5.2 Major element concentrations

Thirteen samples from the NG2 borehole were analysed for major element concentrations (Table 2). Samples have SiO_2 and MgO contents that range from ~40-50 wt% and ~26-42 wt%, respectively. However, sample NG2-773.65 contains a lower MgO value (13.82 wt.%) than the rest of the sample suite, which is due to this being a chilled margin sample from below the Lower Zone. Additionally, FeO contents for the sample suite range from ~8 – 14 wt.%. The Al_2O_3 and CaO contents have a range of ~2 – 4 wt.% and ~1 – 3 wt.%, respectively. However, sample NG2-773.65 contains higher abundances of these major elements (Al_2O_3 = 11.19 wt.% and CaO = 7.55 wt.%). Further, NG2-773.65 contains elevated TiO_2 and Na_2O, and is depleted in Cr_2O_3 in respect to other NG2 samples (Table 2). Select major element data are plotted with respect to MgO in Figure 5. Major elements that have negative correlations with MgO include SiO_2, TiO_2, and CaO (Figures 5a, 5c, and 5d). Positive correlations with MgO include Fe_2O_3, Cr_2O_3, and NiO (Figures 5b, 5e, and 5f).

Magnesium numbers (Mg#) are reported for all samples. To calculate the Mg#, Fe_2O_3 wt.% is converted to FeO wt.% to get Fe in the 2^+ valence state. To do so, Fe_2O_3 wt.% is multiplied by 0.9. Next, both MgO wt.% and FeO wt.% need to be divided by the O wt.% values, which are 40.3 and 71.8, respectively. Following this step, Mg# is calculated using equation 1:

$$Mg\# = Mg^{2+}/(Mg^{2+} + Fe^{2+}) \qquad \text{eq. 1}$$

Table 2. Major and trace element concentrations for NG2 samples with rock types listed. *Rock types taken from modal abundances of thin sections from this study. All other sample rock types are from the NG2 borehole log by B. Teigler, W. J. de Klerk, R. N. Scoon, S. A. Haikney, and W. D. Maier.

	NG2-773.65	NG2-734.64	NG2-706.53	NG2-689.73	NG2-604.5	NG2-591.5	NG2-553.0	NG2-524.8	NG2-450.53	NG2-426.6	NG2-377.48	NG2-219.9	NG2-197.0
SiO_2 (wt. %)	52.3	41.3	40.8	54.5	54.1	41.6	48.6	38.2	52.7	51.2	52.7	54.7	53.2
TiO_2	0.546	0.0471	0.106	0.187	0.159	0.0967	0.117	0.132	0.145	0.127	0.126	0.118	0.0987
Al_2O_3	11.2	2.04	3.12	4.28	3.55	2.72	2.94	2.86	3.45	3.64	3.28	3.55	2.21
Fe_2O_3	10.5	12.7	10.7	8.78	9.66	13.5	12.1	13.2	9.98	10.5	10.8	9.67	9.92
MnO	0.167	0.161	0.144	0.166	0.473	0.174	0.184	0.167	0.178	0.171	0.190	0.190	0.174
MgO	13.8	41.5	36.2	26.4	27.2	35.9	31.9	35.7	29.0	29.8	28.6	27.8	31.0
CaO	7.55	0.674	1.91	3.01	2.65	1.56	1.93	1.64	2.52	2.60	2.22	2.44	1.77
Na_2O	1.77	0.358	0.477	0.825	0.556	0.385	0.413	0.328	0.422	0.450	0.378	0.525	0.218
K_2O	0.612	0.230	0.152	0.388	0.186	0.123	0.110	0.471	0.115	0.105	0.0643	0.111	0.0377
P_2O_5	0.0841	0.0400	0.0346	0.0467	0.0202	0.0286	0.0142	0.0165	0.0242	0.0102	0.0153	0.0102	0.00305
SO_3	0.0152	0.00717	0.0163	0.0142	0.0121	0.0187	0.0162	0.136	0.0171	0.0163	0.00715	b.d.	b.d.
Cr_2O_3	0.163	0.575	0.769	0.408	0.433	0.684	0.476	1.09	0.509	0.701	1.08	0.478	0.552
NiO	0.0486	0.268	0.368	0.157	0.0857	0.223	0.146	0.262	0.0977	0.114	0.101	0.0939	0.116
H_2O-	0.265	0.0740	0.212	0.219	0.117	0.111	0.0810	0.131	0.0655	0.0460	0.0545	0.0549	0.0490
LOI	0.460	-0.477	4.70	0.320	0.0725	2.24	0.489	5.01	0.175	0.0455	-0.105	-0.0405	0.216
Sum	99.4	99.5	99.7	99.7	99.3	99.4	99.5	99.4	99.3	99.5	99.5	99.7	99.6
Mg#	72.4	86.6	87.1	85.6	84.8	84.1	83.9	84.3	85.2	84.9	84.0	85.1	86.1
Li (ppm)	28.8	2.92	4.93	7.42	4.57	2.95	2.79	-	2.44	-	1.48	4.18	2.85
B	4.84	9.23	2.21	1.91	1.24	1.90	0.868	-	1.32	-	0.610	0.434	0.0146
Sc	18.2	3.84	3.29	4.61	4.06	0.657	1.69	-	1.27	-	2.15	3.53	3.76
Ti	3840	292	637	1090	897	532	622	-	810	-	681	644	539
V	162	30.9	58.6	87.5	88.2	56.7	64.3	-	69.1	-	92.6	77.7	99.4
Cr	1130	3700	5100	2620	2730	4210	2880	-	3060	-	6420	2840	3140
Co	67.9	153	124	68.7	77.4	134	113	-	84.4	-	86.8	80.4	96.8
Ni	390	2070	1680	577	583	1590	1020	-	659	-	692	660	801
Cu	40.5	10.8	15.9	24.3	23.1	14.5	32.4	-	17.8	-	15.8	11.5	9.04
Zn	72.0	64.1	56.5	54.0	53.4	67.3	62.1	-	53.8	-	63.7	54.0	51.0
Ga	10.8	2.00	3.35	4.07	3.68	3.05	2.81	-	3.32	-	3.75	3.46	2.77
Ge	1.26	1.18	0.942	1.00	1.04	1.03	1.05	-	0.970	-	1.01	0.964	0.961
Se	0.329	0.0352	-0.556	-0.673	-0.760	-0.963	-0.960	-	-0.955	-	-1.07	-1.09	-1.19
Rb	21.0	7.41	4.82	12.4	5.84	3.55	2.26	-	2.71	-	0.933	1.80	0.638
Sr	227	34.3	58.6	76.8	201	47.7	44.5	-	51.8	-	45.8	51.3	17.0
Y	10.9	1.63	3.29	4.61	3.34	2.48	2.25	-	3.15	-	2.65	2.83	2.08
Zr	24.2	52.2	29.9	34.5	10.6	10.8	13.9	-	10.7	-	9.10	7.53	4.90
Nb	3.52	1.13	0.763	1.14	0.583	0.621	0.332	-	0.450	-	0.183	0.258	0.105
Mo	-0.00179	0.128	-0.000541	0.0582	-0.0228	0.00972	-0.0730	-	-0.0519	-	-0.0733	-0.0881	-0.0970
Sn	0.604	0.226	0.224	0.508	0.181	0.160	0.0980	-	1.99	-	2.83	0.0864	0.0967
Te	0.0179	0.00381	0.00222	0.00208	0.00390	-0.00494	0.00826	-	-0.00430	-	-0.000594	-0.00514	-0.00584
Cs	1.61	0.679	0.426	0.766	0.241	0.265	0.156	-	0.168	-	0.0547	0.0790	0.189
Ba	186	57.1	49.6	108	66.0	44.9	38.6	-	43.3	-	31.3	36.0	10.6
La	9.32	3.65	3.42	4.74	2.70	2.86	1.88	-	2.25	-	2.05	1.82	0.530
Ce	20.2	6.31	7.13	9.65	5.56	5.73	3.76	-	4.58	-	4.06	3.50	1.08
Pr	2.54	0.644	0.854	1.14	0.681	0.682	0.447	-	0.550	-	0.480	0.409	0.138
Nd	10.3	2.14	3.36	4.42	2.72	2.65	1.78	-	2.20	-	1.90	1.61	0.621
Sm	2.21	0.339	0.690	0.899	0.574	0.518	0.383	-	0.491	-	0.415	0.357	0.177
Eu	0.636	0.124	0.203	0.278	0.186	0.162	0.144	-	0.181	-	0.147	0.136	0.0676
Gd	2.19	0.355	0.698	0.949	0.624	0.542	0.414	-	0.556	-	0.459	0.404	0.233
Tb	0.326	0.0459	0.105	0.142	0.0966	0.0806	0.0669	-	0.0905	-	0.0712	0.0699	0.0468
Dy	1.93	0.260	0.619	0.861	0.614	0.473	0.422	-	0.587	-	0.478	0.486	0.343
Ho	0.391	0.0583	0.130	0.181	0.135	0.100	0.0898	-	0.127	-	0.106	0.112	0.0836
Er	1.07	0.174	0.359	0.513	0.393	0.284	0.263	-	0.370	-	0.315	0.359	0.260
Tm	0.157	0.0280	0.0538	0.0779	0.0618	0.0441	0.0418	-	0.0584	-	0.0515	0.0592	0.0434
Yb	0.988	0.208	0.350	0.524	0.430	0.288	0.289	-	0.396	-	0.366	0.415	0.331
Lu	0.140	0.0326	0.0532	0.0804	0.0656	0.0453	0.0459	-	0.0623	-	0.0571	0.0681	0.0525
Hf	0.717	1.15	0.736	0.971	0.351	0.305	0.367	-	0.318	-	0.268	0.240	0.163
Ta	0.235	0.104	0.0549	0.0802	0.0395	0.0394	0.0235	-	0.0349	-	0.0138	0.0191	0.00734
W	0.342	0.299	0.136	0.197	0.0907	0.141	0.0622	-	0.0711	-	0.0473	0.0591	0.0236
Ir	0.0000107	0.0000182	0.0000132	0.0000151	0.00000499	0.00000484	0.00000569	-	0.0000101	-	0.0000103	0.00000384	0.00000653
Au	0.00066	0.00145	0.00209	0.00207	0.00227	0.00182	0.00263	-	0.00264	-	0.00277	0.00271	0.00197
Hg	0.00296	0.00317	0.000867	0.00136	0.000612	0.00124	0.000294	-	0.0000968	-	0.000489	-0.000290	-0.0000449
Tl	0.153	0.0612	0.0457	0.0896	0.0977	0.0333	0.0633	-	0.0238	-	0.00824	0.0223	0.00745
Pb	7.71	2.23	1.70	2.06	1.17	1.36	1.00	-	1.08	-	0.844	0.984	0.357
Th	1.54	1.40	0.802	0.878	0.533	0.616	0.287	-	0.343	-	0.280	0.236	0.0657
U	0.437	0.553	0.210	0.271	0.144	0.201	0.0915	-	0.100	-	0.0816	0.0622	0.0191
Rock Type	Hornfels	Harzburgite/Dunite	Dunite	Dunite	Pyroxenite*	Dunite	Harzburgite	Websterite*	Pyroxenite*	Harzburgite*	Harzburgite*	Harzburgite	Harzburgite

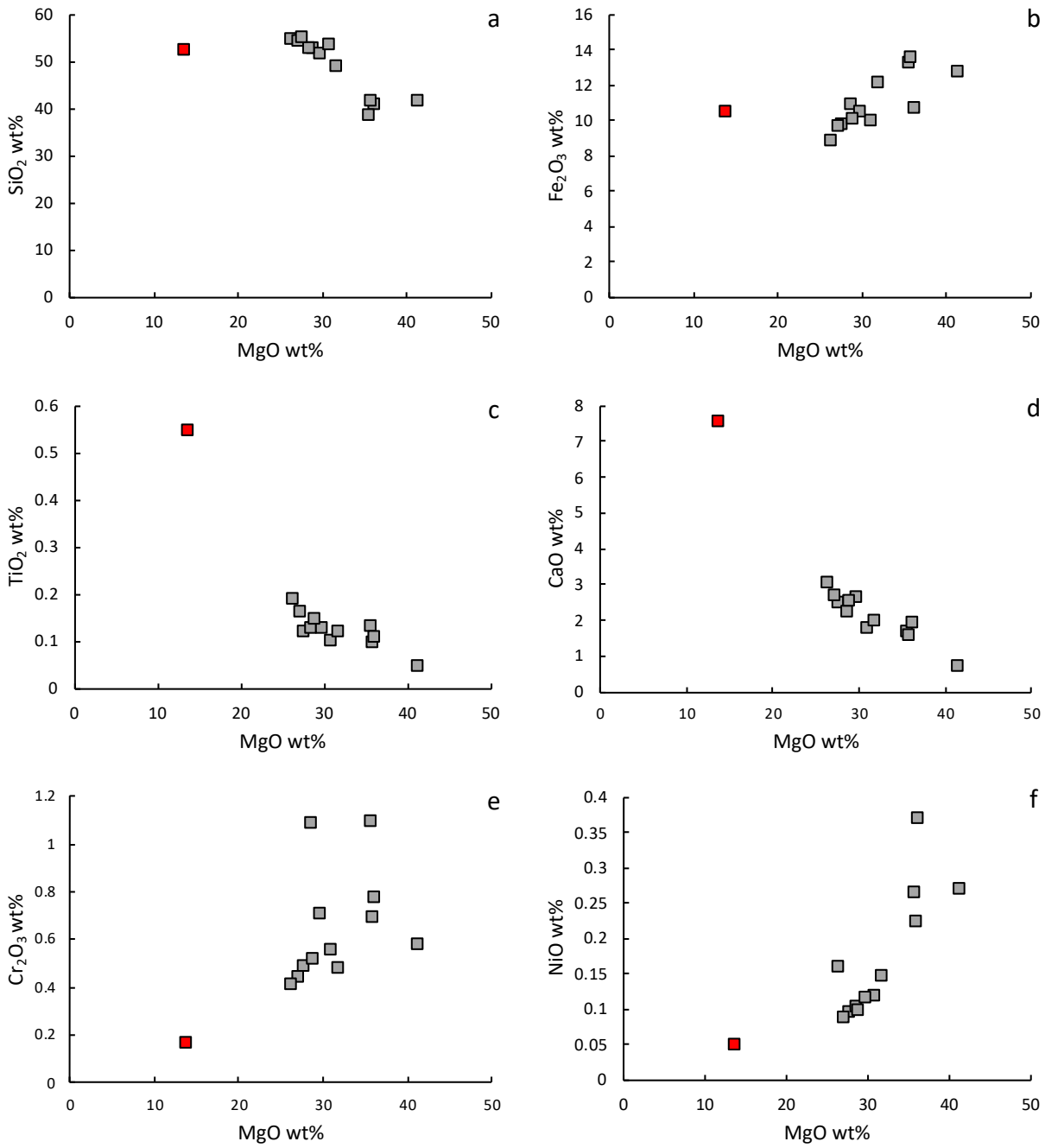

Figure 5. Major element compositions for NG2 samples relative to MgO. (a) SiO_2 showing a decreasing trend with increasing MgO contents. (b) Fe_2O_3 with a positive trend with increasing MgO contents. (c) TiO_2 with a decreasing trend with increasing MgO. (d) CaO with a decreasing trend toward increasing MgO contents. (e) Cr_2O_3 showing a general increasing trend with MgO contents. When Cr_2O_3 contents reach about 0.6 wt% the trend disappears and the data are scattered. (f) NiO showing an increasing trend as MgO contents increase. Data points in red are for NG2-772.36, which is a chilled margin sample from the base of the NG2 borehole. Red squares with black outlines are chilled margin sample NG2-773.65.

The Mg#'s for the NG2 samples range from 0.72 to 0.87, with the majority of samples falling between 0.83 to 0.87 (Table 2). Sample NG2-773.65 falls out of the normal range of Mg# values,

with an Mg# = 0.72.

5.3 Trace element concentrations

Trace element concentrations are reported for the NG2 samples (Table 2). The NG2 samples show enrichment in the large ion lithophile elements (LILE) with respect to the high field strength elements (HFSE) (Figure 6). Further, in primitive mantle normalised Figure 6, Pb shows a strong positive anomaly, and Ta and Nb show strong negative anomalies. All samples show very similar trends in trace element concentrations, including NG2-773.65, which has much different major element concentrations. In regard to rare earth elements (REE), samples are enriched in light rare earth elements (LREE) with respect to heavy rare earth elements (HREE) (Figure 7).

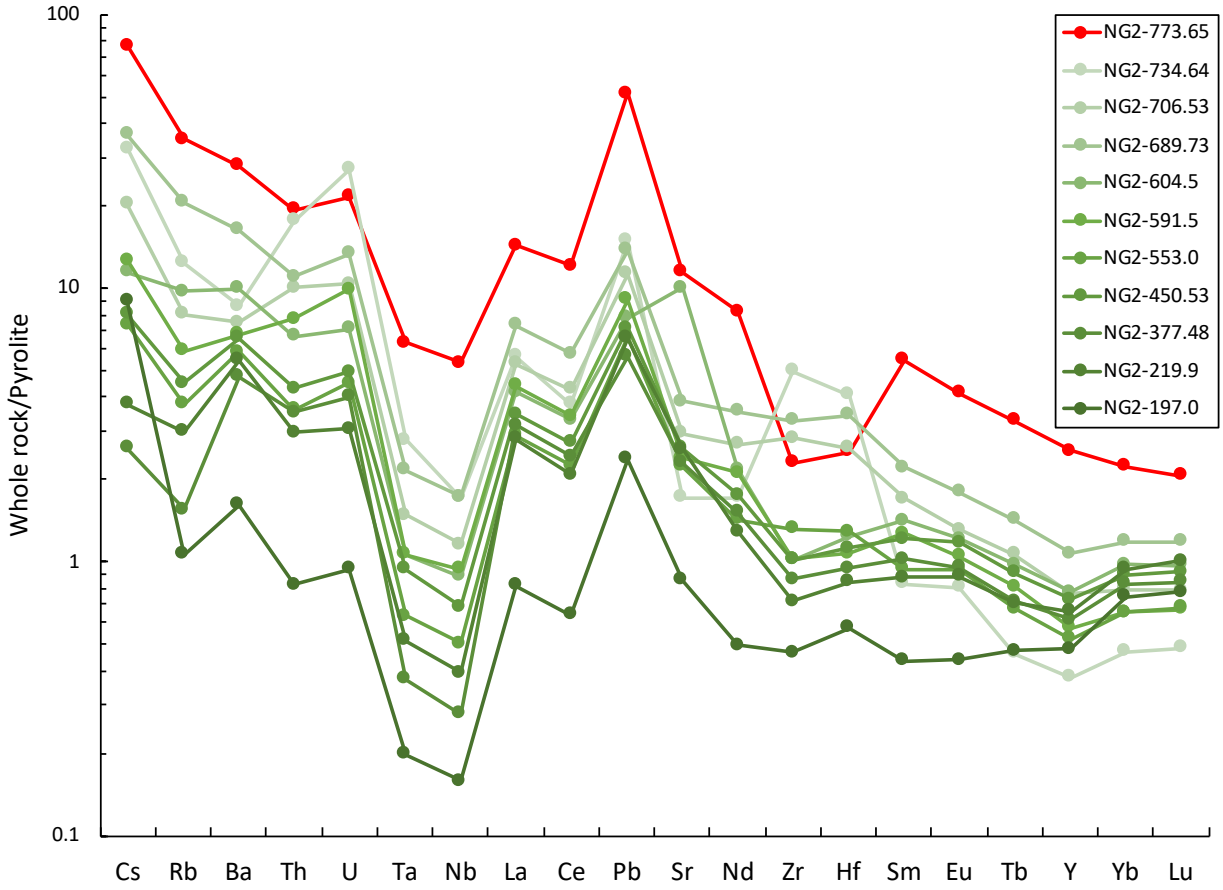

Figure 6. Trace element concentrations for NG2 Bushveld samples normalized to pyrolite values from McDonough and Sun, 1995.

Sample NG2-197 shows uncharacteristically low LREE and is slightly more enriched in HREE. Further, NG2-734.64 remains enriched in the LREE relative to the HREE, but the trend exhibited

does not match other NG2 samples. Sample NG2-734.64 has a La concentration of 3.65 ppm, and the average La concentration for NG2 samples is 2.59, excluding NG2-773.65 which has a much higher concentration (9.32 ppm). However, NG2-734.64 exhibits a sharper decrease from LREE to Dy, in which the trend becomes flat until a slight relative enrichment in Yb and Lu compared to the MREE and HREE (Figure 7). The primitive mantle-normalized (value of pyrolite used from McDonough and Sun, 1995) La/Yb ratios [$(La/Yb)_N$] for NG2-734.64 are much higher (11.9) than

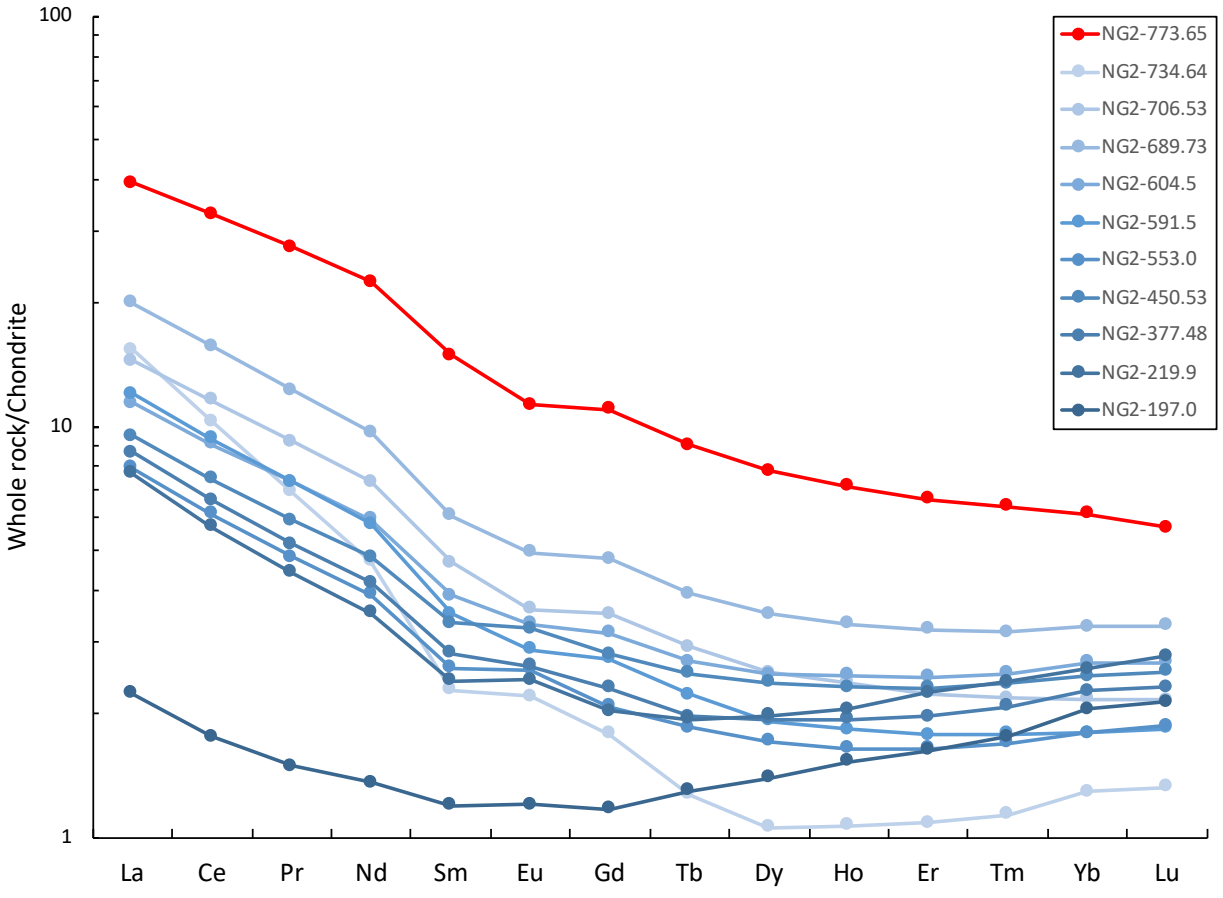

Figure 7. Rare earth element (REE) concentrations, normalized to chondrite (McDonough and Sun, 1995) for NG2 samples.

the other NG2 samples which have $(La/Yb)_N$ values ranging from $(La/Yb)_N$ = 1.09 to 6.74. Additionally, the samples show variable Zr/Hf ratios, with three samples (NG2-734.64, -706.53, and -553.0) exhibiting positive Zr-Hf anomalies, and the remainder negative Zr-Hf anomalies. Scatter plots of La/Sm vs Gd/Yb, La/Sm vs La/Yb, and La/Yb vs Gd/Yb can be seen in Figure 8. In

Figure 8a there is no relationship between La/Sm and Gd/Yb, and Figure 8b exhibits a slight positive correlation, although most samples are grouped between La/Sm = 4 – 6. Further, Figure 8c shows a positive trend for La/Yb vs Gd/Yb. There is one outlier, chilled margin sample NG2-734.64, in all of these scatter plots. This sample has higher La/Sm and La/Yb ratios than the other NG2 samples while maintaining similar Gd/Yb ratios. This is a result of NG2-734.64 being relatively enriched in La but depleted Sm and Yb in comparison to the other NG2 samples.

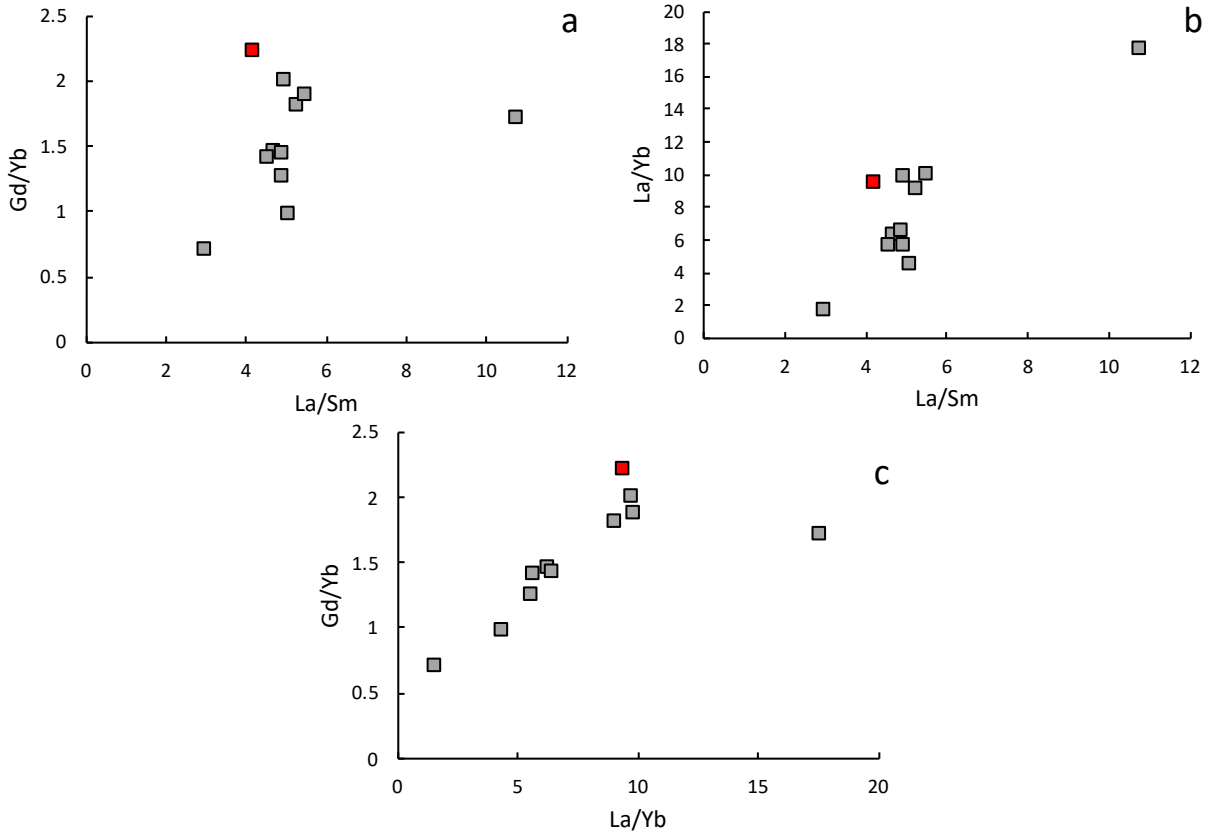

Figure 8. Scatter plot diagrams illustrating the relationships between La/Sm, Gd/Yb, and La/Yb ratios. (a) La/Sm vs Gd/Yb, (b) La/Sm vs La/Yb, and (c) La/Yb vs Gd/Yb. Red squares with black outlines are chilled margin sample NG2-773.65.

5.4 Oxygen isotopes

Oxygen isotope values for NG2 samples have a range of $\delta^{18}O$ = 5.56 – 9.78 ‰ (Table 3). Within these values, olivine separates contain a range of $\delta^{18}O$ = 5.56 – 6.89‰, and the orthopyroxene separates $\delta^{18}O$ = 5.79 – 9.78, although most orthopyroxene $\delta^{18}O$ values fall between 6.18 – 6.49. Olivine and orthopyroxene overlap, however, the orthopyroxene samples

have consistently higher $\delta^{18}O$ values. Chilled margin sample NG2-773.65 contains orthopyroxene $\delta^{18}O$ = 9.80‰, 9.42‰, and 6.49‰ (Table 3). The two elevated values are much higher than any other samples from the NG2 suite, similarly to the differences this sample has in terms of major elements compared to the other samples. One analysis for NG2-773.65 resulted in a $\delta^{18}O$ = 6.49, which is much lower than the two other analyses for this sample, but this value is most similar to the NG2 sample suite. This value ($\delta^{18}O$ = 6.49) for sample NG2-773.65 is disregarded since the other two $\delta^{18}O$ values for this sample are very similar. All samples with both olivine and orthopyroxene separate analyses, with the exception of samples NG2-689.73 and NG2-377.48,

Table 3. Oxygen isotope data for the NG2 borehole. All values are in per mill (‰).

	$\delta^{18}O$ olivine	$\delta^{18}O$ orthopyroxene	$\delta^{18}O$ orthopyroxene - 2	$\delta^{18}O$ orthopyroxene - 3	$\delta^{18}O$ clinopyroxene
NG2-773.65	-	9.78	9.42	6.49	-
NG2-734.64	5.67	-	-	-	-
NG2-706.5	5.56	6.32	-	-	-
NG2-689.73	6.89	6.48	-	-	-
NG2-604.5	6.28	6.48	-	-	-
NG2-591.5	6.06	6.27	-	-	-
NG2-553.0	-	6.49	-	-	-
NG2-524.8	5.67	-	-	-	-
NG2-450.53	6.67	-	-	-	6.02
NG2-426.6	-	6.24	-	-	-
NG2-377.48	6.56	5.79	-	-	-
NG2-219.9	-	6.18	-	-	-
NG2-197.0	-	8.03	6.32	-	-

had higher $\delta^{18}O$ values (0.41‰ and 0.77‰ higher, respectively) for orthopyroxene separates than olivine. Only one clinopyroxene sample was run (NG2-450.53), and has $\delta^{18}O$ = 6.02, similar to both olivine and orthopyroxene separates for other samples. Further, sample NG2-450.53 has $\delta^{18}O$ = 6.56 for orthopyroxene, which is higher than the clinopyroxene $\delta^{18}O$ value for this sample. Reasoning for differences in $\delta^{18}O$ values between olivine, orthopyroxene, and clinopyroxene separates will be covered in detail within the discussion section. Sample NG2-197.0 has orthopyroxene $\delta^{18}O$ values of 8.03‰ and 6.32‰, which vary greatly (Table 3). It is possible that some alteration material was present on mineral separates to cause the higher of the two values, since this value deviates from those of the NG2 sample suite other than the chilled margin

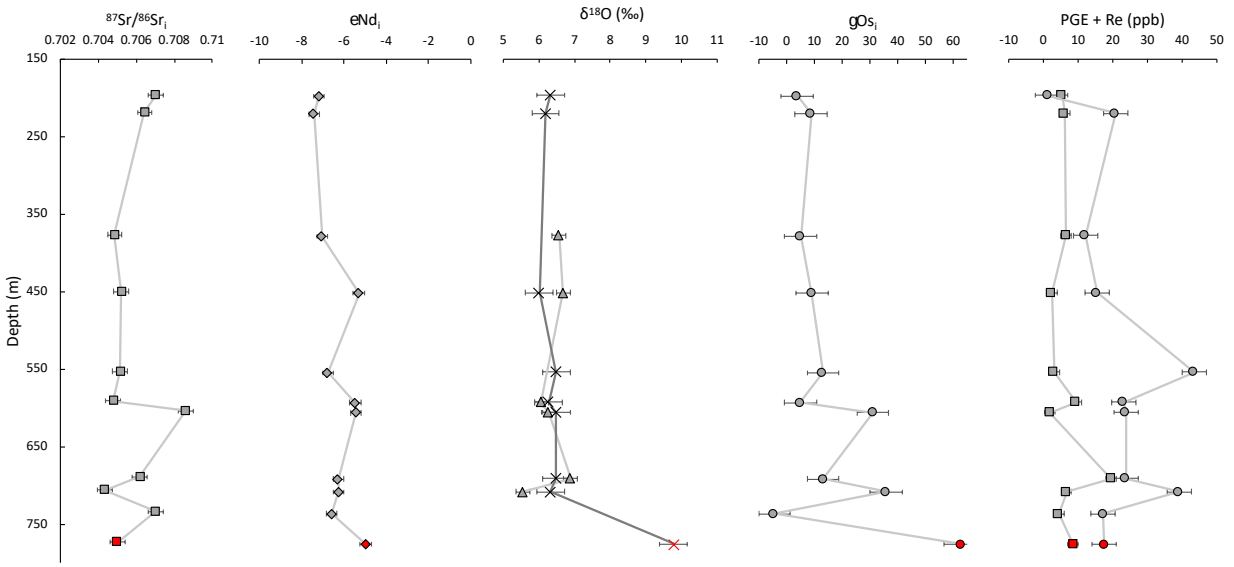

Figure 9. Isotope ($^{87}Sr/^{86}Sr_i$, εNd_i, $\delta^{18}O$, γOs_i) and PGE + Re compositions for NG2 samples with depth, including standard error bars. Initial Sr ($^{87}Sr/^{86}Sr_i$) shows variable composition between depths of 800 and 600m. Samples from more shallow locations within the borehole have more consistent values. εNd_i shows a general decreasing trend with increasing height from the base of the borehole section. Shown in the $\delta^{18}O$ plot are olivine (triangles) and orthopyroxene and clinopyroxene (x's) $\delta^{18}O$ values. The $\delta^{18}O$ values are consistent throughout the section with the exception of sample NG2-773.65 (red symbols), which has more elevated $\delta^{18}O$ than the other samples. The γOs_i values display variable yet decreasing contents with increasing height from the base of the borehole. The PGE + Re plot shows the sum of the IPGE (Os, Ir, Ru) [squares] and the PPGE (Pt and Pd) + Re [circles]. Here there is a generally consistent trend with some samples that have more elevated or depleted contents in the borehole stratigraphy.

sample, NG2-773.65. The $\delta^{18}O$ values for NG2 samples remain constant throughout the borehole sequence (Figure 9). Further, $\delta^{18}O$ values do not correlate with values from the other isotopic systems utilised in this study (Figure 10a, 10b, 10f). This suggests that the stable isotope, $\delta^{18}O$, is consistent with the values given by the radiogenic isotopic systems utilised (i.e., $^{87}Sr/^{86}Sr$, $^{143}Nd/^{144}Nd$, and Os-Os).

5.5 Samarium-neodymium isotopes

The Bushveld NG2 borehole samples have measured $^{143}Nd/^{144}Nd$ isotope values that range from 0.5109 to 0.5119. To age-correct the samples and obtain εNd_i values, the first calculation is to obtain the $^{147}Sm/^{144}Nd$ value. Trace element compositions for samples are reported as ^{147}Sm and ^{146}Nd. To obtain the necessary $^{147}Sm/^{144}Nd$ ratio, $^{147}Sm/^{146}Nd$ ratios and measured $^{143}Nd/^{144}Nd$ isotopic values are utilised and applied to the following equation:

$$^{147}Sm/^{144}Nd = {}^{147}Sm/^{146}Nd\ [0.53151 + (0.14252 \times {}^{143}Nd/^{144}Nd)] \qquad \text{eq. 2}$$

The $^{147}Sm/^{144}Nd$ values range from 0.0954 to 0.1725, with most samples falling between $^{147}Sm/^{144}Nd$ = 0.1182 – 0.1349 (Table 4). Outliers for $^{147}Sm/^{144}Nd$ values include NG2-734.64

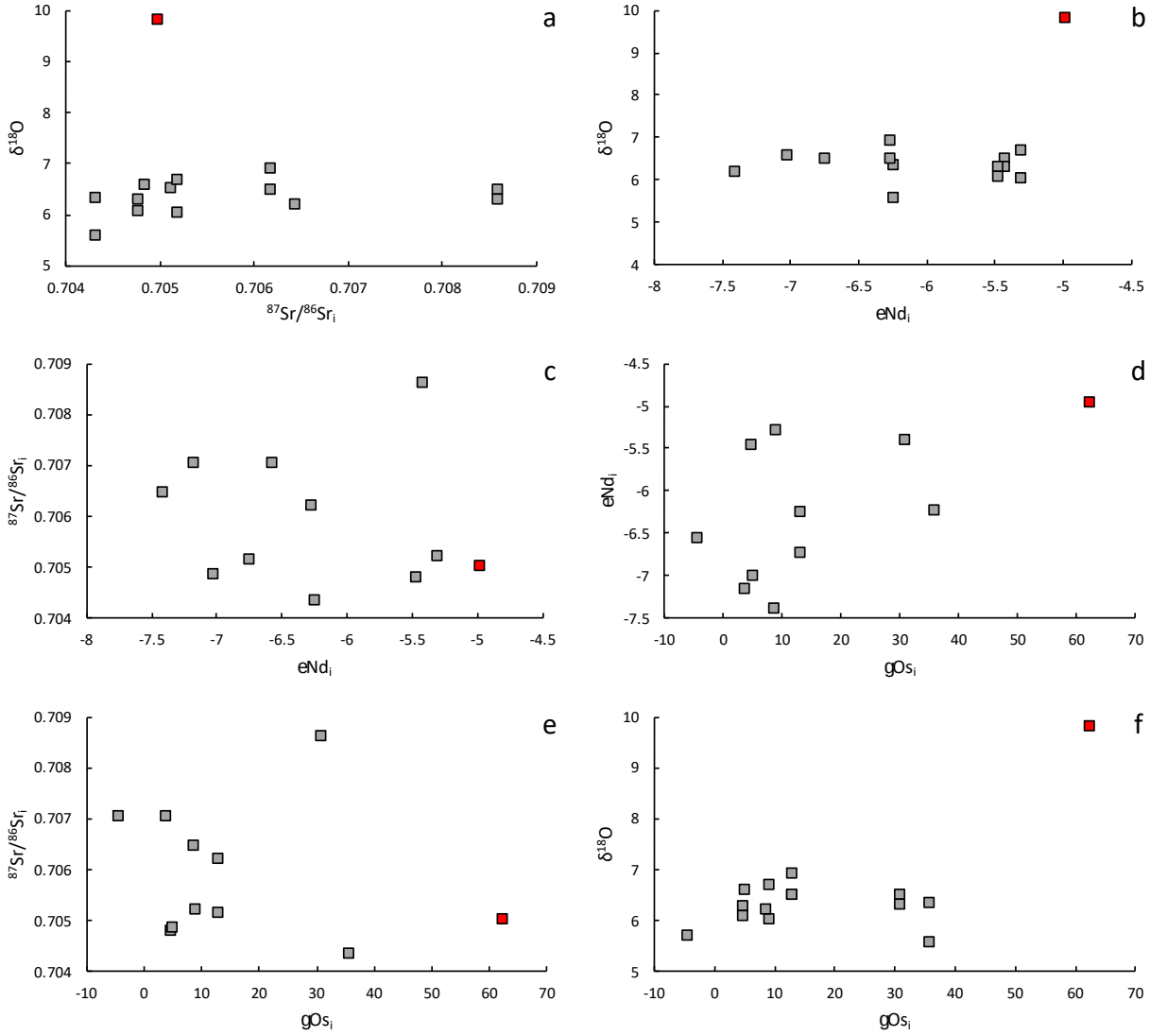

Figure 10. Scatter plots comparing data points from isotope systems utilised in this study. (a) $^{87}Sr/^{86}Sr_i$ vs $\delta^{18}O$, (b) εNd_i vs $\delta^{18}O$, (c) εNd_i vs $^{87}Sr/^{86}Sr_i$, (d) γOs_i vs εNd_i, (e) γOs_i vs $^{87}Sr/^{86}Sr_i$, and (f) γOs_i vs $\delta^{18}O$. The red square with the black outline represents sample NG2-773.65, the chilled margin sample.

(0.0954) and NG2-197.0 (0.1725) (Table 4). The next step in the calculation is to determine the chondritic uniform reservoir (CHUR) for the age of the samples analysed. For Bushveld NG2

borehole calculations, a reference age, t, of 2.06 Ga is utilized (Buick et al., 2001). The equation for this calculation is below:

$$^{143}Nd/^{144}Nd_{CHUR\ (i)} = {}^{143}Nd/^{144}Nd_{CHUR} - {}^{147}Sm/^{144}Nd_{CHUR}\ (e^{\lambda(t)} - 1) \qquad \text{eq. 3}$$

Where $^{143}Nd/^{144}Nd_{CHUR\ (i)}$ is the initial isotopic composition for the CHUR, $^{143}Nd/^{144}Nd_{CHUR}$ and $^{147}Sm/^{144}Nd_{CHUR}$ are the present-day CHUR isotopic compositions for $^{143}Nd/^{144}Nd$ and $^{147}Sm/^{144}Nd$, respectively, λ is the decay constant for the Sm-Nd system (6.54×10^{-12}), and t is the age of the samples analysed. Next, the sample initial $^{143}Nd/^{144}Nd$ ($^{143}Nd/^{144}Nd_{sample\ (i)}$) isotopic composition is calculated:

$$^{143}Nd/^{144}Nd_{sample\ (i)} = {}^{143}Nd/^{144}Nd_{sample} - {}^{147}Sm/^{144}Nd_{sample}\ (e^{\lambda(t)} - 1) \qquad \text{eq. 4}$$

Where $^{143}Nd/^{144}Nd_{sample}$ is the isotopically measured $^{143}Nd/^{144}Nd$ ratio for samples and $^{147}Sm/^{144}Nd_{sample}$ is the ratio given by equation 2. Values for the $^{143}Nd/^{144}Nd$ ratio can be found in Table 4. The final calculation is to obtain the εNd_i value:

$$\varepsilon Nd_i = (^{143}Nd/^{144}Nd_{sample\ (i)} - {}^{143}Nd/^{144}Nd_{CHUR\ (i)})/(\ ^{143}Nd/^{144}Nd_{CHUR\ (i)}) \times 10{,}000 \qquad \text{eq. 5}$$

The NG2 borehole samples contain εNd_i values in the range of -4.97 to -7.40, where the Marginal Zone sample NG2-773.65 contains the highest value (-4.97) (Table 4). Samples do not show a trend of decreasing εNd_i values with increasing stratigraphic height within the NG2 borehole sequence, as the values vary significantly throughout (Figure 9). Values for εNd_i do not show clear relationships with $^{87}Sr/^{86}Sr_i$, $\delta^{18}O$, or γOs_i (Figure 10b - 10d)

5.6 Rubidium-strontium isotopes

Rubidium-strontium isotope values for NG2 samples have a measured isotopic $^{87}Sr/^{86}Sr_i$ range of 0.7066 – 0.7256 (Table 4). In order to obtain Sr-isotope values in a form that can be compared to other data that are not from the Bushveld, the initial Sr compositions ($^{87}Sr/^{86}Sr_i$)

need to be calculated. The first step to obtain $^{87}Sr/^{86}Sr_i$ values is to calculate the $^{87}Rb/^{86}Sr$ ratio since trace element data report Rb and Sr as ^{85}Rb and ^{88}Sr:

$$^{87}Rb/^{86}Sr_{sample} = {}^{85}Rb/^{88}Sr_{sample}\,[2.6939 + 0.2832\,(^{87}Sr/^{86}Sr)] \qquad \text{eq. 6}$$

where $^{87}Rb/^{88}Sr_{sample}$ is the sample calculated ratio of ^{87}Rb and ^{86}Sr, $^{85}Rb/^{88}Sr_{sample}$ is the ratio of ^{85}Rb and ^{88}Sr from sample trace element data, and $^{87}Sr/^{86}Sr$ is the measured isotope composition of the sample. Ratio compositions for $^{87}Rb/^{86}Sr$ range from 0.0590 – 0.6263 (Table 4). To calculate $^{87}Sr/^{86}Sr_i$ equation 7 is employed:

$$^{87}Sr/^{86}Sr_{initial} = {}^{87}Sr/^{86}Sr - {}^{87}Rb/^{86}Sr_{sample}\,(e^{\lambda(t)} - 1) \qquad \text{eq. 7}$$

where $^{87}Sr/^{86}Sr$ is the measured isotopic composition of the sample, $^{87}Rb/^{86}Sr_{sample}$ is the ratio of $^{87}Rb/^{86}Sr$ given by trace element analyses, λ is the decay constant for the system (1.42×10^{-11}), and t is the age of the sample.

Table 4. Rb, Sr, Sm, and Nd trace element concentrations, measured Sr and Nd isotope values, initial Sr ($^{87}Sr/^{86}Sr_i$), and εNd_i values. See text for $^{87}Sr/^{86}Sr_i$ and εNd_i calculation equations.

	Rb (ppm)	Sr (ppm)	$^{87}Rb/^{86}Sr$	$^{87}Sr/^{86}Sr$	2SE	Sr_i	Sm (ppm)	Nd (ppm)	$^{147}Sm/^{144}Nd$	$^{143}Nd/^{144}Nd$	2SE	εNd
NG2-773.65	21.02	227.28	0.2678	0.7129	0.000010	0.7050	2.21	10.32	0.1295	0.5115	0.000013	-4.97
NG2-734.64	7.41	34.32	0.6263	0.7256	0.000017	0.7070	0.34	2.14	0.0954	0.5109	0.000018	-6.56
NG2-706.53	4.82	58.56	0.2382	0.7114	0.000014	0.7043	0.69	3.36	0.1242	0.5113	0.000012	-6.24
NG2-689.73	12.37	76.75	0.4669	0.7200	0.000013	0.7062	0.90	4.42	0.1228	0.5113	0.000012	-6.26
NG2-604.5	5.84	200.69	0.0843	0.7111	0.000013	0.7086	0.57	2.72	0.1275	0.5114	0.000012	-5.41
NG2-591.5	3.55	47.72	0.2152	0.7112	0.000016	0.7048	0.52	2.65	0.1182	0.5113	0.000011	-5.47
NG2-553.0	2.26	44.45	0.1471	0.7095	0.000014	0.7051	0.38	1.78	0.1300	0.5114	0.000019	-6.75
NG2-450.53	2.71	51.79	0.1513	0.7097	0.000013	0.7052	0.49	2.20	0.1349	0.5115	0.000012	-5.30
NG2-377.48	0.93	45.79	0.0590	0.7066	0.000014	0.7049	0.42	1.90	0.1318	0.5114	0.000012	-7.02
NG2-219.9	1.80	51.29	0.1016	0.7095	0.000012	0.7064	0.36	1.61	0.1338	0.5114	0.000014	-7.40
NG2-197.0	0.64	17.04	0.1084	0.7102	0.000014	0.7070	0.18	0.62	0.1725	0.5119	0.000028	-7.17

The $^{87}Sr/^{86}Sr_i$ values range from 0.7043 – 0.7086 (Table 4), and samples from deeper in the NG2 borehole contain more variable $^{87}Sr/^{86}Sr_i$ values than samples from shallower depths in the borehole sequence (Figure 9). Additionally, $^{87}Sr/^{86}Sr_i$ does not show relationships with $\delta^{18}O$, εNd_i, or γOs_i (Figures 10a, 10c, and 10e).

997 **5.7 Rhenium-osmium isotopes**

998 The $^{187}Os/^{188}Os$ isotope values for NG2 samples range from 0.1257 to 0.4450 (Table 5).
999 Additionally, samples have a range of $^{187}Re/^{188}Os_{sample}$ that fall between 0.1936 to 7.4844 (Table
1000 5). NG2 samples are then age-corrected ($^{187}Os/^{188}Os_{sample\ (i)}$) to 2.06 Ga using equation 8:
1001
1002 $$^{187}Os/^{188}Os_{sample\ (i)} = {}^{187}Os/^{188}Os_{sample} - {}^{187}Re/^{188}Os_{sample}\,(e^{\lambda(t)} - 1) \qquad \text{eq. 8}$$
1003
1004 where $^{187}Os/^{188}Os_{sample}$ and $^{187}Re/^{188}Os_{sample}$ are the measured $^{187}Os/^{188}Os$ and $^{187}Re/^{188}Os$ values
1005 for each sample, λ is the ^{187}Re decay constant ($\lambda = 1.666 * 10^{-11}$), and t is the time for the age
1006 correction (Shirey and Walker, 1998). The $^{187}Os/^{188}Os_{sample\ (i)}$ values range from 0.1081 to 0.1837,
1007 but are generally in the range of $^{187}Os/^{188}Os_{sample\ (i)}$ = 0.1174 – 0.1279 (Table 5). Samples that
1008 deviate from the typical $^{187}Os/^{188}Os_{sample\ (i)}$ range include NG2-773.65 (0.1836), NG2-706.53
1009 (0.1536), and NG2-604.5 (0.1482) (Table 5). The $^{187}Os/^{188}Os_{sample\ (i)}$ values are useful when
1010 comparing rocks that are temporally and spatially related, however, in order to get these values
1011 in a form that can be compared to rocks that have no relationship they need to be reported as a
1012 percentage difference between the $^{187}Os/^{188}Os_{sample\ (i)}$ and the chondritic composition at the age-
1013 corrected time of $^{187}Os/^{188}Os_{sample\ (i)}$, γOs_i (Shirey and Walker, 1998; Day, 2013). The first step in
1014 calculating γOs_i is to determine the age-corrected chondrite value:
1015
1016 $$^{187}Os/^{188}Os_{chon(t)} = {}^{187}Os/^{188}Os_{chon(i)} + {}^{187}Re/^{188}Os_{chon}\,(e^{\lambda(4568000000)} - e^{\lambda(t)}) \qquad \text{eq. 9}$$
1017
1018 Where $^{187}Os/^{188}Os_{chon(t)}$ is the age-corrected chondritic value, $^{187}Os/^{188}Os_{chon(i)}$ is the initial
1019 chondritic $^{187}Os/^{188}Os$ value ($^{187}Os/^{188}Os_{chon(i)}$ = 0.09531) and $^{187}Re/^{188}Os_{chon}$ is the $^{187}Re/^{188}Os$
1020 chondritic value ($^{187}Re/^{188}Os_{chon}$ = 0.40186). In the case of the Bushveld Complex, t is defined at
1021 2.06 Ga, which is the approximate age given from geochronology studies (Buick et al., 2001).The
1022 $^{187}Os/^{188}Os_{chon(t)}$ value will remain constant for samples of the same age (e.g. samples all from the

Table 5. Re and Os concentrations, Re-Os isotope values, and calculated γOs. See text for the γOs calculations.

	Re (ppb)	Os (ppb)	$^{187}Os/^{188}Os$	2SE	$^{187}Re/^{188}Os$	2SE	$^{187}Os/^{188}Os_i$	$^{187}Os/^{188}Os_{chon(t)}$	γOs_i
NG2-773.65	0.702	0.471	0.4450	0.0056	7.4844	0.0045	0.1837	0.1131	62.5
NG2-734.64	0.196	1.068	0.1390	0.0001	0.8841	0.0424	0.1081	0.1131	-4.37
NG2-706.53	0.003	0.080	0.1609	0.0002	0.2075	0.0843	0.1536	0.1131	35.9
NG2-689.73	0.359	0.355	0.3022	0.0002	4.9910	0.0367	0.1279	0.1131	13.2
NG2-604.5	0.259	0.198	0.3759	0.0002	6.5200	0.0489	0.1482	0.1131	31.1
NG2-591.5	0.292	1.020	0.1671	0.0001	1.3871	0.0289	0.1187	0.1131	4.97
NG2-553.0	0.289	0.522	0.2221	0.0002	2.6977	0.0217	0.1279	0.1131	13.1
NG2-450.53	0.268	0.812	0.1793	0.0001	1.5999	0.0094	0.1234	0.1131	9.15
NG2-377.48	0.226	5.617	0.1257	0.0000	0.1936	0.0013	0.1189	0.1131	5.18
NG2-219.9	0.166	0.372	0.1990	0.0001	2.1753	0.0100	0.1230	0.1131	8.84
NG2-197.0	0.152	2.318	0.1285	0.0001	0.3163	0.0024	0.1174	0.1131	3.86

Bushveld) but this value will need to be re-calculated for samples with different ages. The $^{187}Os/^{188}Os_{chon\ (t)}$ value for the Bushveld NG2 samples is calculated to be 0.1131 (Table 5).

The final calculation needed to determine γOs_i is equation 10. This calculation compares the $^{187}Os/^{188}Os_{sample\ (i)}$ with $^{187}Os/^{188}Os_{chon(t)}$. This comparison is particularly useful for comparing sets of data that are different ages, since the γOs_i is relative to the chondritic value at a given time (Day, 2013).

$$\gamma Os_i = [(^{187}Os/^{188}Os_{sample\ (i)})/(\ ^{187}Os/^{188}Os_{chon(t)}) - 1] \times 100 \qquad \text{eq. 10}$$

The γOs_i values for the Bushveld data range from -4.37 to +62.5 (Table 5). Only one sample (NG2-734.64) has a negative γOs_i value, whereas the remainder of the samples have positive γOs_i (Table 5). The majority of samples have γOs_i values between -4.37 to 13.2, with NG2-773.65, NG2-706.53, and NG2-604.5 being outliers that have γOs_i = 62.5, 35.9, and 31.1, respectively. Sample NG2-773.65 is the chilled margin sample and contains the highest γOs_i value from the NG2 sample suite. There does not appear to be a correlation between the abundance of sulphides and γOs_i values. Sample NG2-604.5 contains chromite and chalcopyrite with a 0.3 mod.%, and the γOs_i value for this sample is γOs_i = 31.1. Samples NG2-450.53 and NG2-377.48 have γOs_i values of +9.15 and +5.18, respectively. Sample NG2-450.53 contains chromite, pyrrhotite, and pentlandite with 0.6 mod.%, and NG2-377.48 has pyrrhotite, pentlandite, chalcopyrite, and chromite with 2.3 mod.%. Given by the γOs_i values of these samples, the opaque phases present, and modal

abundances of the opaque phases, it does not appear that these are correlated with each other. However, the Os concentrations for these samples may be correlated with opaque mineral abundances. Sample NG2-377.48 has the greatest modal abundance of opaque phases (2.3 mod.%) and also has the greatest Os concentration from the NG2 sample suite (5.617 ppb). Further, NG2-450.53 has a greater abundance of opaques (0.6 mod.%) and a higher Os concentration (0.812 ppb) than NG2-604.5 (0.3 mod.% for opaques and an Os concentration of 0.198 ppb). The abundances of HSE will be covered in section 5.8 below.

There is not a strong relationship between borehole depth and γOs_i values. The most radiogenic and unradiogenic samples are the two deepest of the suite from the borehole (Figure 9). However, the γOs_i values for sample NG2-591.5 and shallower samples show much more constrained values that range from γOs_i = 3.86 to 13.1. Additionally, γOs_i values show no correlation with the other isotopic systems used in this study (Figure 10c, 10e, and 10f). It could be interpreted that with increasing γOs_i values, εNd_i values increase as well. This correlation is weak, if even present, however.

5.8 Highly siderophile elements (HSE)

The NG2 samples were measured for HSE (Re, Pd, Pt, Ru, Ir, and Os) concentrations (Table 6). The range of HSE contents for the samples are the following: Re (0.00341 – 0.702), Pd (0.959

Table 6. Highly siderophile element concentrations for NG2 samples. Concentrations are in ppb.

	Re	Pd	Pt	Ru	Ir	Os
NG2-773.65	0.702	4.11	12.7	6.91	1.15	0.471
NG2-734.64	0.196	2.93	14.1	2.94	0.458	1.07
NG2-706.53	0.00341	24.6	14.5	5.99	0.628	0.0796
NG2-689.73	0.359	2.84	20.6	15.5	3.79	0.355
NG2-604.5	0.259	19.8	3.77	1.68	0.110	0.198
NG2-591.5	0.292	21.9	0.918	5.95	2.51	1.02
NG2-553.0	0.289	43.0	0.238	2.16	0.439	0.522
NG2-450.53	0.268	10.7	4.55	1.19	0.436	0.812
NG2-377.48	0.226	9.99	1.87	0.631	0.369	5.62
NG2-219.9	0.166	16.9	3.67	5.24	0.585	0.372
NG2-197.0	0.152	0.959	0.115	2.19	1.01	2.32
Average	*0.265*	*14.3*	*7.01*	*4.58*	*1.04*	*1.17*

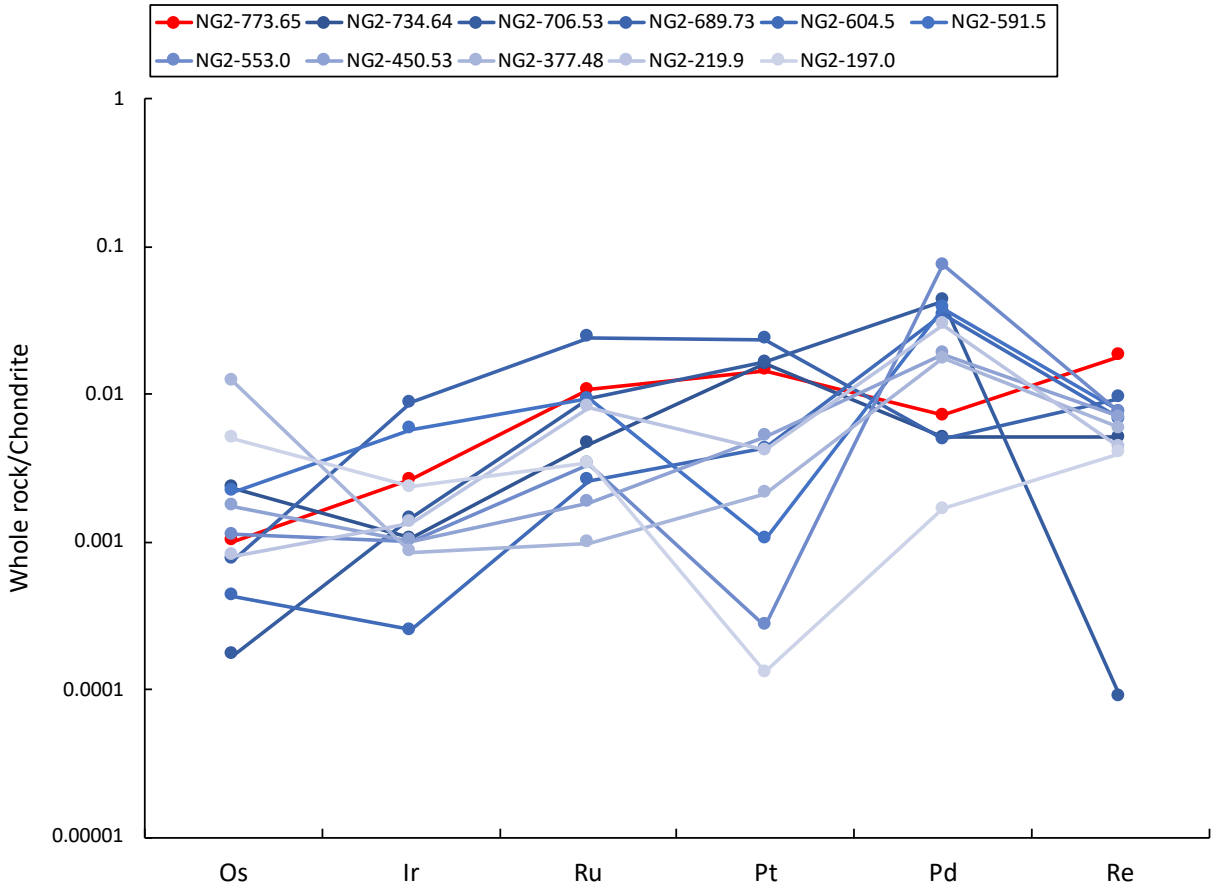

Figure 11. HSE (Os, Ir, Ru, Pt, Pd, Re) normalized to chondrite (Day et al., 2016a).

– 43.0), Pt (0.115 – 20.6), Ru (0.631 – 15.5), Ir (0.110 – 3.79), and Os (0.0796 – 5.62). When normalized to chondrite, the HSE show variable trends (Figure 11). However, most samples show an enrichment in Pd relative to Pt. Three samples, NG2-773.65, NG2-734.64, and NG2-689.73, show the opposite relationship. Additionally, the HSE are plotted versus borehole depth in Figure 9 as iridium-group PGE (IPGE) and the platinum-group PGE (PPGE) + Re. The PPGE + Re are more variable than the IPGE with depth. These PGE groups do not appear to correlate with each other or with any of the isotopic values that are also plotted in Figure 9. Further, in Figures 12 - 14 the HSE are plotted against each other. There is lack of any strong relationship among the HSE, with the exception of a slight positive correlation for Ru vs. Pt (Figure 14b). As mentioned above, there may be a relationship between opaque mineral abundances and the concentration of Os in the samples. For the other HSE this does not appear to be the case. All three samples discussed above

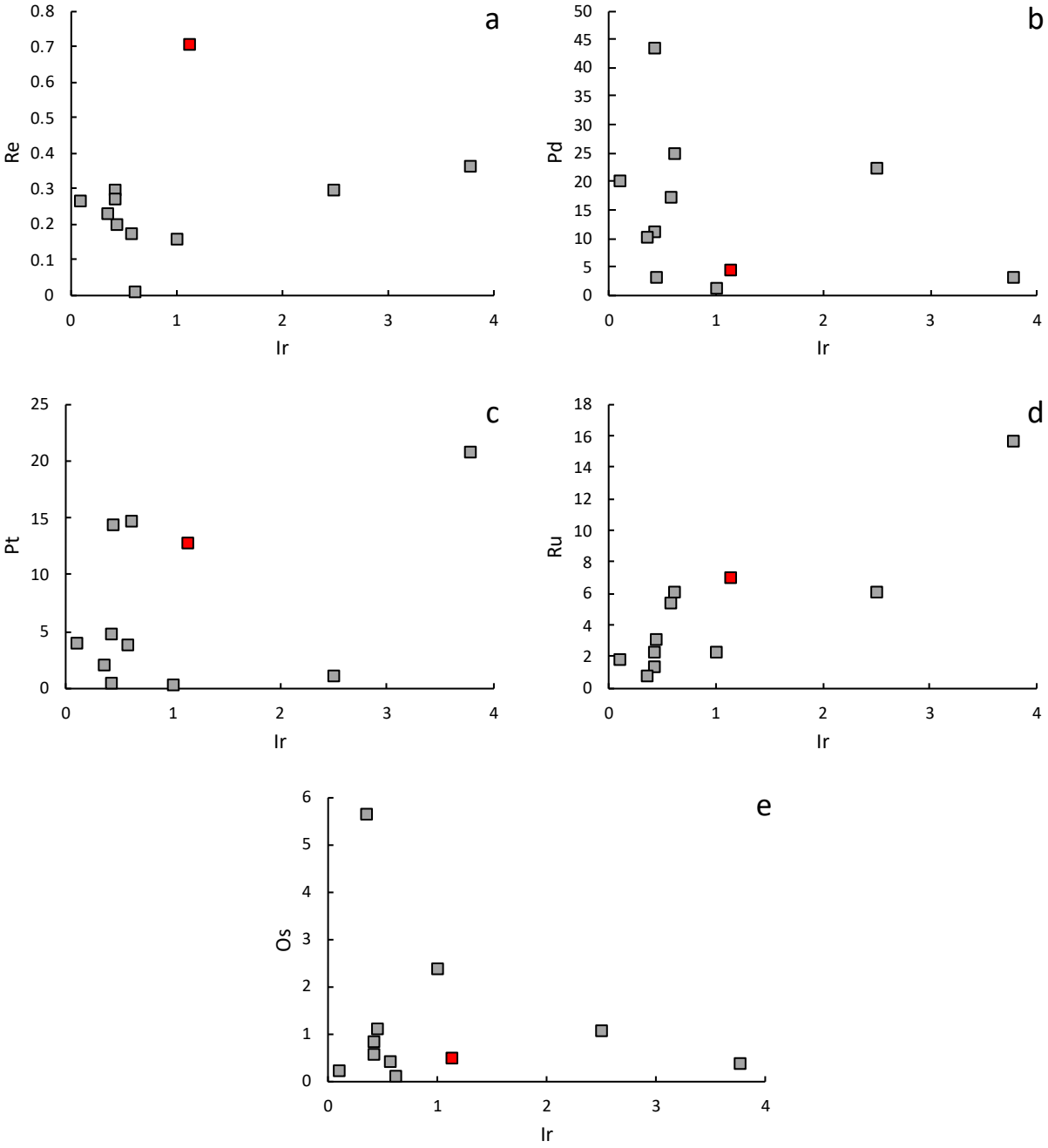

Figure 12. Scatter plot comparisons among HSE with respect to Ir. (a) Re, (b) Pd, (c) Pt, (d) Ru, and (e) Os. All HSE concentrations are in ppb. The red squares with black outlines represent sample NG2-773.65, the chilled margin sample.

contain very similar concentrations of Re, Pt, Ru, and Ir (Table 6). The Pd contents for these samples are different, however, in which NG2-604.5 has a higher concentration (19.8 ppb) than

NG2-450.53 (10.7 ppb) and NG2-377.48 (9.99 ppb). These are opposite to the Os concentrations in these samples.

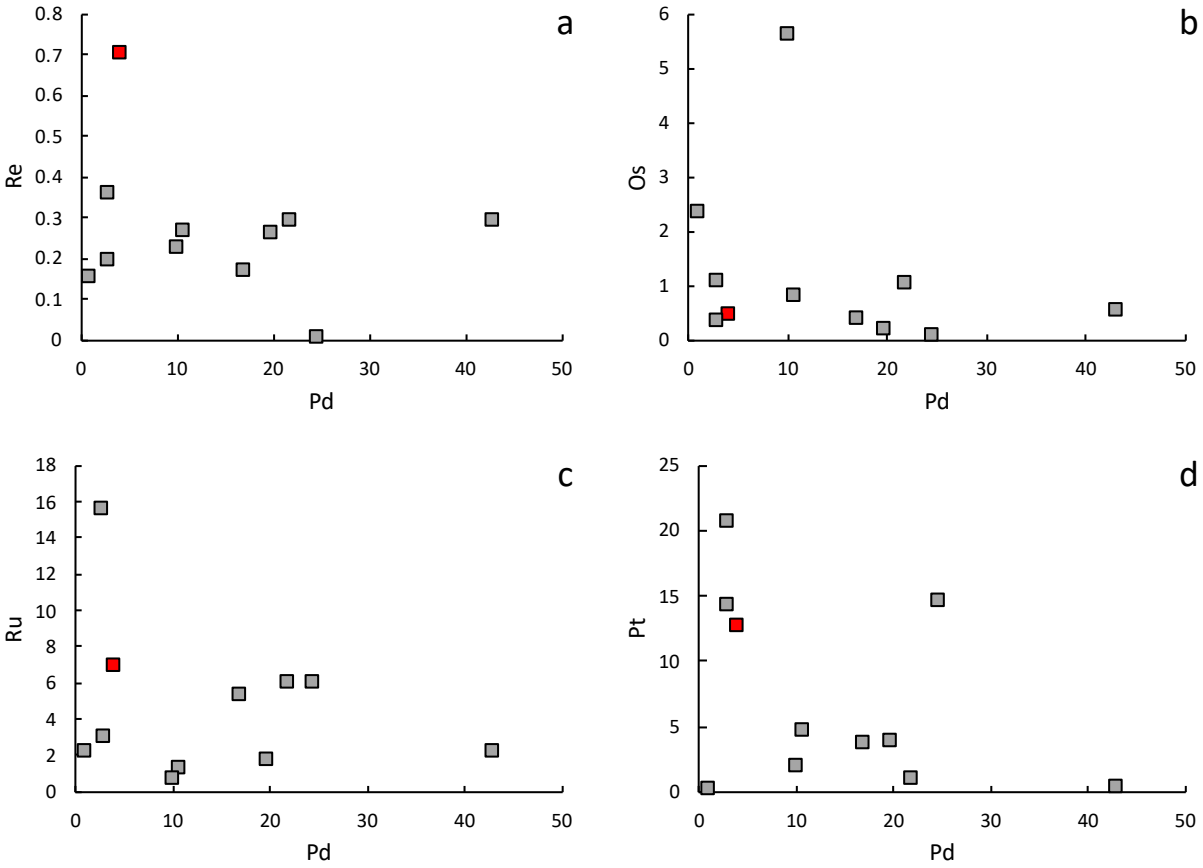

Figure 13. HSE scatter plots with respect to Pd. (a) Re, (b) Os, (c) Ru, and (d) Pt. All HSE concentrations are in ppb. The red squares with black outlines represent sample NG2-773.65, the chilled margin sample.

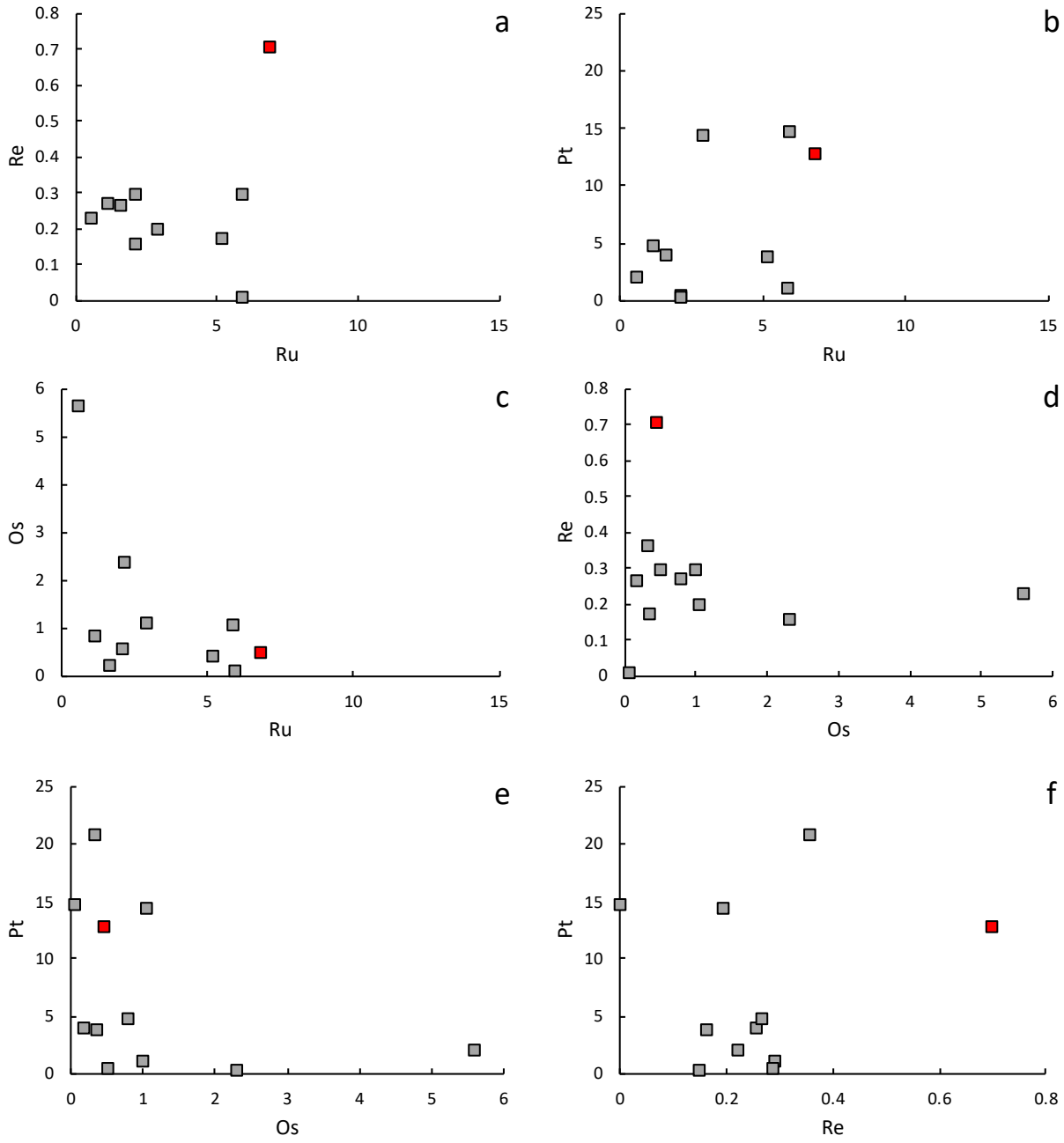

Figure 14. Comparisons between HSE. (a) Ru vs Re, (b) Ru vs Pt, (c) Ru vs Os, (d) Os vs Re, (e) Os vs Pt, and (f) Re vs Pt. All HSE concentrations are in ppb. The red squares with black outlines represent sample NG2-773.65, the chilled margin sample.

6. Discussion

6.1 Comparison with Bushveld literature data

Major element data for the NG2 sample suite contain characteristically high SiO_2 (38.2 – 54.7 wt.%) and MgO contents (26.3 – 41.4 wt.%), in agreement with published data for the Lower Zone (e.g. Maier et al., 2000; Godel et al., 2011). In addition, FeO contents range from 7.9 – 12.2 wt.% for the NG2 suite, which are similar to the range of values for published data (e.g. Maier et al., 2000; Godel et al., 2011). Chilled margin sample NG2-773.65 contains SiO_2 (52.3 wt.%) and FeO (9.4 wt.%) similar to the NG2 suite. In contrast to the NG2 suite, sample NG2-773.65 contains lower MgO (13.8 wt.%), higher Al_2O_3 (11.2 wt.%), CaO (7.6 wt.%), Na_2O (1.8 wt.%), and K_2O (0.6 wt.%). The major element geochemistry for NG2-773.65 is in agreement with published data for chilled margin samples from the eastern and western limbs of the Bushveld (e.g. Wilson, 2012; Maier et al., 2016). Thus, the sample NG2-773.65 is a chilled margin sample and is not related to the rest of the NG2 Lower Zone samples analysed in this study.

Trace element profiles between the NG2 suite, NG2-773.65, and published data on the Lower Zone are very similar despite the differences in major element data between the LZ and chilled margin samples. The only major difference between NG2 samples, NG2-773.65, and published Lower Zone data is that NG2-773.65 has greater concentrations of trace elements (Figures 15 & 16). This greater enrichment in trace elements for NG2-773.65 is also observed for other chilled margin samples relative to the NG2 suite and Lower Zone (Figures 15 & 16) (e.g. Wilson, 2012; Maier et al., 2016). Additionally, the NG2 sample suite and NG2-773.65 have similar trace element profiles as the B1 rocks, which are the best estimate for the parental composition to the Lower Zone (Figures 15 & 16) (e.g. Barnes et al., 2010). However, the B1 rocks have greater trace element concentrations than NG2 samples and published Lower Zone data, similar to NG2-773.65 and chilled margin rocks (Figures 15 & 16) (e.g. Barnes et al., 2010). The NG2 samples, NG2-773.65, published Lower Zone data, and B1 rocks all have an enrichment in LILE and LREE over HFSE and HREE, respectively, as well as large positive Pb and negative Nb anomalies in primitive mantle normalized diagrams (Figures 15 & 16) (e.g. Maier et al., 2000; Barnes et al., 2010; Godel et al., 2011; Wilson, 2012; Maier et al., 2016).

Oxygen isotope values for the NG2 sample suite also agree with published data on the Lower Zone (Figure 17) (e.g. Harris et al., 2005). Published $\delta^{18}O$ values for Lower Zone olivine and orthopyroxene separates range from $\delta^{18}O$ = 5.60 – 7.60‰ (Harris et al., 2005), and the NG2 sample suite contain $\delta^{18}O$ = 5.60 – 6.70‰. Further, the NG2 suite has overlapping $\delta^{18}O$ value ranges to the Marginal Zone ($\delta^{18}O$ = 6.60‰ – 7.80‰), Critical Zone ($\delta^{18}O$ = 6.20‰ – 7.10‰), Main Zone ($\delta^{18}O$ = 5.80‰ – 13.10‰), and the Upper Zone ($\delta^{18}O$ = 5.80‰ – 10.40‰) (Figure 16) (Harris et al., 2005). Sample NG2-773.65 has higher $\delta^{18}O$ values ($\delta^{18}O$ = 9.42‰ and 9.78‰) than the NG2 suite and any of the other zones of the Bushveld, with the exception of a plagioclase separate from the Main Zone that contains $\delta^{18}O$ = 13.1‰ (Figure 17). In addition to NG2 suite $\delta^{18}O$ values agreeing with published data for the Bushveld *sensu stricto*, NG2 sample $\delta^{18}O$ values

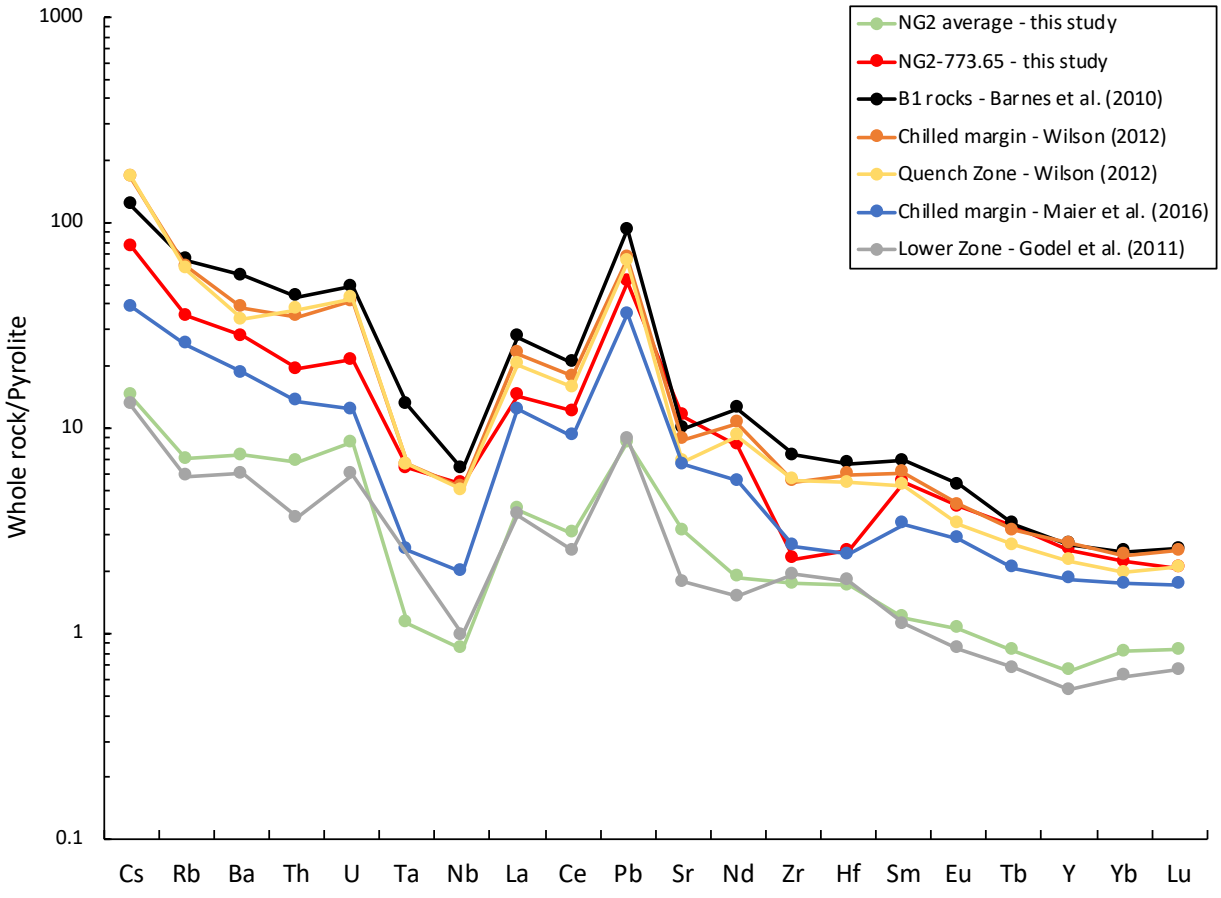

Figure 15. Trace element diagram showing the average values for the NG2 suite, B1 rocks, chilled margin samples, quench zone samples, Lower Zone, and sample NG2-773.65.

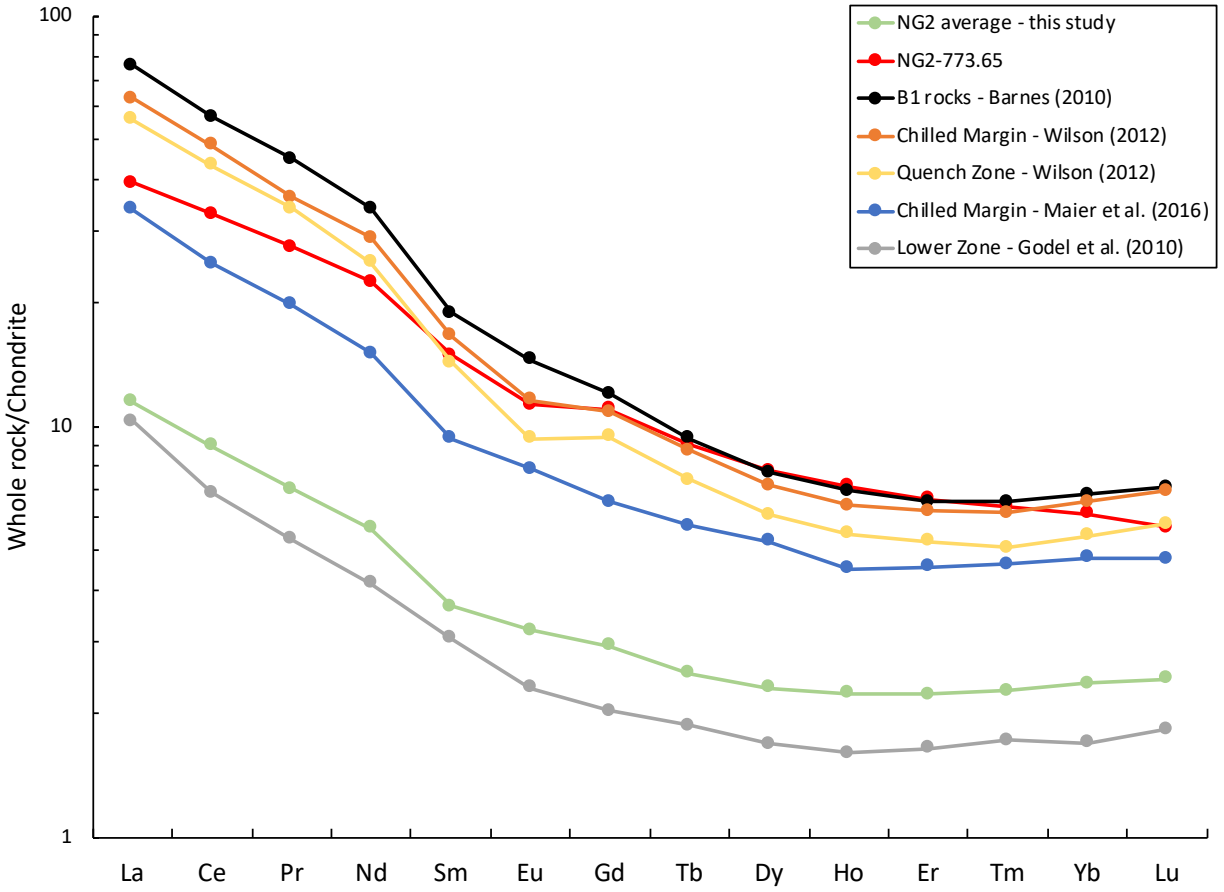

Figure 16. REE diagram showing the relative concentrations and trends for the same suite of samples from Fig. 15.

overlap with Bushveld-related Driekop, Mooihoek, and Onverwacht platiniferous dunite pipes with $\delta^{18}O$ values (5.70‰ – 7.40‰) (Günther et al., 2018). To the author's knowledge this is the first report of a $\delta^{18}O$ value for a chilled margin sample for the Bushveld. As a result, this sample is unable to be compared to any other chilled margin samples from the Bushveld. The oxygen isotope compositions for NG2 samples, NG2-773.65, and the Bushveld overall are generally greater than mantle values (Mantle $\delta^{18}O$ = 5.70‰; Eiler, 2001), suggesting that the Bushveld magmas assimilated large portions of the crust, recycled crust in the mantle, or a different EM source (Harris et al., 2005; Harris et al., 2015; Günther et al., 2018). This will be discussed in detailed below in section 6.2.

Strontium isotopes for the NG2 suite range from $^{87}Sr/^{86}Sr_i$ = 0.7043 – 0.7086, and previous $^{87}Sr/^{86}Sr_i$ values for the Lower Zone range from $^{87}Sr/^{86}Sr_i$ = 0.7044 - 0.7074 (Kruger, 1994; Maier et al., 2000). Only sample NG2-604.5 has a value ($^{87}Sr/^{86}Sr_i$ = 0.7086) that falls outside of this

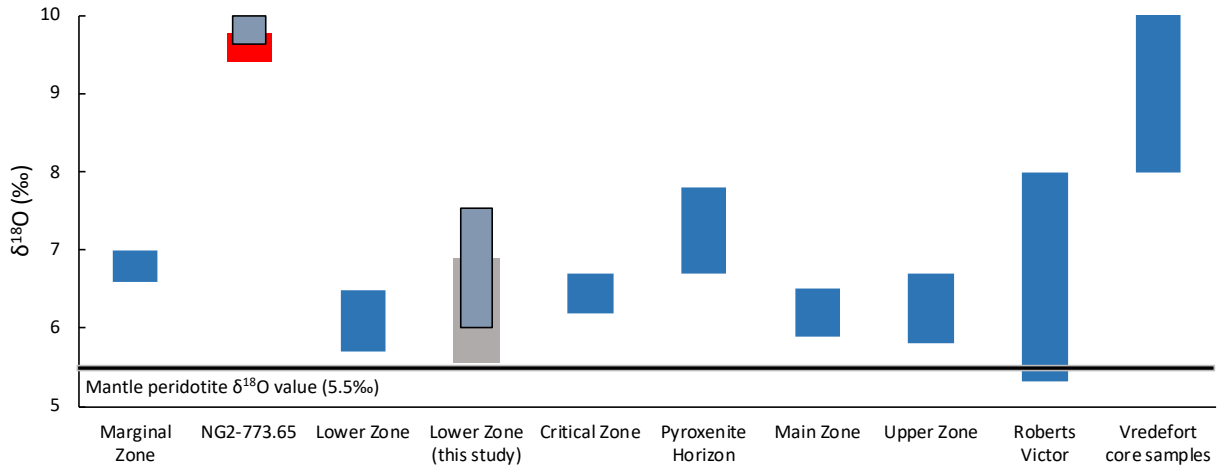

Figure 17. Oxygen isotope ranges for each zone of the Bushveld Complex and the Pyroxenite Horizon, as well as the range in values for the NG2 borehole suite measured in this study. The Pyroxenite Horizon is a ~1 m – thick layer of feldspathic pyroxenite 400 m below the MZ-UZ boundary from the Bellevue borehole in the Northern Limb (Harris et al., 2005). In addition to the Bushveld, ranges for Roberts Victor eclogites and the crustal sequence of the Vredefort impact structure oxygen isotopes are included. Published Bushveld, Roberts Victor eclogites, and Vredefort crust come from MacGregor and Manton (1986); Schulze et al., (2000); Harris et al., (2005); Fagereng et al., (2008); Riches et al., (2016). Further, blue-grey boxes overlaying NG2-773.65 and the NG2 suite (grey box) represent the range in $\delta^{18}O$ values for the calculated magma values for NG2 olivine and orthopyroxene separates. Black bar is for mantle peridotite $\delta^{18}O$ value (5.5‰; Eiler, 2001) reference.

range. Given this, the $^{87}Sr/^{86}Sr_i$ values reported for the NG2 suite are in good agreement with published data for the Lower Zone. Sample NG2-773.65 has $^{87}Sr/^{86}Sr_i = 0.7050$, which fits near the middle of values for the NG2 suite. Further, this value agrees with published $^{87}Sr/^{86}Sr_i$ values for chilled margin rocks, where $^{87}Sr/^{86}Sr_i = 0.7049 – 0.7059$ (e.g. Maier et al., 2016).

Only two samples from the Lower Zone in the literature have been analysed for Sm-Nd isotopes where the εNd_i values are εNd_i = -5.4 and -6.0 (Maier et al., 2000). The range in εNd_i values for the NG2 suite are -7.40 to -5.30, and sample NG2-773.65 has εNd_i = -4.97. This range is in good agreement with the small sample size for the Lower Zone (Maier et al., 2000). To the authors knowledge there are no published εNd_i values for Bushveld chilled margin samples.

This is the first study reporting osmium isotope values for the Lower Zone. The NG2 suite contains γOs_i = -4.37 to +35.9, and chilled margin sample NG2-773.65 contains γOs_i = +62.5 (Figures 18 & 19). The range in γOs_i values are similar to the ranges for osmium isotope studies for the Critical Zone and the Platreef, where γOs_i = +1.8 to +71.4 (Figures 18 & 19) (McCandless et al., 1999; Schoenberg et al., 1999; Reisberg et al., 2011). However, most γOs_i values from these studies range γOs_i = +20 to +72, which are more radiogenic than all NG2 samples with the

exception of NG2-706.53 and NG2-604.5 (McCandless et al., 1999; Schoenberg et al., 1999; Reisberg et al., 2011).

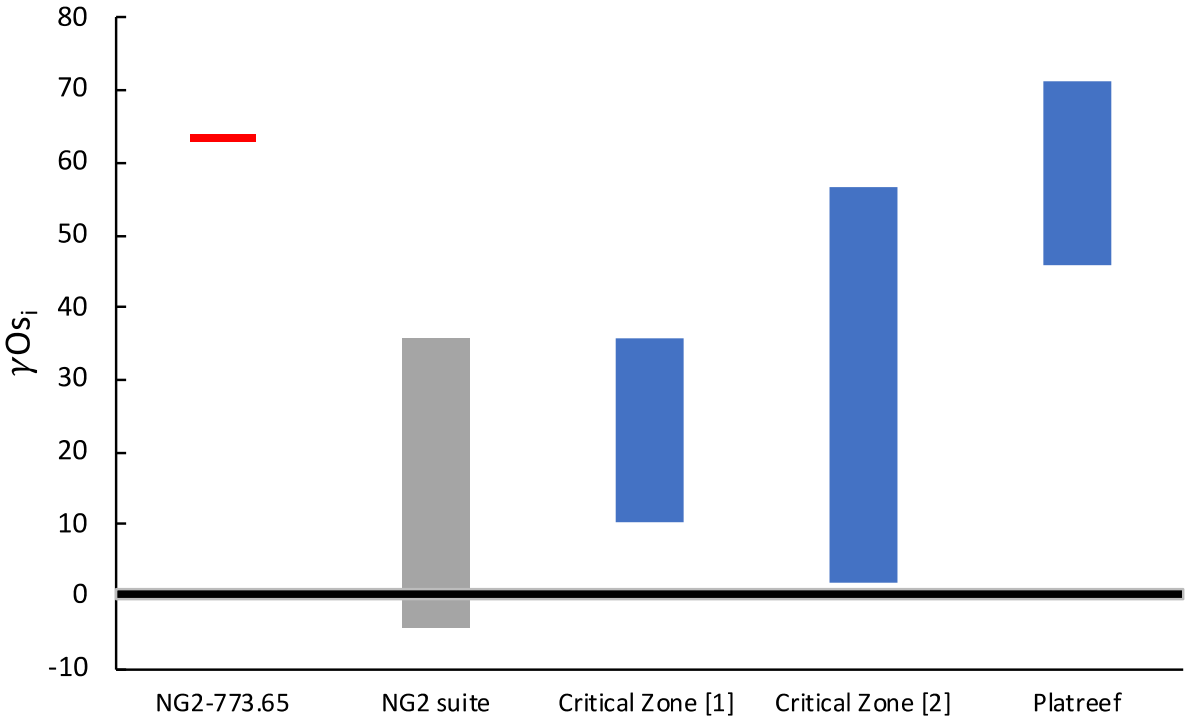

Figure 18. The γOs_i value ranges for NG2-773.65, the NG2 suite, and published Critical Zone ([1] McCandless et al., 1999; [2] Schoenberg et al., 1999), and Platreef (Reisberg et al., 2011) values.

Sample NG2-734.64 is the first report of unradiogenic γOs_i (γOs_i = -4.37) for the Bushveld Complex, an indicator for an H-SCLM source. However, the standard error bars of two samples from the NG2 suite and two samples from the Schoenberg et al. (1999) Merensky Reef suite overlap into unradiogenic γOs_i values (Figure 19). These error values that overlap into negative γOs_i values reinforces the claim that samples from the Lower Zone, and the Bushveld Complex as a whole, assumed melts from the H-SCLM.

Published HSE data have been reported for the Lower Zone prior to this study (Lee and Tredoux, 1986; Maier and Barnes, 1999; Barnes and Maier, 2002). The ranges of HSE values for the Lower Zone are Os = 1 – 4.9 ppb, Ir = 0.3 – 0.69 ppb, Ru = 0.59 – 66 ppb, Pt = 2 – 88.9 ppb, Pd = 4 – 87 ppb, and the range of HSE values for the NG2 suite are as follows: Os = 0.08 – 5.6 ppb, Ir = 0.11 – 3.78 ppb, Ru = 0.631 – 15.48 ppb, Pt = 0.115 – 20.62 ppb, and Pd = 0.96 – 42.99 ppb

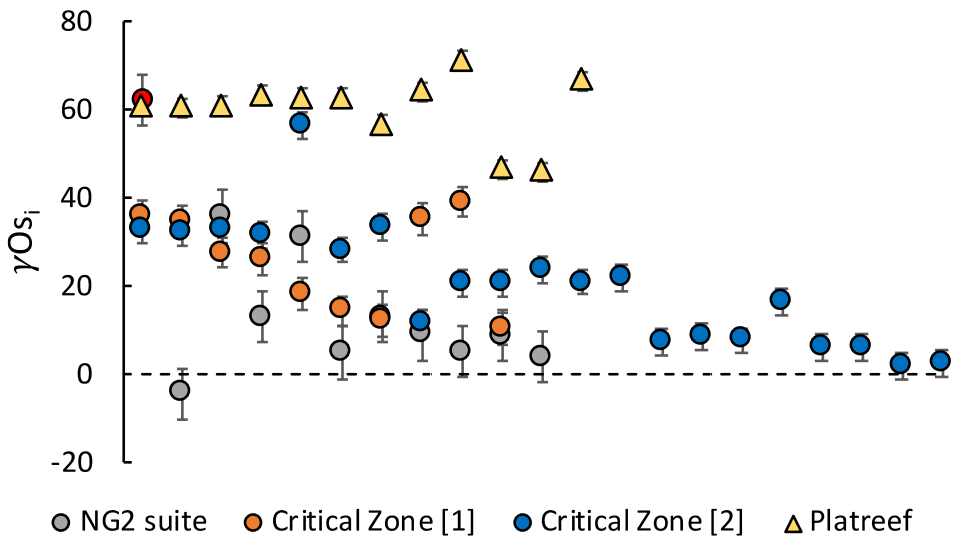

Figure 19. Comparison of γOs_i values for Bushveld samples analysed for Os-Os isotopes. Included are samples from the NG2 suite (this study), published Critical Zone ([1] McCandless et al., 1999; [2] Schoenberg et al., 1999) and Platreef (Reisberg et al., 2011) values. The red circle is sample NG2-773.65. Standard error bars, and a $\gamma Os_i = 0$ dashed reference line included.

(Figure 20) (Lee and Tredoux, 1986; Maier and Barnes, 1999). The ranges between the published data for the Lower Zone and NG2 sample suite overlap relatively well. The published data for the Lower Zone contains a tighter range for Ir, and greater ranges for the other HSE with the exception of Os values in which these are very similar for these sample sets (Lee and Tredoux, 1986; Maier and Barnes, 1999). Figure 20a, 20b, and 20d show no correlations between HSE data for the NG2 suite and published data for the Lower Zone. However, Figure 20c shows a strong correlation for Ir versus Ru other than the five samples with Ir > 3.7 ppb. Additionally, there is significant overlap in Pd and Pt concentrations for the NG2 suite, NG2-773.65, and published data for the Lower, lower Critical, upper Critical, and Main Zones of the Bushveld (Figure 21). Most values for these zones fall between Pd = 1 – 15 ppb and Pt = 1 – 100 ppb, in which the values are 'clumped' together and show no trend (Figure 21). There is a positive trend between Pd and Pt for samples that contain Pd values greater than 15 ppb, however (Figure 21). The NG2 samples mostly plot with the published data with the lowest Pt and median Pd concentrations (Figure 21). Further, there are three NG2 samples that plot away from the main grouping of Pd and Pt values for the Bushveld due to lower Pt concentrations (Figure 21). One of these samples (NG2-197.0) is not observed in the figure but contains Pd = 0.96 ppb and Pt = 0.11 ppb.

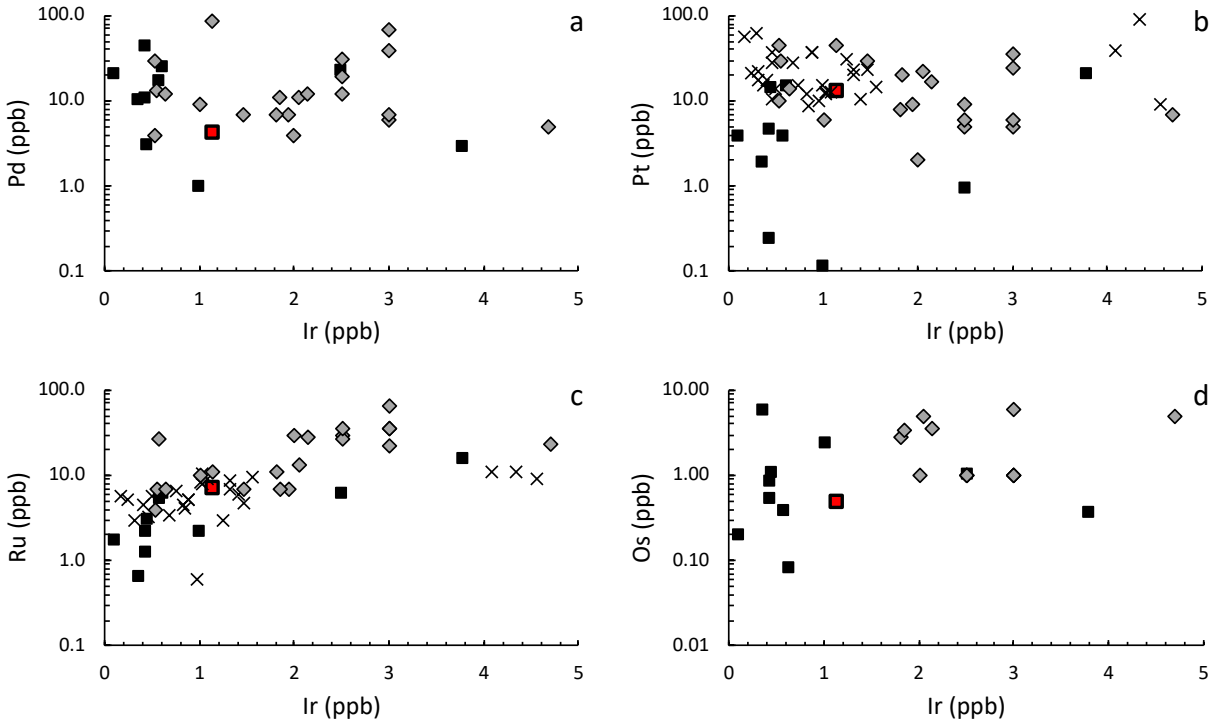

Figure 20. Variations in Pd (a), Pt(b), Ru (c), and Os (d) concentrations versus Ir for the NG2 suite (black squares), NG2-773.65 (red squares), and published data for Lower Zone silicate rocks from Lee and Tredoux (1986) (black X's), and Maier and Barnes (1999) (grey diamonds). Note that Lee and Tredoux (1986) did not report Re, Pd, and Os concentrations, and Maier and Barnes (1999) did not report Re concentrations, which is why there is no Ir versus Re plot here.

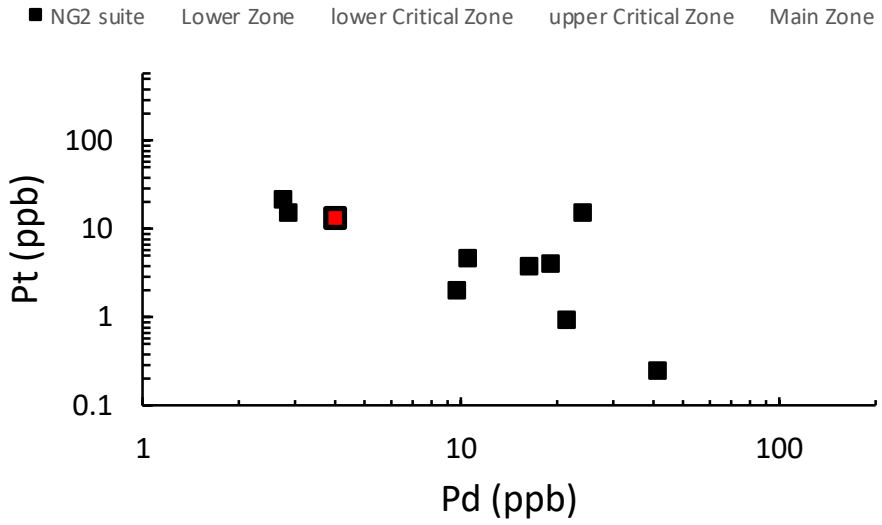

Figure 21. Plot of Pd versus Pt for the NG2 suite samples, NG2-773.65 (red square), published Lower Zone (Teigler, 1990; Maier and Barnes, 1999), lower Critical Zone (Lee and Parry, 1988; Teigler, 1990; Maier and Barnes, 1999), upper Critical Zone (Lee and Parry, 1988; Teigler, 1990; Maier and Barnes, 1999), and Main Zone (Harney et al., 1990; Maier and Barnes, 1999) data.

The HSE trends for the NG2 suite are extremely variable and have different trends than published average HSE values for the Lower Zone (Barnes and Maier, 2002) (Figure 22). The average published Lower Zone data overall have greater HSE concentrations than most NG2 samples and NG2-773.65, and Pt and Ru concentrations greater than all NG2 samples and NG2-773.65 (Figure 22).

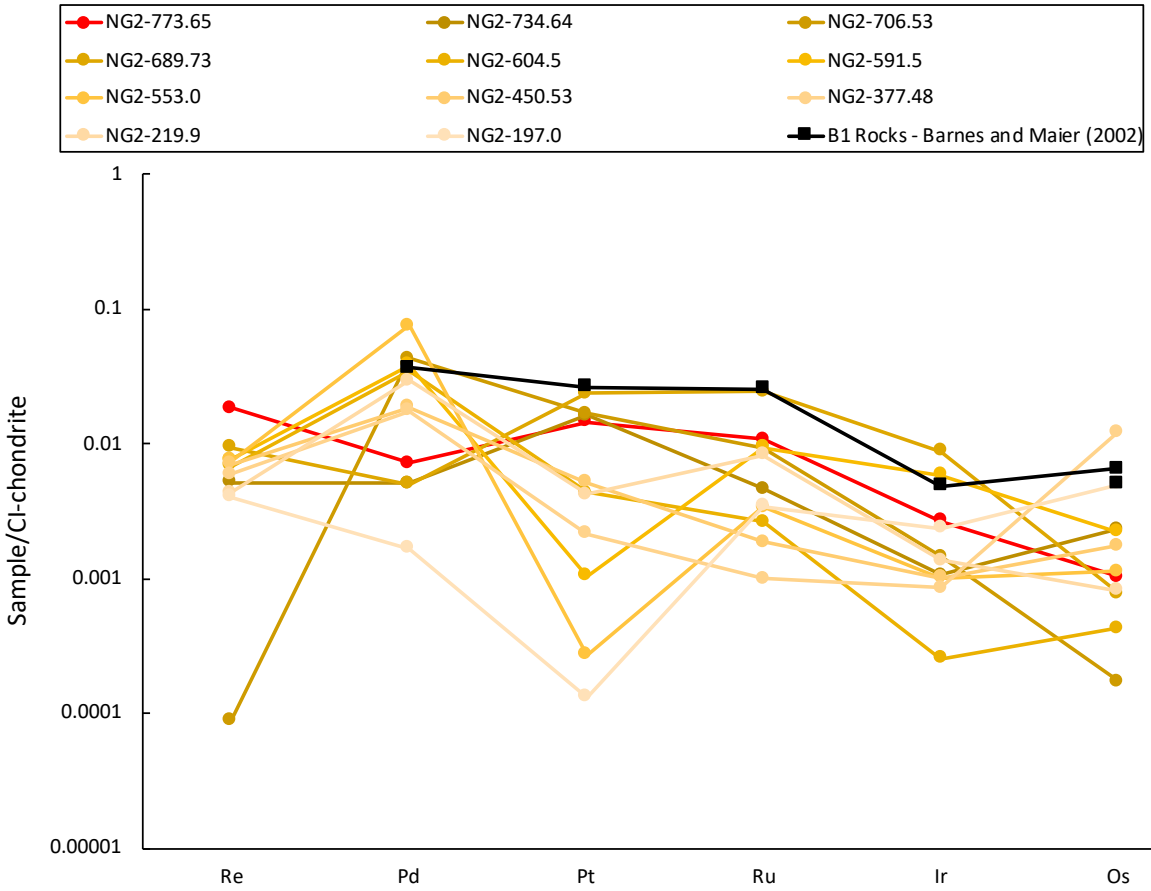

Figure 22. Comparisons in HSE data relative to CI chondrite (Day et al., 2016a) for the NG2 sample suite (shades of yellow), NG2-773.65 (red), and average values for Lower Zone silicate rocks (black) (Barnes and Maier, 2002).

6.2 $\delta^{18}O$ values and correlations with Sr-Nd-Os isotopes: constraints on crustal assimilation for the Lower Zone

The $\delta^{18}O$ values for olivine and pyroxene of the NG2 suite ($\delta^{18}O$ = 5.56 – 8.03‰) and chilled margin sample NG2-773.65 ($\delta^{18}O$ = 9.42 – 9.78‰) are higher than typical mantle

peridotite $\delta^{18}O$ (5.50‰; Eiler, 2001), although one NG2 olivine separate has a similar $\delta^{18}O$ value (NG2-706.5 $\delta^{18}O$ = 5.56‰) (Figure 17). By analysing mineral separates for the major element $\delta^{18}O$, these values reflect parent magma compositions and not interstitial liquid or late-stage alteration processes.

Experimental studies on, and calculations of, oxygen isotope fractionation in silicate minerals show that oxygen isotopes in mantle-derived rocks are often in disequilibrium (Mattey et al., 1994). Further, it has been shown that oxygen isotopes show a relative fractionation trend of $\delta^{18}O$ in orthopyroxene > clinopyroxene > olivine in mantle-derived rocks (e.g. Zheng, 1993; Mattey et al., 1994). Five samples from the NG2 suite had both olivine and pyroxene (orthopyroxene or clinopyroxene) analysed for $\delta^{18}O$. Two of these samples contain higher $\delta^{18}O$ values for orthopyroxene than olivine, as would be expected. Further, one sample that had both olivine and clinopyroxene analysed contains a higher $\delta^{18}O$ value for clinopyroxene over olivine. The $\delta^{18}O$ enrichment for pyroxenes over olivine is also observed in previously reported Bushveld and Bushveld-related samples (e.g. Harris et al., 2005; Günther et al., 2018). These inter-mineral $\delta^{18}O$ differences can be attributed to either (1) fractionation differences or (2) different equilibration temperatures with the magma (Harris et al., 2015). Further, these differences are likely not to have been caused by alteration or the assimilation of crustal materials (Harris et al., 2015). Differences in equilibrium temperatures may also be the cause of these differences and can be calculated using fractionation (Δ) constants (Bindeman et al., 2004; Harris et al., 2015). The magma $\delta^{18}O$ fractionation constants are -0.65 for olivine and -0.21 for orthopyroxene in a magma with ~48 wt.% SiO_2 composition (Bindeman et al., 2004). When these fractionation values are applied to the NG2 olivine and orthopyroxene $\delta^{18}O$ values (Δmineral – magma = fractionation value; can be also written as: Δmineral - fractionation value = magma), every sample has higher $\delta^{18}O$ values for olivine over their orthopyroxene counterpart, except for NG2-706.5 which retains a higher calculated magma $\delta^{18}O$ value for orthopyroxene over olivine (Table 7). The range of calculated magma olivine $\delta^{18}O$ values for the NG2 suite is $\delta^{18}O$ = 6.21 – 7.54‰, and the range is $\delta^{18}O$ = 6.00 – 8.24‰ for calculated magma orthopyroxene (Table 7). Sample NG2-706.5 contains a calculated magma $\delta^{18}O$ value of $\delta^{18}O$ = 6.21‰ for olivine and $\delta^{18}O$ = 6.53‰ for orthopyroxene (Table 7). Regardless of the differences in $\delta^{18}O$ values between olivine and orthopyroxene

Table 7. Olivine and orthopyroxene magma $\delta^{18}O$ values for the NG2 suite. These values were determined from the addition of fractionation values for olivine (-0.65) and orthopyroxene (-0.21) calculated for a magma with SiO_2 = 48 wt.% (Bindeman et al., 2004; Harris et al., 2015). [Δmineral – magma = fractionation value (Bindeman et al., 2004; Harris et al., 2015)].

	Olivine magma δ18O	Orthopyroxene magma δ18O	Opx magma δ18O - 2	Opx magma δ18O - 3
NG2-773.65	-	9.99	9.63	6.70
NG2-734.64	6.32	-	-	-
NG2-706.5	6.21	6.53	-	-
NG2-689.73	7.54	6.69	-	-
NG2-604.5	6.93	6.69	-	-
NG2-591.5	6.71	6.48	-	-
NG2-553.0	-	6.70	-	-
NG2-524.8	6.32	-	-	-
NG2-450.53	7.32	-	-	-
NG2-426.6	-	6.45	-	-
NG2-377.48	7.21	6.00	-	-
NG2-219.9	-	6.39	-	-
NG2-197.0	-	8.24	6.53	-

separates for the NG2 suite and NG2-773.65, the $\delta^{18}O$ values for these samples are much higher than mantle peridotite (5.50‰; Eiler, 2001).

Mass balance calculations by Harris et al. (2005) determined that 41% assimilation of crust from the nearby (150 km to the south) Vredefort impact structure, with $\delta^{18}O$ = 9.15, is required to raise a MORB mantle derived $\delta^{18}O$ composition (MORB mantle = 5.70‰; Eiler, 2001) to $\delta^{18}O$ = 7.10‰. Vredefort crust is utilised as it is the most likely candidate for crustal assimilation processes due to their exposure and proximity to the Bushveld, in addition to it being older than the Bushveld (e.g. Hart et al., 1990; Lana et al., 2003; Harris et al., 2005). Further, assimilation of 36% crustal materials with $\delta^{18}O$ = 9.60‰ (Limpopo metapelite) is required to raise a mantle-derived melt with a $\delta^{18}O$ = 5.70‰ to $\delta^{18}O$ = 7.10‰ (Harris et al., 2005; Harris et al., 2015). Thus, estimates on the degree of crustal assimilation to account for the elevated $\delta^{18}O$ signature for the Bushveld (Lower Zone – Upper Zone) ranges from 20 – 41% crustal material, and 35% for Bushveld-related platiniferous pipes with similar $\delta^{18}O$ values to the NG2 suite (e.g. Maier et al., 2000; Harris et al., 2005; Harris et al., 2015; Maier et al., 2016; Günther et al., 2018). Further, the utilisation of other geochemical and isotopic systems (i.e. major elements, trace elements, Sr and Nd isotopes) estimate 20% crustal assimilation (Maier et al., 2000) for Lower Zone samples and 35% for B1 rocks (Maier et al., 2016). The $\delta^{18}O$ values for the Vredefort crust have a general range of 8.00‰ – 10.00‰ (Figure 17), and the mixing of these rocks with a mantle-derived magma

could produce the $\delta^{18}O$ composition of Bushveld rocks. Here, mass balance calculations for the NG2 suite show that 36% and 27% assimilation of Vredefort crust is required ($\delta^{18}O$ = 9.15‰; Harris et al., 2005; Harris et al., 2015) by a mantle-derived magma in equilibrium with mantle peridotite ($\delta^{18}O$ = 5.50‰; Eiler, 2001) to account for the average $\delta^{18}O$ values of calculated magma NG2 suite olivine (6.82‰) and orthopyroxene (6.50‰) (Table 7), respectively. When using MORB, $\delta^{18}O$ = 5.7‰, and Vredefort crust, the degree of crustal assimilation to raise $\delta^{18}O$ = 5.7‰ to $\delta^{18}O$ = 6.82‰ and 6.50‰ is 33% and 23%, respectively (Eiler, 2001; Harris et al., 2005; Harris et al., 2015). These calculated values are similar to previous estimates discussed above.

Alternatively, the Bushveld magmas could have sourced the elevated $\delta^{18}O$ from a recycled crustal component in the mantle source (Richardson and Shirey, 2008; Harris et al., 2015; Günther et al., 2018). The SCLM beneath the Bushveld contains high $\delta^{18}O$ values, in which oxygen isotopes of eclogite xenoliths from Roberts Victor range $\delta^{18}O$ = 5.32‰ up to $\delta^{18}O$ = 8.00‰ (Figure 17) (e.g. MacGregor and Manton, 1986; Schulze et al., 2000; Riches et al., 2016). Mass balance calculations for the interaction of the E-SCLM, using an upper end-member $\delta^{18}O$ = 8.00‰ (e.g. MacGregor and Manton, 1986; Schulze et al., 2000; Riches et al., 2016), with Kaapvaal Craton peridotite xenolith ($\delta^{18}O$ = 5.19‰; Mattey et al., 1994) requires 58% and 47% E-SCLM input to account for the average calculated magma composition for NG2 olivine (6.82‰) and orthopyroxene (6.50‰) separates, respectively. Alternatively, the interaction of mantle peridotite that has $\delta^{18}O$ = 5.50‰ with E-SCLM ($\delta^{18}O$ = 8.00‰) materials would require 40% and 53% E-SCLM materials to raise mantle peridotite $\delta^{18}O$ to 6.50‰ and 6.82‰, respectively. The E-SCLM contains lower $\delta^{18}O$ values than the Vredefort crust, requiring more E-SCLM materials than Vredefort crust to raise a mantle-derived melt with $\delta^{18}O$ = 5.19‰ and 5.50‰ to $\delta^{18}O$ = 6.50‰ and 6.82‰.

It's also possible that metasomatism involving the release of high $\delta^{18}O$ fluids from subducting crust (i.e. eclogite) beneath the Kaapvaal Craton may have impacted the $\delta^{18}O$ values for the H-SCLM in addition to the E-SCLM (e.g. Eiler et al., 1998; Liu et al., 2014; Heinonen et al., 2018). The high $\delta^{18}O$ values for some Antarctic Karoo rocks are interpreted as being caused by metasomatic activity from the release of fluids from subducting slabs (Heinonen et al., 2018). In this case, it is difficult to calculate the $\delta^{18}O$ input from the SCLM since there are no xenoliths that

contain high values, with the exception of Roberts Victor eclogite samples (e.g. MacGregor and Manton, 1986; Schulze et al., 2000; Harris et al., 2015; Riches et al., 2016).

Sample NG2-773.65 contains much higher $\delta^{18}O$ values than the NG2 suite and Roberts Victor eclogites (Figure 17). Further, the $\delta^{18}O$ values for NG2-773.65 overlap with Vredefort core samples (Figure 17). This greater enrichment in $\delta^{18}O$ values for NG2-773.65 compared to the NG2 suite and Roberts Victor eclogites suggests that this sample obtained its $\delta^{18}O$ character solely from the crust, or from a large component of E-SCLM followed by crustal assimilation. Further, this sample likely had more input from crustal assimilation than the Lower Zone samples. Overall, the $\delta^{18}O$ signatures in the NG2 suite require a high degree of sourced crustal materials, either by crustal assimilation or sourcing recycled crust in the mantle.

6.3 Primary versus secondary Os-isotope signatures

The Re-Os system has the ability to discriminate between materials sourced from the core-mantle boundary, asthenosphere, SCLM, and crust (e.g. Day, 2013). Studies have proposed that the RLS sourced the crust and/or an enriched mantle source, such as the SCLM (e.g. Davies, 1980; Barnes, 1989; McCandless and Ruiz, 1991; Harmer et al., 1995; McCandless et al., 1999; Schoenberg et al., 1999; Maier et al., 2000; Harris et al., 2005; Richardson and Shirey, 2008; Barnes et al., 2010; Reisberg et al., 2011; Harris et al., 2015; Günther et al., 2018). The Re-Os isotope system has the potential to determine if the crust, SCLM, or both, were sources of the Bushveld magmas due to its unique differences in compatibilities between Re and Os and resultant distinct γOs_i for different geochemical reservoirs (e.g. Day, 2013).

The addition or removal of Re and/or Os post-crystallisation may cause Os isotopes to deviate from their original values in which Os isotope values will plot above the isochron if Re has been lost or Os gained, and below the isochron if Re is gained or Os lost (Barnes and Ripley, 2016). The interaction between rock and low temperature fluids can cause Re loss or Os gain (Barnes and Ripley, 2016). Likewise, the assimilation of crustal materials can also cause Re loss or Os gain, forcing samples to plot above the isochron (Barnes and Ripley, 2016). Due to the similarities that low-temperature alteration and crustal contamination have on Re and Os, careful interpretations

for these sample types should be taken. In Figure 23, NG2 samples are plotted against, and have a good fit along, a 2.06 Ga reference isochron. A good fit with the 2.06 Ga reference isochron is

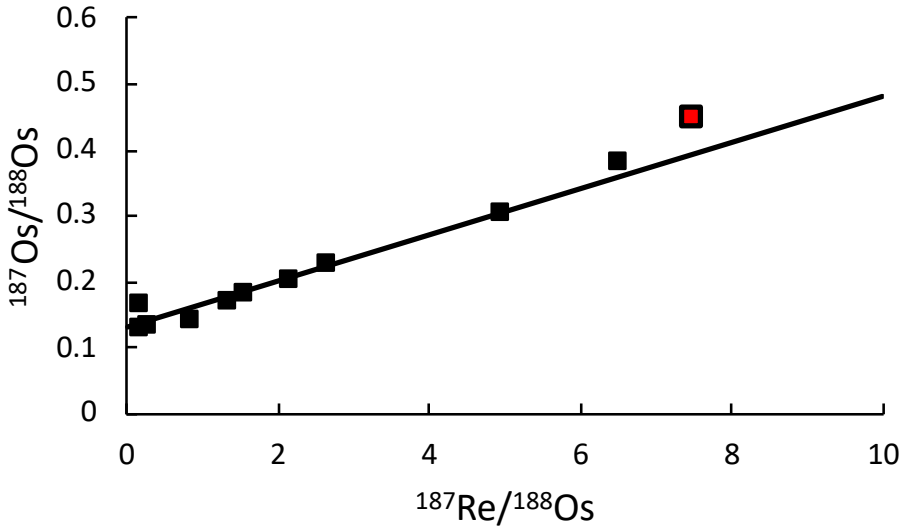

Figure 23. Samples from the NG2 borehole suite plotted against a 2.06 Ga reference isochron. The 2.06 Ga reference isochron slope was determined, and the y-intercept is the average initial 187Os/188Os ratios for the NG2 samples at 2.06 Ga. Most samples fall very close to the reference isochron and provide a good fit. The red square with a black outline is chilled margin sample NG2-773.65.

support for NG2 samples not being extensively altered by low temperature fluids, and that samples plotting above the isochron, i.e. NG2-773.65, NG2-706.53, and NG2-604.5, assimilated more crustal material than samples that plot near, on, or below the isochron. Further, these samples that plot above the isochron have the most radiogenic γOs_i values from the NG2 suite.

6.4 Implications for the mantle source and high $\delta^{18}O$ signature for Lower Zone parent magmas

The generally high $\delta^{18}O$ values for NG2 suite samples ($\delta^{18}O$ = 5.56 – 8.03‰) reflect variable contribution of a crustal component. However, the $\delta^{18}O$ ($\delta^{18}O$ = 5.67‰) value for olivine in sample NG2-734.64 is similar to MORB ($\delta^{18}O$ = 5.70‰) and peridotitic mantle ($\delta^{18}O$ = 5.50‰) (e.g. Eiler, 2001), indicating a mantle origin and little to no crustal component for this sample. Further, the γOs_i value for NG2-734.64 is the lowest in the NG2 suite (γOs = -4.37), and is the only sample reported to date from the Bushveld to contain a negative γOs_i value. However, the standard error values for two NG2 samples and two samples from (Schoenberg et al., 1999)

overlap into negative and unradiogenic γOs_i. The H-SCLM is the only geochemical reservoir to be characterised by unradiogenic γOs_i values due to long-term isolation from the convecting mantle and elevated $^{187}Re/^{188}Os$ (Day, 2013). However, the entire NG2 sample suite, including NG2-734.64, contains negative εNd_i values, which have been previously interpreted as crustal assimilation (e.g. Maier et al., 2000). Yet, negative γOs_i and εNd_i values for sample NG2-734.64 are consistent with an SCLM source (e.g. Pearson et al., 1995b; Pearson et al., 1995a). The negative γOs_i value for NG2-734.64, in combination with a negative εNd_i value and mantle $\delta^{18}O$, is interpreted here to reflect an H-SCLM mantle source rather than crustal assimilation and represents an end-member source component of the Lower Zone parental magma (i.e., little to no crustal component).

In addition to the above geochemical characteristics pointing towards an SCLM source component, strong negative Nb anomalies in primitive mantle normalised diagrams are observed for all samples. These negative anomalies are commonly observed in Karoo flood basalts, for example, and interpreted to reflect a metasomatised SCLM mantle source component (e.g., Jourdan et al., 2007; Harris et al., 2015). Metasomatism of the H-SCLM by slab-derived fluids causes negative Nb anomalies due to the compatibility of Nb in the slab residue, leaving the fluid depleted in Nb (e.g. Brenan et al., 1994; Baier et al., 2008). Thus, the interaction of a Nb-poor fluid with the H-SCLM will cause negative Nb anomalies in the metasomatised H-SCLM. The Nb anomaly (Nb/Nb*) for the NG2 suite can be calculated using the following equation:

$$Nb/Nb^* = \frac{Nb}{\sqrt{Th * La}} \qquad \text{eq. 11}$$

The NG2 suite contains the range Nb/Nb* = 0.08 to 0.19, and these low values represent strong negative Nb anomalies, evidence for a metasomatised SCLM source component. The negative Nb anomalies present in NG2 samples are also present in Karoo high-Ti rocks, in which Nb/Nb* = 0.43 – 0.57 for Karoo high-Ti picrites (Jourdan et al., 2007). Since the NG2 suite and Karoo high-Ti rocks contain these negative Nb anomalies, these LIP's may have sourced the same SCLM

reservoir or a reservoir formed through similar processes. The low Nb/Nb* and εNd_i values throughout the NG2 suite are interpreted as reflecting a primary SCLM source rather than crustal assimilation.

The NG2 suite contains $\delta^{18}O$ values in the range $\delta^{18}O$ = 5.56‰ to 8.03‰, with most $\delta^{18}O$ values > 5.79‰. The range in γOsi values for the NG2 suite is γOs_i = -4.37 to +35.9. This range includes both unradiogenic (e.g. γOs_i = -4.37) and very radiogenic (e.g. γOs_i = +35.9) values. Further, samples NG2-734.64, NG2-377.0, and NG2-197.0 plot within the H-SCLM peridotite xenolith field in Figure 24 (Os concentration vs. $^{187}Os/^{188}Os$). These three samples contain three

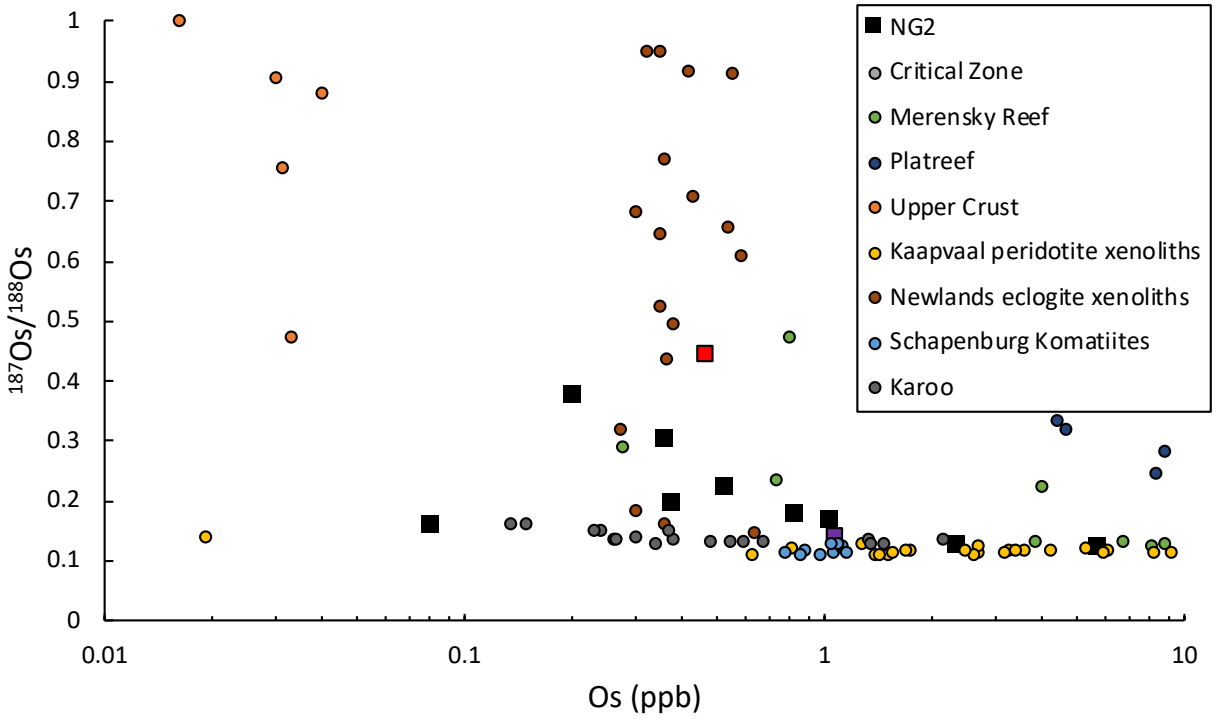

Figure 24. An Os concentration vs $^{187}Os/^{188}Os$ plot including the values for the NG2 borehole suite, Bushveld data, Crust, peridotite xenoliths, eclogite xenoliths, Schapenburg komatiites, and Karoo picrate basalts. Chilled margin sample NG2-773.65 and sample NG2-734.64 are the red and purple squares, respectively. Sample NG2-734.64 has the most unradiogenic γOs_i values from the NG2 borehole suite and has the colour purple to clearly indicate that it plots on top of the komatiite field. Data for the various reservoirs and sample suites come from Ellam et al., 1992; Pearson et al., 1995a; McCandless et al., 1999; Schoenberg et al., 1999; Peucker-Ehrenbrink and Jahn, 2001; Menzies et al., 2003; Puchtel et al., 2009; Reisberg et al., 2011.

of the four lowest γOs_i values in the NG2 suite. The NG2 suite samples trend from the H-SCLM peridotite xenolith field to the eclogite xenolith (E-SCLM) and crust fields, which contain greater $^{187}Os/^{188}Os$ and lower Os concentrations. As the NG2 suite samples trend to more crust-like Os

concentrations and $^{187}Os/^{188}Os$ values, the γOs_i values also increase. There is one outlier, sample NG2-706.53, which contains the lowest Os concentration, and a mantle-like $^{187}Os/^{188}Os$ value. However, this sample contains γOs_i = +35.9, which is the highest for the NG2 suite. The reason why this sample plots away from the other NG2 samples, yet contains mantle Os and $^{187}Os/^{188}Os$ values, cannot be determined, but may have been affected by post-magmatic processes (Figure 24). The range of γOs_i values for the NG2 suite, and the trend observed in Figure 24 are indicative of mixing between an unradiogenic H-SCLM end-member similar to NG2-734.64, and a highly radiogenic crustal component. Two potential crustal components can account for this geochemical signatures: 1) crustal assimilation during ascent of magmas through the crust and/or 2) an enriched mantle source, such as E-SCLM or recycled crust component of a mantle plume.

The crust contains low Nb/Ta ratios, in which the average Nb/Ta ratios for the middle and upper crust are Nb/Ta = 8 and Nb/Ta = 11, respectively, and GLOSS contains Nb/Ta = 14 (Rudnick and Fountain, 1995; Plank and Langmuir, 1998). The Nb/Ta ratios for the middle and upper crust from Rudnick and Fountain (1995) are in general agreement with the range given by Pfänder et al. (2012) for crust (Nb/Ta = 12 – 13). The NG2 suite contains Nb/Ta ratios ranging from Nb/Ta = 10.9 – 15.7, with most samples containing Nb/Ta > 13. The high Nb/Ta ratios, in addition to low Nb/Nb*, for the NG2 sample suite are evidence for partial melting of SCLM, which contains high Nb/Ta ratios (e.g. Pfänder et al., 2012). Interestingly, sample NG2-734.64, which has the second lowest $\delta^{18}O$ and lowest γOs, values in the NG2 suite, also has the lowest Nb/Ta ratio (Nb/Ta = 10.9). Since this sample is interpreted as end-member H-SCLM source, the Nb/Ta ratio should be the highest in the NG2 suite. However, the Nb/Nb* value for NG2-734.64 falls in about the middle for the Lower Zone samples, which is support for an H-SCLM source. Due to this, the Nb/Nb* value may be better at discriminating between crust and SCLM. The lower crust contains a higher Nb/Ta ratio (Nb/Ta = 13) than the middle and upper crust (Rudnick and Fountain, 1995). Larger differences in trace elements between the lower crust and NG2 suite, compared to the NG2 suite with the middle and lower crust, suggests that large amounts of lower crust were not assimilated. Regardless, the Nb/Ta ratios for NG2 suite samples are greater than Nb/Ta = 13 with the exception of two samples (NG2-734.64 and NG2-450.53), evidence for H-SCLM interaction with Lower Zone magmas.

Correlations between $\delta^{18}O$ values and other isotopic systems have the potential to determine if crustal assimilation processes affected the magmas. More specifically, positive correlations of $\delta^{18}O$ with $^{87}Sr/^{86}Sr_i$ and γOs_i, and negative correlations with εNd_i are expected for progressive crustal assimilation. The calculated magmatic $\delta^{18}O$ values for the NG2 suite have been plotted against the other isotopic systems utilised in this study (Table 7; Figures 25 – 27).

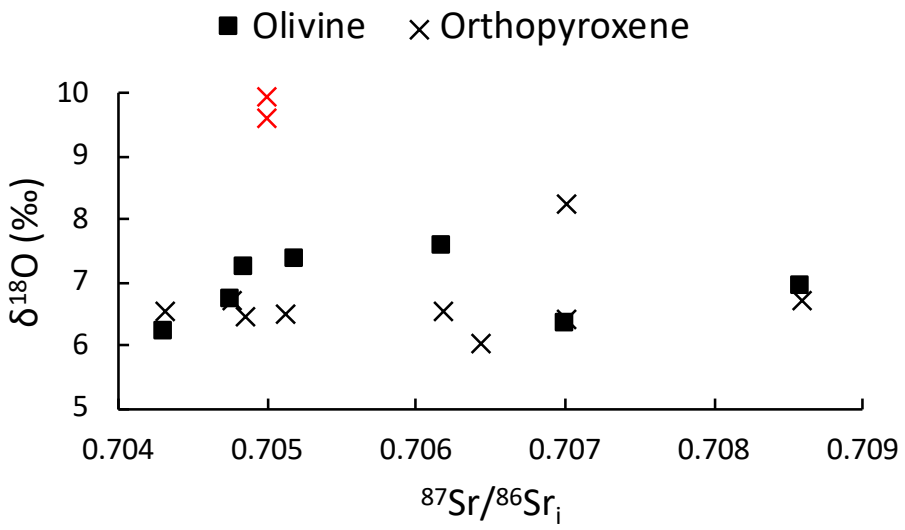

Figure 25. Plot of $^{87}Sr/^{86}Sr_i$ versus calculated magma $\delta^{18}O$ values (Table 7) for olivine and orthopyroxene separates for the NG2 suite and sample NG2-773.65 (red X's)

Despite high $\delta^{18}O$, $^{87}Sr/^{86}Sr_i$, γOs_i, and low εNd_i values, there is no trend in the data suggesting progressive crustal assimilation. Thus, crustal assimilation does not seem likely to account for the high $\delta^{18}O$ values measured in this study (Figures 25 – 27).

Sample NG2-773.65 orthopyroxene separate values plot far away from the NG2 orthopyroxene values in all three figures as it has higher $\delta^{18}O$, εNd_i, and γOs_i values than the NG2 suite (Figures 17, 25 – 27). Chilled margin samples, such as NG2-773.65, are interpreted as being derived from a komatiite magma and assimilating large portions of the crust (20 – 53%) (Wilson, 2012; Maier et al., 2016). Thus, sample NG2-773.65 is interpreted as being representative of crustal assimilation, and demonstrates the isotopic effects of assimilating large portions of the crust.

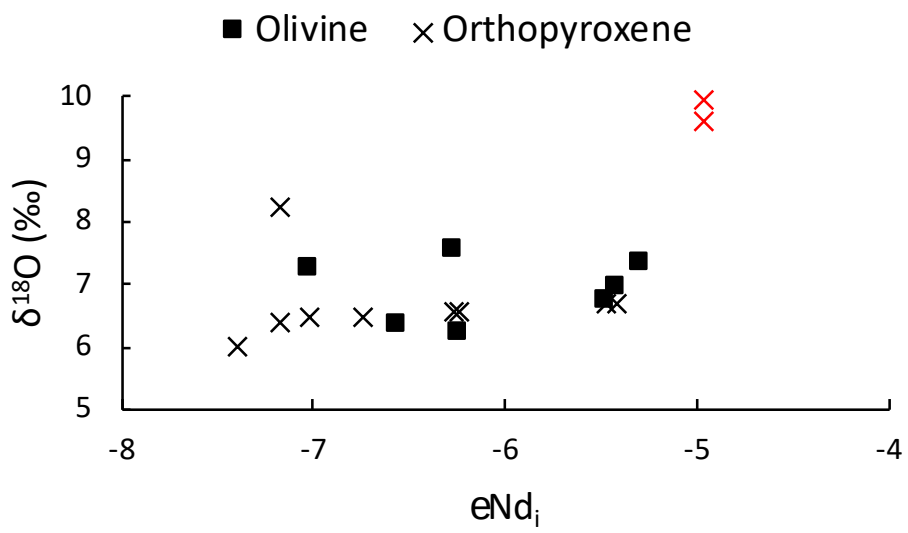

Figure 26. Plot of εNd_i versus calculated magma $\delta^{18}O$ values for olivine and orthopyroxene separates for the NG2 suite and sample NG2-773.65 (red X's).

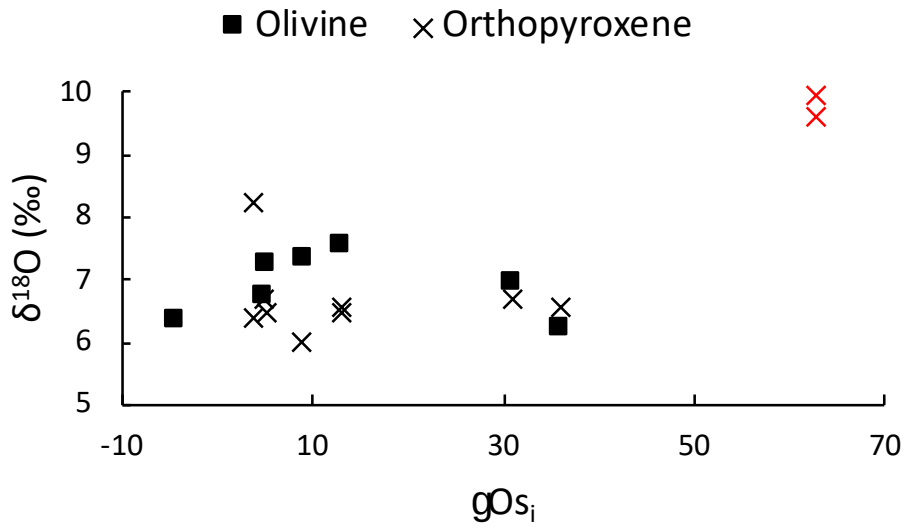

Figure 27. Plot of γOs_i versus calculated magma $\delta^{18}O$ values for olivine and orthopyroxene separates for the NG2 suite and sample NG2-773.65 (red X's).

Samples from the NG2 suite contain similar geochemical compositions to the high-Ti picrites from the Karoo LIP, in which both of these sample suites contain high LILE and LREE compared to HFSE and HREE, respectively, strong negative Nb anomalies, and high $\delta^{18}O$ values (e.g. Harris et al., 2005; Jourdan et al., 2007; Harris et al., 2015). Further, the NG2 suite and high-

Ti Karoo rocks contain similar Sr_i, εNd_i, and γOs_i compositions (e.g. Ellam et al., 1992; Jourdan et al., 2007). In Figure 28, sample NG2-734.64 plots within the SCLM field and most NG2 samples

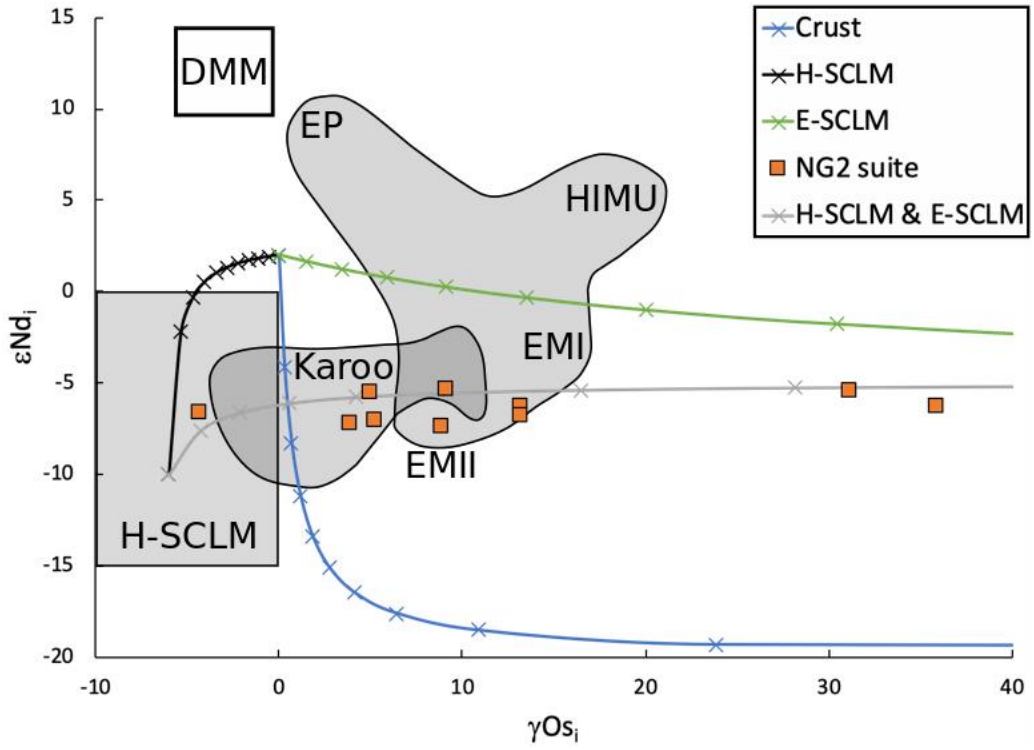

Figure 28. Figure illustrating the relationships between the NG2 sample suite (orange squares) and other mantle reservoirs including the SCLM, Karoo basalts, EMI (enriched mantle I), EMII (enriched mantle II), HIMU (high μ), EP (enriched-plume end member), and DMM (depleted MORB mantle). Calculated mixing model lines are plotted to show the trends for a mantle melt assimilating materials from the Crust (γOs = 540, Os = 0.02 ppb; εNd_i = -20, Nd = 70ppm), H-SCLM (γOs = -6, Os = 3.5 ppb; εNd_i = -10, Nd = 1.2 ppm), or E-SCLM (γOs = 540, Os = 0.1 ppb; εNd_i = -5, Nd = 10 ppm), and a mixing line for H-SCLM and E-SCLM melts. Values for these reservoirs were chosen arbitrarily that resemble values reported in the literature. The crust contains radiogenic γOs_i values that plot to the far right of the figure. Samples NG2-773.65, NG2-706.53, and NG2-689.73 are the most radiogenic γOs_i samples from the NG2 borehole suite. These samples plot to the right of the figure but are not as radiogenic as the crust. Figure is modified from Shirey and Walker (1998) in which the values for the mantle reservoirs come from Zindler and Hart, 1986; Ellam et al., 1992; Carlson and Irving, 1994; Horan et al., 1995; Pearson et al., 1995a; Pearson et al., 1995b; Shirey, 1997; Shirey and Walker, 1998.

overlap with the Karoo picrite field (Ellam et al., 1992). Additionally, the Lower Zone samples follow the mixing trend between H-SCLM and E-SCLM (Figure 28). None of the NG2 samples plotted along the mixing lines for Crust, H-SCLM, and E-SCLM versus a mantle melt (Figure 28). Sample NG2-773.65 (not shown) plots along the same mixing line with γOs = +62.5 and εNd_i = -4.97. A similar trend is observed with the mixing trends of $^{87}Sr/^{86}Sr_i$ versus γOs_i for the crust, H-SCLM, E-SCLM versus a mantle melt, and for H-SCLM versus E-SCLM (Figure 29). However, in this mixing model the Lower Zone samples and NG2-773.65 plot along or between the H-SCLM versus

E-SCLM, and E-SCLM versus mantle melt mixing lines (Figure 29). An exception is sample NG2-734.64, which plots on the H-SCLM versus mantle melt line (Figure 29).

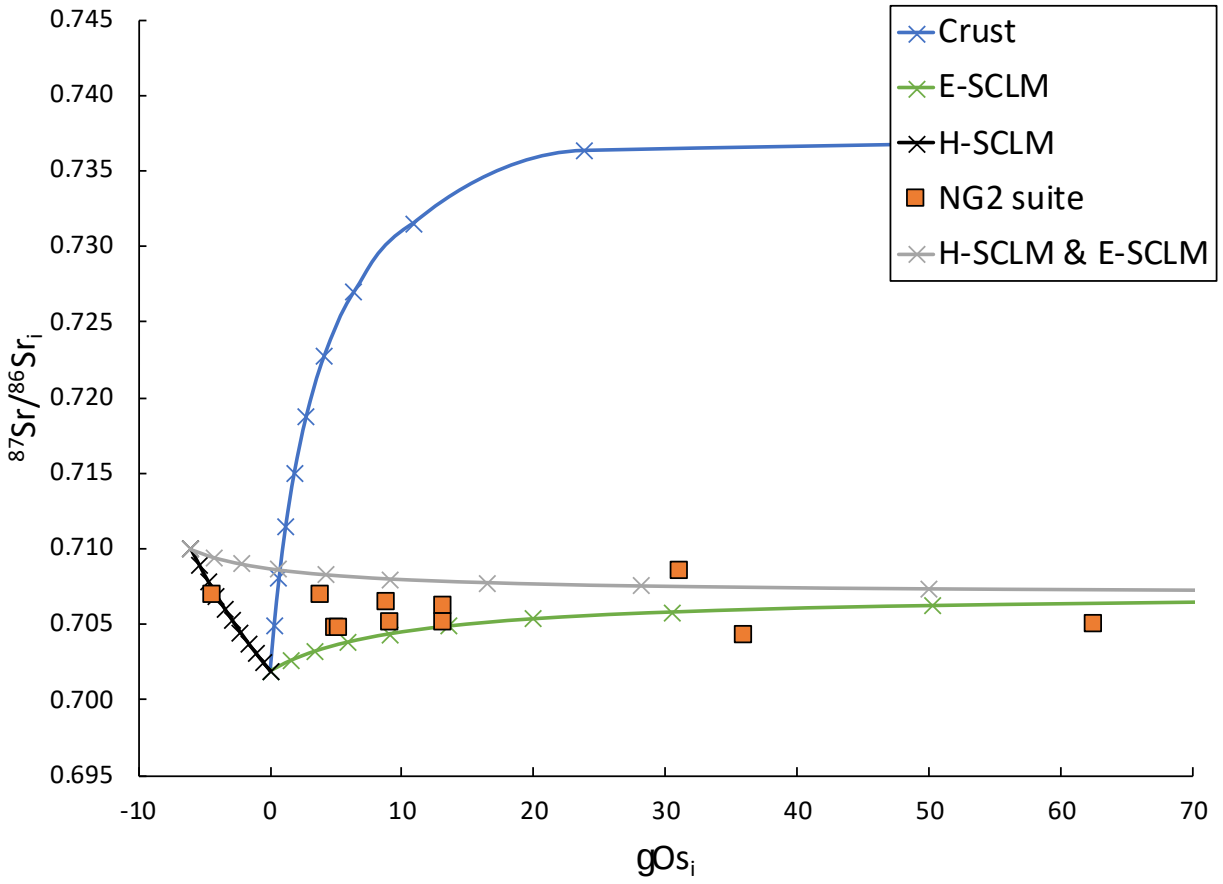

Figure 29. Mixing model for $^{87}Sr/^{86}Sr_i$ versus γOs_i. Mixing lines include Crust ($^{87}Sr/^{86}Sr_i$ = 0.7415, Sr = 290 ppm), E-SCLM ($^{87}Sr/^{86}Sr_i$ = 0.7415, Sr = 290 ppm), and H-SCLM($^{87}Sr/^{86}Sr_i$ = 0.7415, Sr = 290 ppm) versus a mantle melt ($^{87}Sr/^{86}Sr_i$ = 0.7415, Sr = 290 ppm), and the H-SCLM versus E-SCLM. Samples from the NG2 suite are plotted.For γOs and Os (ppb) values for the Crust, H-SCLM, E-SCLM, and mantle melt, see Figure 28.

The addition of significant amounts of crust would yield highly unradiogenic εNd_i and radiogenic $^{87}Sr/^{86}Sr_i$ values (Figures 28 & 29). Instead, Lower Zone samples and NG2-773.65 contain more radiogenic εNd_i and $^{87}Sr/^{86}Sr_i$ values than the crust (Figures 28 & 29). Both the crust and the E-SCLM contain radiogenic γOs_i, whereas the H-SCLM contains unradiogenic γOs_i, and a mantle melt contains slightly radiogenic γOs_i (Figures 28 & 29). All Lower Zone samples plot along the H-SCLM & E-SCLM mixing lines in Figure 28 as well as Figure 29, save sample NG2-734.64. These trends suggest that the Lower Zone principally sourced the H-SCLM and E-SCLM, likely with

a small degree of mantle melt other than the SCLM, as sample NG2-734.64 plots along the H-SCLM and the mantle melt mixing line in Figure 29. Some crustal assimilation may have occurred, especially for samples with the most radiogenic γOs values (i.e. samples NG2-773.65, NG2-706.5, and NG2-604.5). The mixing model of εNd_i versus $^{87}Sr/^{86}Sr_i$ (Figure 30) does not show any meaningful trends as the Lower Zone samples and NG2-773.65 have consistent, unradiogenic, εNd_i values than the mixing lines, which trend from radiogenic to unradiogenic with increasing $^{87}Sr/^{86}Sr_i$ values (Figure 30). This mixing model is also inconsistent with sample NG2-734.64, which contains negative γOs_i, plots within the H-SCLM field (Figure 28), H-SCLM & E-SCLM mixing lines (Figure 28), and on the H-SCLM and mantle melt mixing line (Figure 29), yet plots directly on the lower crust and mantle melt mixing line in Figure 30. In addition to the mixing model correlations for the NG2 suite displayed in Figures 28 & 29, similar εNd_i and γOs_i values and the negative Nb anomalies for the high-Ti Karoo picrites and NG2 suite suggest that the high $\delta^{18}O$ character of these rocks was not the result of crustal assimilation, but rather from a mantle reservoir, such as the E-SCLM (Harris et al., 2015) or an enriched mantle plume that is suggested for the Karoo (e.g. Ellam et al., 1992). The highest γOs_i values for the Karoo picrites fit into the range of OIB γOs_i, which was suggested to indicate that the Karoo sourced a mantle plume and melts from the SCLM (Ellam et al., 1992). Additionally, a mantle plume with a recycled crustal component could explain high Sr_i, high $\delta^{18}O$, and negative εNd_i values for Karoo high-Ti picrites (e.g. Ellam et al., 1992; Hauri and Hart, 1993; Jourdan et al., 2007; Day, 2013; Harris et al., 2015). However, lack of correlations for Sr_i and εNd_i with $\delta^{18}O$ values, high $\delta^{18}O$ values, trace element characteristics, radiogenic isotope compositions, and the depletion of Nb and Ta for Karoo picrites has suggested that the E-SCLM is more likely the source for the crustal characteristics rather than crustal assimilation, or an enriched mantle plume (Harris et al., 2015). The NG2 suite contains similar geochemical characteristics as the high-Ti Karoo picrites, suggesting that the crustal character for the NG2 suite could be from the E-SCLM or an enriched mantle plume.

The author interprets these crustal signatures in the NG2 suite to result from a recycled crustal source in the mantle, such as the E-SCLM or an enriched mantle plume. Additionally, these signatures are unlikely to be related to crustal assimilation processes, with the exception of sample NG2-773.65, which is unrelated to the other Lower Zone samples from the NG2 suite, and

contains the most radiogenic γOs_i (γOs_i = +62.5) and the highest $\delta^{18}O$ values ($\delta^{18}O$ = 9.42‰ & 9.78‰) from NG2 samples analysed in this study.

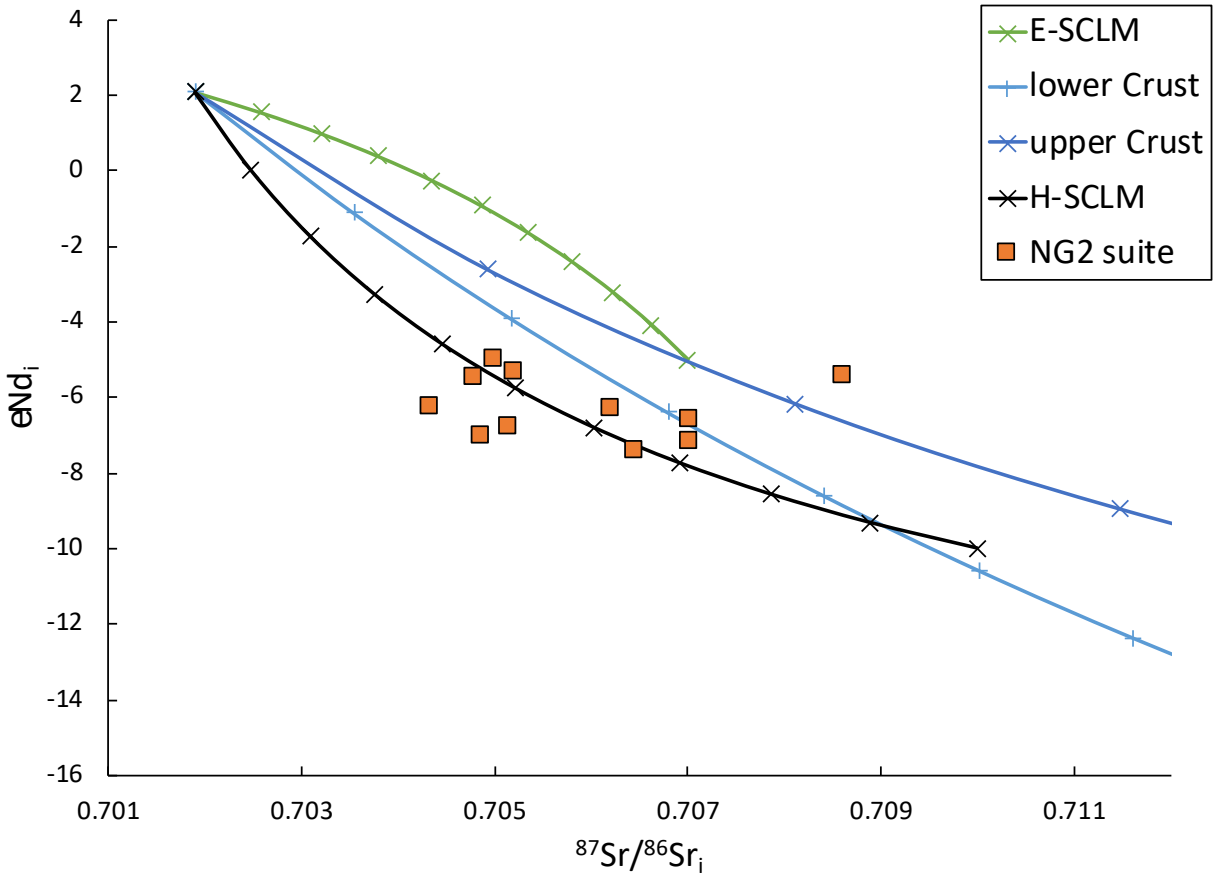

Figure 30. Mixing model of the E-SCLM, lower Crust, upper Crust, and H-SCLM versus a mantle melt, with NG2 samples plotted for εNd_i versus $^{87}Sr/^{86}Sr_i$. For εNd_i, $^{87}Sr/^{86}Sr_i$, Nd (ppm), and Sr (ppm) values, please see Figures 28 & 29.

7. Conclusions

This study investigated the Lower Zone of the Bushveld Complex through samples from the NG2 borehole. The geochemical systems and methods utilised include petrography, point-count analyses, major elements, trace elements, oxygen isotopes, Rb-Sr isotopes, Sm-Nd isotopes, HSE, and Os isotopes. Further, this is the first study on the Lower Zone, which utilised the Re-Os isotope system.

The geochemical data collected for the NG2 sample suite in this study are in agreement with previously collected data for the Lower Zone, and the Bushveld Complex in general, including an enrichment in LILE and LREE over HFSE and HREE, respectively (e.g. Maier et al., 2000; Godel et al., 2011). Further, negative εNd_i and high $\delta^{18}O$ values are present in the NG2 suite samples, as were previously determined for the Lower Zone (e.g. Maier et al., 2000; Harris et al., 2005). The $^{87}Sr/^{86}Sr_i$ values for the NG2 suite are also in agreement with previous studies on the Lower Zone (Kruger, 1994; Maier et al., 2000). As previously mentioned, this is the first study detailing the Re-Os isotope composition of the Lower Zone. This is also the first study to produce a coherent multi-isotope dataset for the Lower Zone. However, the previously reported γOs_i values for the Critical Zone and Platreef overlap with NG2 suite γOs_i values (e.g. McCandless et al., 1999; Schoenberg et al., 1999; Reisberg et al., 2011).

The $\delta^{18}O$ values for the NG2 suite overlap with peridotitic mantle $\delta^{18}O$ values ($\delta^{18}O$ = 5.50‰; Eiler, 2001), but migrate to values much higher than mantle (e.g. $\delta^{18}O$ = 8.03‰). The range in $\delta^{18}O$ values for the NG2 suite are evidence for a crustal source, such as crustal assimilation or sourcing the E-SCLM. However, there are no trends when $\delta^{18}O$ values for the NG2 suite are plotted against $^{87}Sr/^{86}Sr_i$, εNd_i, and γOs_i values. If crustal assimilation had occurred there would likely be direct correlations between $\delta^{18}O$ values and the other isotope systems.

The γOs_i value for NG2-734.64 is the first negative and unradiogenic γOs_i value reported for the Bushveld (γOs_i = -4.37). Additionally, the unradiogenic γOs_i is accompanied by unradiogenic εNd_i, which is ubiquitous for the NG2 suite, and is a primary feature of the parental magma and not crustal assimilation. This value is evidence for the H-SCLM being a mantle source for Lower Zone magmas. However, the NG2 suite contains γOs_i values that range from the unradiogenic value of NG2-734.64 (γOs_i = -4.37) to radiogenic values (e.g. γOs_i = +35.9), reflecting

the sourcing of crustal materials and melts from the H-SCLM. Due to the lack in correlations between isotope systems utilised for the NG2 suite, and that the high-Ti picrites of the Karroo LIP also lack correlations, crustal assimilation is unlikely the cause for the crustal characteristics of the NG2 suite.

Modelling of $^{87}Sr/^{86}Sr_i$, εNd_i, and γOs_i isotopes show that the Lower Zone samples and NG2-773.65 from the NG2 suite plot along the H-SCLM & E-SCLM mixing lines in Figures 28 and 29. An exception is that sample NG2-734.64 plots along the H-SCLM and mantle melt mixing line in Figure 29. These characteristics are support for the Lower Zone magmas primarily sourcing melts from the H-SCLM and E-SCLM, with some input from a primitive mantle melt. The high γOs_i values for samples NG2-773.65, NG2-706.53, and NG2-604.5 could be explained through crustal assimilation, however the $\delta^{18}O$ values for NG2-706.53 ($\delta^{18}O$ = 5.55‰ and 6.32‰) and NG2-604.5 ($\delta^{18}O$ = 6.27‰ and 6.48‰) are not consistent with crustal assimilation. These samples (NG2-706.53 & NG2-604.5) contain $\delta^{18}O$ values that are lower than, or similar to, other samples from the NG2 suite which contain γOs_i < +13.1. Samples NG2-706.53 and NG2-604.5 contain γOs_i = +35.9 and +31.1, respectively. The γOs_i values for these samples is much higher than the corresponding $\delta^{18}O$ values for these samples, which would likely have been much higher if crustal assimilation occurred at a large degree. Thus, the most likely scenario from the data collected and presented here is that the geochemical characteristics reflecting a crustal source are likely a result of Lower Zone magmas sourcing the E-SCLM, or an enriched mantle plume, rather than crustal assimilation. Sample NG2-773.65 is a chilled margin sample that contains the most radiogenic γOs_i (γOs_i = +62.5) and the most elevated $\delta^{18}O$ values ($\delta^{18}O$ = 9.42‰ & 9.78‰) of NG2 borehole samples analysed. This sample is the most likely sample from the NG2 suite to have been affected by crustal assimilation processes.

8. References

Alves S., Alves S., Schiano P., Capmas F. and Allegre C. ~J. (2002) Systematic Osmium Isotope Binary Mixing Arrays in Arc Volcanism. *Earth Planet. Sci. Lett.* **198**, 355–369.

Andrews D. R. A. and Brenan J. M. (2002) The solubility of ruthenium in sulfide liquid: Implications for platinum group mineral stability and sulfide melt-silicate melt partitioning. *Chem. Geol.* **192**, 163–181.

Arndt N. T., Coltice N., Helmstaedt H. and Gregoire M. (2009) Origin of Archean subcontinental lithospheric mantle: Some petrological constraints. *Lithos* **109**, 61–71.

Aulbach S., Mungall J. E. and Pearson D. G. (2016) Distribution and Processing of Highly Siderophile Elements in Cratonic Mantle Lithosphere. *Rev. Mineral. Geochemistry* **81**, 239–304.

Baier J., Audétat A. and Keppler H. (2008) The origin of the negative niobium tantalum anomaly in subduction zone magmas. *Earth Planet. Sci. Lett.* **267**, 290–300.

Barnes S.-J. and Maier W. D. (2002) Platinum-Group Element Distributions in the Rustenburg Layered Suite of the Bushveld Complex , South Africa. In *The geology, geochemistry, mineralogy and mineral beneficiation of the platinum-group elements* pp. 431–458.

Barnes S.-J. and Ripley E. M. (2016) Highly Siderophile and Strongly Chalcophile Elements in Magmatic Ore Deposits. *Rev. Mineral. Geochemistry* **81**, 725–774.

Barnes S. J. (1989) Are Bushveld U-type parent magmas boninites or contaminated komatiites? *Contrib. to Mineral. Petrol.* **101**, 447–457.

Barnes S. J., Maier W. D. and Curl E. A. (2010) Composition of the marginal rocks and sills of the rustenburg layered suite, Bushveld Complex, South Africa: Implications for the formation of the platinum-group element deposits. *Econ. Geol.* **105**, 1491–1511.

Barnes S. J., Pagé P., Prichard H. M., Zientek M. L. and Fisher P. C. (2016) Chalcophile and platinum-group element distribution in the Ultramafic series of the Stillwater Complex, MT, USA—implications for processes enriching chromite layers in Os, Ir, Ru, and Rh. *Miner. Depos.* **51**, 25–47.

Barra F., Ruiz J., Mathur R. and Titley S. (2003) A Re-Os study of sulfide minerals from the Bagdad porphyry Cu-Mo deposit, northern Arizona, USA. *Miner. Depos.* **38**, 585–596.

Becker H., Horan M. F., Walker R. J., Gao S., Lorand J. P. and Rudnick R. L. (2006) Highly siderophile element composition of the Earth's primitive upper mantle: Constraints from new data on peridotite massifs and xenoliths. *Geochim. Cosmochim. Acta* **70**, 4528–4550.

de Beer J. H., Meyer R. and Hattingh P. J. (1987) Geoelectrical and paleomagnetic studies on the Bushveld Complex. In *Proterozoic Lithosphere Evolution* (ed. A. Kröner). pp. 191–204.

Bezard R., Schaefer B. F., Turner S., Davidson J. P. and Selby D. (2015) Lower crustal assimilation in oceanic arcs: Insights from an osmium isotopic study of the Lesser Antilles. *Geochim. Cosmochim. Acta* **150**, 330–344. Available at: http://dx.doi.org/10.1016/j.gca.2014.11.009.

Bindeman I. N., Ponomareva V. V., Bailey J. C. and Valley J. W. (2004) Volcanic arc of Kamchatka: A province with high-δ18O magma sources and large-scale 18O/16O depletion of the upper crust. *Geochim. Cosmochim. Acta* **68**, 841–865.

Birck J. L., Barman M. R. and Campas F. (1997) Re-Os isotopic measurements at the femtomole level in natural samples. *Geostand. Newsl.* **21**, 19–27.

Brandon A. D., Graham D. W., Waight T. and Gautason B. (2007) 186Os and 187Os enrichments and high-3He/4He sources in the Earth's mantle: Evidence from Icelandic picrites. *Geochim. Cosmochim. Acta* **71**, 4570–4591.

Brandon A. D., Humayun M., Puchtel I. S. and Zolensky M. E. (2005) Re-Os isotopic systematics and platinum group element composition of the Tagish Lake carbonaceous chondrite. *Geochim. Cosmochim. Acta* **69**, 1619–1631.

Brandon A. D., Norman M. D., Walker R. J. and Morgan J. W. (1999) 186Os-187Os systematics of Hawaiian picrites. *Earth Planet. Sci. Lett.* **174**, 25–42.

Brandon A. D., Puchtel I. S., Walker R. J., Day J. M. D., Irving A. J. and Taylor L. A. (2012) Evolution of the martian mantle inferred from the 187Re-187Os isotope and highly siderophile element abundance systematics of shergottite meteorites. *Geochim. Cosmochim. Acta* **76**, 206–235. Available at: http://dx.doi.org/10.1016/j.gca.2011.09.047.

Brenan J. M., Bennett N. R. and Zajacz Z. (2016) Experimental Results on Fractionation of the Highly Siderophile Elements (HSE) at Variable Pressures and Temperatures during Planetary and Magmatic Differentiation. *Rev. Mineral. Geochemistry* **81**, 1–87.

Brenan J. M., Finnigan C. F., McDonough W. F. and Homolova V. (2012) Experimental constraints on the partitioning of Ru, Rh, Ir, Pt and Pd between chromite and silicate melt: The importance of ferric iron. *Chem. Geol.* **302**–**303**, 16–32. Available at: http://dx.doi.org/10.1016/j.chemgeo.2011.05.015.

Brenan J. M., Shaw H. F., Phinney D. L. and Ryerson F. J. (1994) Rutile-aqueous fluid partitioning of Nb, Ta, Hf, Zr, U and Th: implications for high field strength element depletions in island-arc basalts. *Earth Planet. Sci. Lett.* **128**, 327–339.

Buchanan P. C., Reimold W. U., Koeberl C. and Kruger F. J. (2004) Rb-Sr and Sm-Nd isotopic compositions of the Rooiberg Group, South Africa: Early Bushveld-related volcanism. *Lithos* **75**, 373–388.

Buchanan P. C., Reimold W. U., Koebert C. and Kruger F. J. (2002) Geochemistry of intermediate to siliceous volcanic rocks of the Rooiberg Group, Bushveld Magmatic Province, South Africa. *Contrib. to Mineral. Petrol.* **144**, 131–143.

Buick I. S., Maas R. and Gibson R. (2001) Precise U–Pb titanite age constraints on the emplacement of the Bushveld Complex, South Africa. *J. Geol. Soc. London.* **158**, 3–6.

Capobianco C. J. and Drake M. J. (1990) Partitioning of ruthenium, rhodium, and palladium between spinel and silicate melt and implications for platinum group element fractionation trends. *Geochim. Cosmochim. Acta* **54**, 869–874.

Capobianco C. J., Hervig R. L. and Drake M. J. (1994) Experiments on crystal/liquid partitioning of Ru, Rh and Pd for magnetite and hematite solid solutions crystallized from silicate melt. *Chem. Geol.* **113**, 23–43.

Carlson R. W. and Irving A. J. (1994) Depletion and enrichment history of subcontinental lithospheric mantle: An Os, Sr, Nd and Pb isotopic study of ultramafic xenoliths from the northwestern Wyoming Craton. *Earth Planet. Sci. Lett.* **126**, 457–472.

Carlson R. W., Pearson D. G., Boyd F. R., Shirey S. B., Irvine G., Menzies A. H. and Gurney J. J. (1999) Re-Os Systematics of Lithospheric Peridotites: Implications for Lithosphere Formation and Preservation. *7th Int. Kimberl. Conf.*, 99–108. Available at: https://www.researchgate.net/publication/284513473_Re-Os_Systematics_of_Lithospheric_Peridotites_Implications_for_Lithosphere_Formation_and_Preservation.

Cawthorn R. G. (1999a) Platinum-group element mineralization in the Bushveld Complex - a critical reassessment of geochemical models. *South African J. Geol.* **102**, 268–281.

Cawthorn R. G. (1999b) Platinum-group element mineralization in the Bushveld Complex - a critical reassessment of geochemical models. *South African J. Geol.* **102**, 268–281.

Cawthorn R. G. (2015) The Bushveld Complex, South Africa. In *Layered Intrusions* (eds. B. Charlier, O. Namur, R. Latypov, and C. Tegner). Springer. pp. 517–588.

Cawthorn R. G. and Walraven F. (1998) Emplacement and Crystallization Time for the Bushveld Complex. *J. Petrol.* **39**, 1669–1687.

Cawthorn R. G. and Webb S. J. (2013) Cooling of the bushveld complex, South Africa: Implications for paleomagnetic reversals. *Geology* **41**, 687–690.

Chazey W. J. and Neal C. R. (2005) Platinum-group element constraints on source composition and magma evolution of the Kerguelen Plateau using basalts from ODP Leg 183. *Geochim. Cosmochim. Acta* **69**, 4685–4701.

Chesley J. T. and Ruiz J. (1998) Crust-mantle interaction in large igneous provinces: Implications from the Re-Os isotope systematics of the Columbia River flood basalts. *Earth Planet. Sci. Lett.* **154**, 1–11.

Class C., Goldstein S. L. and Shirey S. B. (2009) Osmium isotopes in Grande Comore lavas: A new extreme among a spectrum of EM-type mantle endmembers. *Earth Planet. Sci. Lett.* **284**, 219–227.

Cohen A. S. and Waters F. G. (1996) Separation of osmium from geological materials by solvent extraction for analysis by thermal ionisation mass spectrometry. *Anal. Chim. Acta* **332**, 269–275.

Dale C. W., Burton K. W., Pearson D. G., Gannoun A., Alard O., Argles T. W. and Parkinson I. J. (2009) Highly siderophile element behaviour accompanying subduction of oceanic crust: Whole rock and mineral-scale insights from a high-pressure terrain. *Geochim. Cosmochim. Acta* **73**, 1394–1416. Available at: http://dx.doi.org/10.1016/j.gca.2008.11.036.

Davies G. (1980) Parental magma to the Bushveld Complex. *Nature* **287**, 33–35.

Davies G. and Tredoux M. (1985) The platinum-group element and gold contents of the marginal rocks and sills of the Bushveld complex. *Econ. Geol.* **80**, 838–848.

Day J. M. D. (2013) Hotspot volcanism and highly siderophile elements. *Chem. Geol.* **341**, 50–74.

Day J. M. D., Brandon A. D. and Walker R. J. (2016a) Highly Siderophile Elements in Earth, Mars, the Moon, and Asteroids. *Rev. Mineral. Geochemistry* **81**, 161–238.

Day J. M. D. and O'Driscoll B. (2019) Ancient high Pt/Os crustal contaminants can explain radiogenic 186 Os in some intraplate magmas. *Earth Planet. Sci. Lett.* **519**, 101–108. Available at: https://doi.org/10.1016/j.epsl.2019.04.039.

Day J. M. D., Pearson D. G. and Hulbert L. J. (2008) Rhenium - Osmium isotope and platinum-group element constraints on the origin and evolution of the 1.27 Ga muskox layered intrusion. *J. Petrol.* **49**, 1255–1295.

Day J. M. D., Pearson D. G., Macpherson C. G., Lowry D. and Carracedo J. C. (2010a) Evidence for distinct proportions of subducted oceanic crust and lithosphere in HIMU-type mantle beneath El Hierro and La Palma, Canary Islands. *Geochim. Cosmochim. Acta* **74**, 6565–6589. Available at: http://dx.doi.org/10.1016/j.gca.2010.08.021.

Day J. M. D., Pearson D. G., Macpherson C. G., Lowry D. and Carracedo J. C. (2009) Pyroxenite-rich mantle formed by recycled oceanic lithosphere: Oxygen-osmium isotope evidence from Canary Island lavas. *Geology* **37**, 555–558.

Day J. M. D., Pearson D. G. and Taylor L. A. (2007) Highly siderophile element constraints on accretion and differentiation of the Earth-Moon system. *Science (80-.).* **315**, 217–219.

Day J. M. D., Walker R. J., James O. B. and Puchtel I. S. (2010b) Osmium isotope and highly siderophile element systematics of the lunar crust. *Earth Planet. Sci. Lett.* **289**, 595–605. Available at: http://dx.doi.org/10.1016/j.epsl.2009.12.001.

Day J. M. D., Walker R. J. and Warren J. M. (2017) 186Os–187Os and highly siderophile element abundance systematics of the mantle revealed by abyssal peridotites and Os-rich alloys. *Geochim. Cosmochim. Acta* **200**, 232–254. Available at: http://dx.doi.org/10.1016/j.gca.2016.12.013.

Day J. M. D., Waters C. L., Schaefer B. F., Walker R. J. and Turner S. (2016b) Use of Hydrofluoric Acid Desilicification in the Determination of Highly Siderophile Element Abundances and Re-Pt-Os Isotope Systematics in Mafic-Ultramafic Rocks. *Geostand. Geoanalytical Res.* **40**, 49–65.

Debaille V., Trønnes R. G., Brandon A. D., Waight T. E., Graham D. W. and Lee C. T. A. (2009) Primitive off-rift basalts from Iceland and Jan Mayen: Os-isotopic evidence for a mantle source containing enriched subcontinental lithosphere. *Geochim. Cosmochim. Acta* **73**, 3423–3449.

Depaolo D. J. (1981) Trace element and isotopic effects of combined wallrock assimilation and fractional crystallization. *Earth Planet. Sci. Lett.* **53**, 189–202.

Eales H. V. and Cawthorn R. G. (1996) Developments in Petrology: Layered Intrusions. In *Layered Intrusions* (ed. R. G. Cawthorn). Elsevier Science B. V. pp. 181–229.

Eales H. V. and Costin G. (2012) Crustally contaminated komatiite: Primary source of the chromitites and marginal, Lower, and Critical zone magmas in a staging chamber beneath the Bushveld Complex. *Econ. Geol.* **107**, 645–665.

Eiler J. M. (2001) Oxygen Isotope Variations of Basaltic Lavas and Upper Mantle Rocks. In *Reviews in Mineralogy and Geochemistry* pp. 319–364.

Eiler J. M., McInnes B., Valley J. W., Graham C. M. and Stolper E. M. (1998) Oxygen isotope evidence for slab-derived fluids in the sub-arc mantle. *Nature* **393**, 777–781.

Eisele J., Sharma M., Galer S. J. G., Blichert-Toft J., Devey C. W. and Hofmann A. W. (2002) The role of sediment recycling in EM-1 inferred from Os, Pb, Hf, Nd, Sr isotope and trace element systematics of the Pitcairn hotspot. *Earth Planet. Sci. Lett.* **196**, 197–212.

Ellam R. M. (2006) New constraints on the petrogenesis of the Nuanetsi picrite basalts from Pb and Hf isotope data. *Earth Planet. Sci. Lett.* **245**, 153–161.

Ellam R. M., Carlsont R. W. and Shireyt S. B. (1992) Evidence from Re-Os Isotopes for Plume-Lithosphere Mixing in. *Nature* **359**, 718–721.

Ellam R. M. and Cox K. G. (1989) A Proterozoic lithospheric source for Karoo magmatism: evidence from the Nuanetsi picrites. *Earth Planet. Sci. Lett.* **92**, 207–218.

Escrig S., Doucelance R., Moreira M. and Allègre C. J. (2005) Os isotope systematics in Fogo Island: Evidence for lower continental crust

fragments under the Cape Verde Southern Islands. *Chem. Geol.* **219**, 93–113.

Fagereng Å., Harris C., La Grange M. and Stevens G. (2008) Stable isotope study of the Archaean rocks of the Vredefort impact structure, central Kaapvaal Craton, South Africa. *Contrib. to Mineral. Petrol.* **155**, 63–78.

Fonseca R. O. C., Campbell I. H., O'Neill H. S. C. and Allen C. M. (2009) Solubility of Pt in sulphide mattes: Implications for the genesis of PGE-rich horizons in layered intrusions. *Geochim. Cosmochim. Acta* **73**, 5764–5777.

Fonseca R. O. C., Laurenz V., Mallmann G., Luguet A., Hoehne N. and Jochum K. P. (2012) New constraints on the genesis and long-term stability of Os-rich alloys in the Earth's mantle. *Geochim. Cosmochim. Acta* **87**, 227–242.

Gannoun A., Burton K. W., Day J. M. D., Harvey J., Schiano P. and Parkinson I. (2016) Highly Siderophile Element and Os Isotope Systematics of Volcanic Rocks at Divergent and Convergent Plate Boundaries and in Intraplate Settings. *Rev. Mineral. Geochemistry* **81**, 651–724.

Gannoun A., Burton K. W., Parkinson I. J., Alard O., Schiano P. and Thomas L. E. (2007) The scale and origin of the osmium isotope variations in mid-ocean ridge basalts. *Earth Planet. Sci. Lett.* **259**, 541–556.

Glazner A. F. (1994) Foundering of mafic plutons and density stratification of continental crust. *Geology* **22**, 435–438.

Gleißner P. and Becker H. (2017) Formation of Apollo 16 impactites and the composition of late accreted material: Constraints from Os isotopes, highly siderophile elements and sulfur abundances. *Geochim. Cosmochim. Acta* **200**, 1–24.

Godel B., Barnes S. J. and Maier W. D. (2011) Parental magma composition inferred from trace element in cumulus and intercumulus silicate minerals: An example from the Lower and Lower Critical Zones of the Bushveld Complex, South-Africa. *Lithos* **125**, 537–552. Available at: http://dx.doi.org/10.1016/j.lithos.2011.03.010.

Griffin W. L. and O'Reilly S. Y. (2007) Cratonic lithospheric mantle: Is anything subducted? *Episodes* **30**, 43–53.

Günther T., Haase K. M., Junge M., Oberthür T., Woelki D. and Krumm S. (2018) Oxygen isotope and trace element compositions of platiniferous dunite pipes of the Bushveld Complex, South Africa – Signals from a recycled mantle component? *Lithos* **310**–**311**, 332–341.

Hacker B. R. (1996) Eclogite formation and the rheology, buoyancy, seismicity, and H2O content of oceanic crust. In *Subduction: Top to Bottom* (eds. G. E. Bebout, D. W. Scholl, S. H. Kirby, and J. P. Platt). American Geophysical Union. pp. 337–346.

Harger H. S. (1934) An Early Transvaal Geological Map by Carl Mauch. *Trans. Geolical Soc. South Africa* **37**, 1–4. Available at: https://www.geolsoc.org.uk/Plate-Tectonics/Chap4-Plate-Tectonics-of-the-UK/Caledonian-Orogeney.

Harmer R. E., Auret J. M. and Eglington B. M. (1995) Lead isotope variations within the Bushveld complex, Southern Africa: a reconnaissance study. *J. African Earth Sci.* **21**, 595–606.

Harmer R. E. and Farrow D. (1995) An isotopic study on the volcanics of the Rooiberg Group: age implications and a potential exploration tool. *Miner. Depos.* **30**, 188–195.

Harmer R. E. and Sharpe M. R. (1985) Field relations and strontium isotope systematics of the marginal rocks of the eastern Bushveld complex. *Econ. Geol.* **80**, 813–837.

Harney D. M. W., Merkle R. K. W. and Von Gruenewaldt G. (1990) Platinum-group element behavior in the lower part of the Upper Zone, eastern Bushveld Complex - implications for the formation of the main magnetite layer. *Econ. Geol.* **85**, 1777–1789.

Harris C., Pronost J. J. M., Ashwal L. D. and Cawthorn R. G. (2005) Oxygen and hydrogen isotope stratigraphy of the Rustenburg Layered Suite, Bushveld Complex: Constraints on crustal contamination. *J. Petrol.* **46**, 579–601.

Harris C., le Roux P., Cochrane R., Martin L., Duncan A. R., Marsh J. S., le Roex A. P. and Class C. (2015) The oxygen isotope composition of Karoo and Etendeka picrites: High $\delta^{18}O$ mantle or crustal contamination? *Contrib. to Mineral. Petrol.* **170**, 1–24.

Harris C. and Vogeli J. (2010) Oxygen isotope composition of garnet in the Peninsula Granite, Cape Granite Suite, South Africa: Constraints on melting and emplacement mechanisms. *South African J. Geol.* **113**, 401–412.

Hart R. J., Andreoli M. A. G., Tredoux M. and De Wit M. J. (1990) Geochemistry across an exposed section of Archaean crust at Vredefort, South Africa: with implications for mid-crustal discontinuities. *Chem. Geol.* **82**, 21–50.

Hatton C. J. (1995a) Mantle plume origin for the Bushveld and Ventersdorp magmatic provinces. *J. African Earth Sci.* **21**, 571–577.

Hatton C. J. (1995b) The Bushveld Complex, a product of interaction among magmas derived from a mantle plume. *Commun. Geol. Surv. Namibia* **10**, 93–98.

Hatton C. J. and Schweitzer J. K. (1995) Evidence for synchronous extrusive and intrusive Bushveld magmatism The Rooiberg Group of South

Africa is one of the. *J. African Earth Sci.* **21**, 579–594.

Hauri E. H. and Hart S. R. (1993) ReOs isotope systematics of HIMU and EMII oceanic island basalts from the south Pacific Ocean. *Earth Planet. Sci. Lett.* **114**, 353–371.

Heinonen J. S., Luttinen A. V. and Whitehouse M. J. (2018) Enrichment of 18O in the mantle sources of the Antarctic portion of the Karoo large igneous province. *Contrib. to Mineral. Petrol.* **173**, 1–21. Available at: http://dx.doi.org/10.1007/s00410-018-1447-4.

Hickey R. L. and Frey F. A. (1982) Geochemical characteristics of boninite series volcanics: implications for their source. *Geochim. Cosmochim. Acta* **46**, 2099–2115.

Hill M., Barker F., Hunter D. and Knight R. (1996) Geochemical characteristics and origin of the lebowa granite suite, bushveld complex. *Int. Geol. Rev.* **38**, 195–227.

Hofmann A. W. (2003) Sampling mantle heteogeneity through oceanic basalts: isotopes and trace elements. In *Treatise on Geochemistry* (eds. R. W. Carlson, H. D. Holland, and K. K. Turekian). Elsevier-Pergamon, Oxford. pp. 61–101.

Horan M. F., Walker R. J., Fedorenko V. A. and Czamanske G. K. (1995) Osmium and neodymium isotopic constraints on the temporal and spatial evolution of Siberian flood basalt sources. *Geochim. Cosmochim. Acta* **59**, 5159–5168.

Ireland T. J., Walker R. J. and Garcia M. O. (2009) Highly siderophile element and 187Os isotope systematics of Hawaiian picrites: Implications for parental melt composition and source heterogeneity. *Chem. Geol.* **260**, 112–128. Available at: http://dx.doi.org/10.1016/j.chemgeo.2008.12.009.

Irvine T. N. and Sharpe M. R. (1982) Source-rock compositions and depths of origin of Bushveld and Stillwater magmas. *Carnegie Inst. Washingt. Yearb.* **81**, 294–303.

Jackson M. G. and Shirey S. B. (2011) Re-Os isotope systematics in Samoan shield lavas and the use of Os-isotopes in olivine phenocrysts to determine primary magmatic compositions. *Earth Planet. Sci. Lett.* **312**, 91–101.

Jacob D. E., Schmickler B. and Schulze D. J. (2003) Trace element geochemistry of coesite-bearing eclogites from the Roberts Victor kimberlite, Kaapvaal craton. *Lithos* **71**, 337–351.

Janney P. E., Shirey S. B., Carlson R. W., Pearson D. G., Bell D. R., Le Roex A. P., Ishikawa A., Nixon P. H. and Boyd F. R. (2010) Age, composition and thermal characteristics of South African off-craton mantle lithosphere: Evidence for a multi-stage history. *J. Petrol.* **51**, 1849–1890.

Jourdan F., Bertrand H., Schärer U., Blichert-Toft J., Féraud G. and Kampunzu A. B. (2007) Major and trace element and Sr, Nd, Hf, and Pb isotope compositions of the Karoo large igneous province, Botswana - Zimbabwe: Lithosphere vs Mantle Plume Contribution. *J. Petrol.* **48**, 1043–1077.

Kinnaird J. A. (2005) May 2005 LIP of the Month: The Bushveld Large Igneous Complex. *The Bushveld Large Igneous Complex*, 1–39. Available at: http://www.largeigneousprovinces.org/sites/default/files/BushveldLIP.pdf.

Kleemann G. J. and Twist D. (1989) The compositionally-zoned sheet-like granite pluton of the bushveld complex: Evidence bearing on the nature of a-type magmatism. *J. Petrol.* **30**, 1383–1414.

Kruger F. J. (1994) The Sr-isotopic stratigraphy of the western Bushveld Complex. *South African J. Geol.* **97**, 393–398.

Kruger F. J. and Marsh J. S. (1982) Significance of $^{87}Sr/^{86}Sr$ ratios in the Merensky cyclic unit of the Bushveld Complex. *Nature* **298**, 53–55.

Lambert D. D., Walker R. J., Morgan J. W., Shirey S. B., Carlson R. W., Zientek M. L., Lipin B. R., Koski M. S. and Cooper R. L. (1994) Re - Os and Sm - Nd isotope geochemistry of the stillwater complex, montana: Implications for the petrogenesis of the J-M Reef. *J. Petrol.* **35**, 1717–1753.

Lana C., Gibson R. L., Kisters A. F. M. and Reimold W. U. (2003) Archean crustal structure of the Kaapvaal craton, South Africa - evidence from the Vredefort dome. *Earth Planet. Sci. Lett.* **206**, 133–144.

Lassiter J. C., Blichert-Toft J., Hauri E. H. and Barsczus H. G. (2003) Isotope and trace element variations in lavas from Raivavae and Rapa, Cook-Austral islands: Constraints on the nature of HIMU- and EM-mantle and the origin of mid-plate volcanism in French Polynesia. *Chem. Geol.* **202**, 115–138.

Lassiter J. C. and Hauri E. H. (1998) Osmium-isotope variations in Hawaiian lavas: Evidence for recycled oceanic lithosphere in the Hawaiian plume. *Earth Planet. Sci. Lett.* **164**, 483–496.

Latypov R., Costin G., Chistyakova S., Hunt E. J., Mukherjee R. and Naldrett T. (2018) Platinum-bearing chromite layers are caused by pressure

reduction during magma ascent /704/2151/209 /704/2151/431 /147 article. *Nat. Commun.* **9**, 1–7. Available at: http://dx.doi.org/10.1038/s41467-017-02773-w.

Lee C. A. and Butcher A. R. (1990) Cyclicity in the Sr isotope stratigraphy through the Merensky and Bastard Reef units, Atok section, eastern Bushveld Complex. *Econ. Geol.* **85**, 877–883.

Lee C. A. and Parry S. J. (1988) Platinum-group element geochemistry of the ower and middle group chromitites of the eastern Bushveld Complex. *Econ. Geol.* **83**, 1127–1139.

Lee C. A. and Tredoux M. (1986) Platinum group abundances in the Lower and lower Critical Zones of the Eastern Bushveld Complex. *Econ. Geol.* **81**, 1087–1095.

Lenhardt N. and Eriksson P. G. (2012) Volcanism of the Palaeoproterozoic Bushveld Large Igneous Province: The Rooiberg Group, Kaapvaal Craton, South Africa. *Precambrian Res.* **214–215**, 82–94. Available at: http://dx.doi.org/10.1016/j.precamres.2011.12.003.

Liu C. Z., Wu F. Y., Chung S. L., Li Q. L., Sun W. D. and Ji W. Q. (2014) A "hidden" 18 O-enriched reservoir in the sub-arc mantle. *Sci. Rep.* **4**, 1–6.

MacCaskie D. R. (1983) Differentiation of the Nebo Granite (main Bushveld granite), South Africa. University of Oregon.

MacGregor I. D. and Manton W. I. (1986) Roberts victor eclogites: Ancient oceanic crust. *J. Geophys. Res.* **91**, 14063–14079.

Maier W. D., Arndt N. T. and Curl E. A. (2000) Progressive crustal contamination of the Bushveld Complex: Evidence from ND isotopic analyses of the cumulate rocks. *Contrib. to Mineral. Petrol.* **140**, 316–327.

Maier W. D. and Barnes S. J. (1998) Concentrations of rare earth elements in silicate rocks of the Lower, Critical and Main Zones of the Bushveld Complex. *Chem. Geol.* **150**, 85–103.

Maier W. D. and Barnes S. J. (1999) Platinum-group elements in silicate rocks of the Lower, Critical and Main Zones at union section, Western Bushveld Complex. *J. Petrol.* **40**, 1647–1671.

Maier W. D. and Barnes S. J. (2004) Pt/Pd and Pd/Ir ratios in mantle-derived magmas: A possible role for mantle metasomatism. *South African J. Geol.* **107**, 333–340.

Maier W. D., Barnes S. J. and Karykowski B. T. (2016) A chilled margin of komatiite and Mg-rich basaltic andesite in the western Bushveld Complex, South Africa. *Contrib. to Mineral. Petrol.* **171**, 1–22.

Malitch K. N. and Latypov R. M. (2011) Re-Os and S isotope constraints on timing and source heterogeneity of PGE-Cu-Ni sulfide ores: A case study at the Talnakh ORE junction, Noril'sk Province, Russia. *Can. Mineral.* **49**, 1653–1677.

Marcantonio F., Zindler A., Elliott T. and Staudigel H. (1995) recycled crust in the mantle source of HIMU ocean islands. *Earth Planet. Sci. Lett.* **133**, 397–410.

Mattey D., Lowry D. and Macpherson C. (1994) Oxygen isotope composition of mantle peridotite. *Earth Planet. Sci. Lett.* **128**, 231–241.

McCandless T. E. and Ruiz J. (1991) Osmium isotopes and crustal sources for platinum-group mineralization in the Bushveld Complex, South Africa. *Geology* **19**, 1225–1228.

McCandless T. E., Ruiz J., Adair B. I. and Freydier C. (1999) Re-Os isotope and Pd/Ru variations in chromitites from the Critical Zone, Bushveld Complex, South Africa. *Geochim. Cosmochim. Acta* **63**, 911–923.

McDonald I. and Viljoen K. S. (2006) Platinum-group element geochemistry of mantle eclogites: A reconnaissance study of xenoliths from the Orapa kimberlite, Botswana. *Appl. Earth Sci.* **115**, 81–93.

McDonough W. F. and Sun S. s. (1995) The composition of the Earth. *Chem. Geol.* **120**, 223–253.

Meisel T. and Horan M. F. (2016) Analytical methods for the highly siderophile elements. *Rev. Mineral. Geochemistry* **81**, 89–106.

Meisel T., Walker R. J., Irving A. J. and Lorand J. P. (2001) Osmium isotopic compositions of mantle xenoliths: A global perspective. *Geochim. Cosmochim. Acta* **65**, 1311–1323.

Menzies A. H., Carlson R. W., Shirey S. B. and Gurney J. J. (2003) Re–Os systematics of diamond-bearing eclogites from the Newlands kimberlite. *Lithos* **71**, 323–336.

Molyneux T. G. and Klinkert P. S. (1978) A structural interpretation of part of the eastern mafic lobe of the Bushveld Complex and its surrounds. *Trans. Geol. Soc. South Africa* **81**, 359–368.

Morgan J. W., Walker R. J., Horan M. F., Beary E. S. and Naldrett A. J. (2002) Pt – 186 Os and Re – 187 Os systematics of the Sudbury Igneous Complex , Ontario. *Geochim. Cosmochim. Acta* **66**, 273–290.

Mungall J. and Brenan J. (2014) Partitioning of platinum-group elements and Au between sulfide liquid and basalt and the origins of mantle-crust fractionation of the chalcophile elements. *Geochim. Cosmochim. Acta* **125**, 265–289. Available at: http://dx.doi.org/10.1016/j.gca.2013.10.002.

Mungall J. E., Kamo S. L. and Mcquade S. (2016) U-Pb geochronology documents out-of-sequence emplacement of ultramafic layers in the Bushveld Igneous Complex of South Africa. *Nat. Commun.* **7**, 1–13. Available at: http://dx.doi.org/10.1038/ncomms13385.

Olsson J. R., Söderlund U., Hamilton M. A., Klausen M. B. and Helffrich G. R. (2011) A late Archaean radiating dyke swarm as possible clue to the origin of the Bushveld Complex. *Nat. Geosci.* **4**, 865–869. Available at: http://dx.doi.org/10.1038/ngeo1308.

Olsson J. R., Söderlund U., Klausen M. B. and Ernst R. E. (2010) U-Pb baddeleyite ages linking major Archean dyke swarms to volcanic-rift forming events in the Kaapvaal craton (South Africa), and a precise age for the Bushveld Complex. *Precambrian Res.* **183**, 490–500. Available at: http://dx.doi.org/10.1016/j.precamres.2010.07.009.

Pearson D. G., Carlson R. W., Shirey S. B., Boyd F. R. and Nixon P. H. (1995a) Stabilisation of Archaean lithospheric mantle: A Re-Os isotope study of peridotite xenoliths from the Kaapvaal craton. *Earth Planet. Sci. Lett.* **134**, 341–357.

Pearson D. G., Irvine G. J., Ionov D. A., Boyd F. R. and Dreibus G. E. (2004) Re-Os isotope systematics and platinum group element fractionation during mantle melt extraction: A study of massif and xenolith peridotite suites. *Chem. Geol.* **208**, 29–59.

Pearson D. G., Shirey S. B., Carlson R. W., Boyd F. R., Pokhilenko N. P. and Shimizu N. (1995b) Re-Os, Sm-Nd, and Rb-Sr isotope evidence for thick Archaean lithospheric mantle beneath the Siberian craton modified by multistage metasomatism. *Geochim. Cosmochim. Acta* **59**, 959–977.

Pegram W. J. and Allègre C. J. (1992) Osmium isotopic compositions from oceanic basalts. *Earth Planet. Sci. Lett.* **111**, 59–68.

Peucker-Ehrenbrink B. and Jahn B. (2001) The Upper Continental Crust. *Geochemistry, Geophys. Geosystems* **2**, 1–22.

Pfänder J. A., Jung S., Münker C., Stracke A. and Mezger K. (2012) A possible high Nb/Ta reservoir in the continental lithospheric mantle and consequences on the global Nb budget - Evidence from continental basalts from Central Germany. *Geochim. Cosmochim. Acta* **77**, 232–251.

Pin C., Gannoun A. and Dupont A. (2014) Rapid, simultaneous separation of Sr, Pb, and Nd by extraction chromatography prior to isotope ratios determination by TIMS and MC-ICP-MS. *J. Anal. At. Spectrom.* **29**, 1858–1870.

Plank T. and Langmuir C. H. (1998) The chemical composition of subducting sediment and its consequences for the crust and mantle. *Chem. Geol.* **145**, 325–394.

Prevec S. A., Ashwal L. D. and Mkaza M. S. (2005) Mineral disequilibrium in the Merensky Reef, western Bushveld Complex, South Africa: New Sm-Nd isotopic evidence. *Contrib. to Mineral. Petrol.* **149**, 306–315.

Puchtel I. S., Walker R. J., Anhaeusser C. R. and Gruau G. (2009) Re-Os isotope systematics and HSE abundances of the 3.5 Ga Schapenburg komatiites, South Africa: Hydrous melting or prolonged survival of primordial heterogeneities in the mantle? *Chem. Geol.* **262**, 355–369. Available at: http://dx.doi.org/10.1016/j.chemgeo.2009.02.006.

Radu I. B., Harris C., Moine B. N., Costin G. and Cottin J. Y. (2019) Subduction relics in the subcontinental lithospheric mantle evidence from variation in the δ 18 O value of eclogite xenoliths from the Kaapvaal craton. *Contrib. to Mineral. Petrol.* **174**. Available at: http://dx.doi.org/10.1007/s00410-019-1552-z.

Rajesh H. M., Chisonga B. C., Shindo K., Beukes N. J. and Armstrong R. A. (2013) Petrographic, geochemical and SHRIMP U-Pb titanite age characterization of the Thabazimbi mafic sills: Extended time frame and a unifying petrogenetic model for the Bushveld Large Igneous Province. *Precambrian Res.* **230**, 79–102. Available at: http://dx.doi.org/10.1016/j.precamres.2013.02.002.

Reid D. L., Cawthorn R. G., Kruger F. J. and Tredoux M. (1993) Isotope and trace-element patterns below the Merensky Reef, Bushveld Complex, South Africa: evidence for fluids? *Chem. Geol.* **106**, 171–186.

Reisberg L., Tredoux M., Harris C., Coftier A. and Chaumba J. (2011) Re and Os distribution and Os isotope composition of the Platreef at the Sandsloot-Mogolakwena mine, Bushveld complex, South Africa. *Chem. Geol.* **281**, 352–363. Available at: http://dx.doi.org/10.1016/j.chemgeo.2010.12.021.

Reisberg L., Zindler A., Marcantonio F., White W., Wyman D. and Weaver B. (1993) Os isotope systematics in ocean island basalts. *Earth Planet. Sci. Lett.* **120**, 149–167.

Richardson S. H., Pöml P. F., Shirey S. B. and Harris J. W. (2009) Age and origin of peridotitic diamonds from Venetia, Limpopo Belt, Kaapvaal-Zimbabwe craton. *Lithos* **112**, 785–792. Available at: http://dx.doi.org/10.1016/j.lithos.2009.05.017.

Richardson S. H. and Shirey S. B. (2008) Continental mantle signature of Bushveld magmas and coeval diamonds. *Nature* **453**, 910–913.

Riches A. J. V., Ickert R. B., Pearson D. G., Stern R. A., Jackson S. E., Ishikawa A., Kjarsgaard B. A. and Gurney J. J. (2016) In situ oxygen-isotope, major-, and trace-element constraints on the metasomatic modification and crustal origin of a diamondiferous eclogite from Roberts Victor, Kaapvaal Craton. *Geochim. Cosmochim. Acta* **174**, 345–359.

Righter K., Campbell A. J., Humayun M. and Hervig R. L. (2004) Partitioning of Ru, Rh, Pd, Re, Ir, and Au between Cr-bearing spinel, olivine, pyroxene and silicate melts. *Geochim. Cosmochim. Acta* **68**, 867–880.

Robb S. J. and Mungall J. E. (2020) Testing emplacement models for the Rustenburg Layered Suite of the Bushveld Complex with numerical heat flow models and plagioclase geospeedometry. *Earth Planet. Sci. Lett.* **534**, 116084. Available at: https://doi.org/10.1016/j.epsl.2020.116084.

Roy-Barman M. and Allègre C. J. (1995) 187Os/186Os in oceanic island basalts: tracing oceanic crust recycling in the mantle. *Earth Planet. Sci. Lett.* **129**, 145–161.

Rudnick R. L. and Fountain D. M. (1995) Nature and composition of the continental crust : A lower crustal perspective. *Rev. Geophys.* **33**, 267–309. Available at: http://linkinghub.elsevier.com/retrieve/pii/S0031920104001657.

Saal A. E., Rudnick R. L., Ravizza G. E. and Hart S. R. (1998) Re-Os isotopic evidence for the composition, formation and age of the lower continental crust. *Nature* **393**, 1–4.

Sawkins F. J. (1984) *Metal Deposits in Relation to Plate Tectonics*. 1st ed. eds. P. J. Wyllie, A. El Goresy, and W. von Engelhardt, Springer-Verlag, Berlin.

Schaefer B. F., Turner S., Parkinson I., Rogers N. and Hawkesworth C. (2002) Evidence for recycled Archaean oceanic mantle lithosphere in the Azores plume. *Nature* **420**, 304–307.

Schiano P., Burton K. W., Dupré B., Birck J. L., Guille G. and Allègre C. J. (2001) Correlated Os-Pb-Nd-Sr isotopes in the Austral-cook chain basalts: The nature of mantle components in plume sources. *Earth Planet. Sci. Lett.* **186**, 527–537.

Schoenberg R., Kruger F. J., Nägler T. F., Meisel T. and Kramers J. D. (1999) PGE enrichment in chromitite layers and the Merensky Reef of the western Bushveld Complex; a Re-Os and Rb-Sr isotope study. *Earth Planet. Sci. Lett.* **172**, 49–64.

Schoenberg R., Nägler T. F., Gnos E., Kramers J. D. and Kamber B. S. (2003) The Source of the Great Dyke, Zimbabwe, and Its Tectonic Significance: Evidence from Re-Os Isotopes. *J. Geol.* **111**, 565–578.

Schulze D. J., Valley J. W. and Spicuzza M. J. (2000) Coesite eclogites from the Roberts Victor kimberlite, South Africa. *Lithos* **54**, 23–32.

Schweitzer J. K., Hatton C. J. and De Waal S. A. (1997) Link between the granitic and volcanic rocks of the Bushveld Complex, South Africa. *J. African Earth Sci.* **24**, 95–104.

Schweitzer J. K., Hatton C. J. and De Waal S. A. (1995) Regional lithochemical stratigraphy of the Rooiberg Group, upper Transvaal Supergroup: a proposed new subdivision. *South African J. Geol.* **98**, 245–255.

Scoates J. S. and Friedman R. M. (2008) Precise age of the platiniferous Merensky Reef, Bushveld Complex, South Africa, by the U-Pb zircon chemical abrasion ID-TIMS technique. *Econ. Geol.* **103**, 465–471.

Sen I. S., Bizimis M., Sen G. and Huang S. (2011) A radiogenic Os component in the oceanic lithosphere? Constraints from Hawaiian pyroxenite xenoliths. *Geochim. Cosmochim. Acta* **75**, 4899–4916. Available at: http://dx.doi.org/10.1016/j.gca.2011.06.008.

Sharpe M. R. (1981) The chronology of magma influxes to the eastern compartment of the Bushveld Complex as exemplified by its marginal border groups. *J. Geol. Soc. London.* **138**, 307–326.

Sharpe M. R., Bahat D. and Von Gruenewaldt G. (1981) The concentric elliptical structure of feeder sites to the Bushveld Complex and possible economic implications. *Trans. - Geol. Soc. South Africa* **84**, 239–244.

Sharpe M. R. and Hulbert L. J. (1985) Ultramafic sills beneath the eastern Bushveld complex: mobilized suspensions of early lower zone cumulates in a parental magma with boninitic affinities. *Econ. Geol.* **80**, 849–871.

Shirey B., Carlson R. W., Richardson H., Menzies A., Gurney J., Pearson D. G. and Harris J. W. (2001) Archean emplacement of eclogitic components into the lithospheric mantle during formation of the Kaapvaal Craton. *Geophys. Res. Lett.* **28**, 2509–2512.

Shirey S. B. (1997) Re-Os isotopic compositions of Midcontinent rift system picrites: implications for plume-lithosphere interaction and enriched mantle sources. *Can. J. Earth Sci.* **34**, 489–503.

Shirey S. B. and Walker R. J. (1998) The Re-Os Isotope System in Cosmochemistry and High-Temperature Geochemistry. *Annu. Rev. Earth Planet. Sci.* **26**, 423–500.

Shu Q., Brey G. P., Pearson D. G., Liu J., Gibson S. A. and Becker H. (2019) The evolution of the Kaapvaal craton: A multi-isotopic perspective from lithospheric peridotites from Finsch diamond mine. *Precambrian Res.* **331**, 105380. Available at: https://doi.org/10.1016/j.precamres.2019.105380.

Simmons C. E. and Hanson G. N. (1978) Geochemistry and origin of massif-type anorthosites. *Contrib. to Mineral. Petrol.* **66**, 119–135.

Smoliar M., Walker R. J. and Morgan J. W. (1996) Re-Os Ages of Group IIA , IIIA , IVA , and IVB Iron Meteorites Author (s): Michael I . Smoliar , Richard J . Walker , John W . Morgan Published by : American Association for the Advancement of Science Stable URL : http://www.jstor.org/stable/2889840. *Science (80-.).* **271**, 1099–1102.

Snow J. E., Schmidt G. and Rampone E. (2000) Os isotopes and highly siderophile elements (HSE) in the Ligurian ophiolites, Italy. *Earth Planet. Sci. Lett.* **175**, 119–132.

Sparks R. S. J. (1986) The role of crustal contamination in magma evolution through geological time. *Earth Planet. Sci. Lett.* **78**, 211–223.

Stein H. J., Markey R. J. and Morgan J. W. (1997) and Accurate Ages for Molybdenite from the East Qinling Molybdenum Belt, Shaanxi Province, China. *Econ. Geol.* **92**, 827–835.

Tanaka T., Togashi S., Kamioka H., Amakawa H., Kagami H., Hamamoto T., Yuhara M., Orihashi Y., Yoneda S., Shimizu H., Kunimaru T., Takahashi K., Yanagi T., Nakano T., Fujimaki H., Shinjo R., Asahara Y., Tanimizu M. and Dragusanu C. (2000) JNdi-1: A neodymium isotopic reference in consistency with LaJolla neodymium. *Chem. Geol.* **168**, 279–281.

Taylor S. R., Campbell I. H., McCulloch M. T. and McLennan S. M. (1984) A lower crustal origin for massif-type anorthosites. *Nature* **311**, 372–374.

Teigler B. (1990) Mineralogy, petrology and geochemistry of the Lower and lower Critical Zones, northwestern Bushveld Complex. Rhodes University, Grahamstown, South Africa.

Twist D. (1985) Geochemical evolution of the Rooiberg silicic lavas in the Loskop Dam area, southeastern Bushveld. *Econ. Geol.* **80**, 1153–1165.

Twist D. and French B. M. (1983) Voluminous acid volcanism in the Bushveld Complex: A review of the Rooiberg felsite. *Bull. Volcanol.* **46**, 225–242.

Vermaak C. F. (1995) Platinum-group metals: a global perspective. *Mintek*.

Wager L. R. and Brown G. M. (1968) *Layered Igneous Rocks*. 1st ed., Oliver and Boyd LTD, Edinburgh.

Walker R. J., Morgan J. W., Horan M. F., Czamanske G. K., Krogstad E. J., Fedorenko V. A. and Kunilov V. E. (1994) Re-Os isotopic evidence for an enriched-mantle source for the Noril'sk-type, ore-bearing intrusions, Siberia. *Geochim. Cosmochim. Acta* **58**, 4179–4197.

Walker R. J., Morgan J. W., Naldrett A. J., Li C. and Fassett J. D. (1991) Re-Os isotope evidence for a major crustal component in Ni-Cu sulfide ores, Sudbury igneous complex, Ontario. *Earth Planet. Sci. Lett.* **105**, 416–429.

Walraven F. (1997) Geochronology of the Rooiberg Group, Transvaal Supergroup, South Africa. *Econ. Geol. Res. Unit Inf. Circ. (University Witwatersrand)* **316**.

Walraven F. and Hattingh P. J. (1993) Geochronology of the Nebo Granite, Bushveld Complex. *South African J. Geol.* **96**, 31–41.

White W. M. (2010) Oceanic Island Basalts and Mantle Plumes: The Geochemical Perspective. *Annu. Rev. Earth Planet. Sci.* **38**, 133–160.

Widom E., Hoernle K. A., Shirey S. B. and Schmincke H. U. (1999) Os isotope systematics in the Canary Islands and Madeira: Lithospheric contamination and mantle plume signatures. *J. Petrol.* **40**, 279–296.

Widom E. and Shirey S. B. (1996) Os isotope systematics in the Azores: Implications for mantle plume sources. *Earth Planet. Sci. Lett.* **142**, 451–465.

Wiggers de Vries D. F., Pearson D. G., Bulanova G. P., Smelov A. P., Pavlushin A. D. and Davies G. R. (2013) Re-Os dating of sulphide inclusions zonally distributed in single Yakutian diamonds: Evidence for multiple episodes of Proterozoic formation and protracted timescales of diamond growth. *Geochim. Cosmochim. Acta* **120**, 363–394. Available at: http://dx.doi.org/10.1016/j.gca.2013.06.035.

Willemse J. (1969) The geology of the Bushveld Igneous Complex, the largest repository of magmatic ore deposits in the world. *Econ. Geol.*

Monogr. **4**, 137–208.

Wilson A. H. (2012) A chill sequence to the bushveld complex: Insight into the first stage of emplacement and implications for the parental magmas. *J. Petrol.* **53**, 1123–1168.

Workman R. K., Hart S. R., Jackson M., Regelous M., Farley K. A., Blusztajn J., Kurz M. and Staudigel H. (2004) Recycled metasomatized lithosphere as the origin of the Enriched Mantle II (EM2) end-member: Evidence from the Samoan Volcanic Chain. *Geochemistry, Geophys. Geosystems* **5**, 1–44.

Yang A. Y., Zhao T. P., Zhou M. F., Deng X. G., Wang G. Q. and Li J. (2013) Os isotopic compositions of MORBs from the ultra-slow spreading Southwest Indian Ridge: Constraints on the assimilation and fractional crystallization (AFC) processes. *Lithos* **179**, 28–35. Available at: http://dx.doi.org/10.1016/j.lithos.2013.07.020.

Yao Z., Mungall J. and Jenkins M. (2020) Formation of the Rustenburg Layered Suite by assimilation - batch crystallization (ABC) and - fractional crystallization (AFC). *Res. Sq.* **Preprint**, 1–25.

Zeh A., Ovtcharova M., Wilson A. H. and Schaltegger U. (2015) The Bushveld Complex was emplaced and cooled in less than one million years - results of zirconology, and geotectonic implications. *Earth Planet. Sci. Lett.* **418**, 103–114. Available at: http://dx.doi.org/10.1016/j.epsl.2015.02.035.

Zeh A., Wilson A. H., Gudelius D. and Gerdes A. (2019) Hafnium Isotopic Composition of the Bushveld Complex Requires Mantle Melt–Upper Crust Mixing: New Evidence from Zirconology of Mafic, Felsic and Metasedimentary Rocks. *J. Petrol.* **60**, 2169–2200.

Zheng Y. F. (1993) Calculation of oxygen isotope fractionation in anhydrous silicate minerals. *Geochim. Cosmochim. Acta* **57**, 1079–1091.

Zindler A. and Hart S. (1986) Chemical Geodynamics. *Annu. Rev. Earth Planet. Sci.* **14**, 493–571.

Zirakparvar N. A., Mathez E. A., Rajesh H. M. and Choe S. (2019) Lu-Hf isotopic evidence of a deep mantle plume source for the ~2.06 Ga Bushveld Large Igneous Province. *Lithos* **348**–**349**, 105168.

Zirakparvar N. A., Mathez E. A., Scoates J. S. and Wall C. J. (2014) Zircon Hf isotope evidence for an enriched mantle source for the Bushveld Igneous Complex. *Contrib. to Mineral. Petrol.* **168**, 1–18.